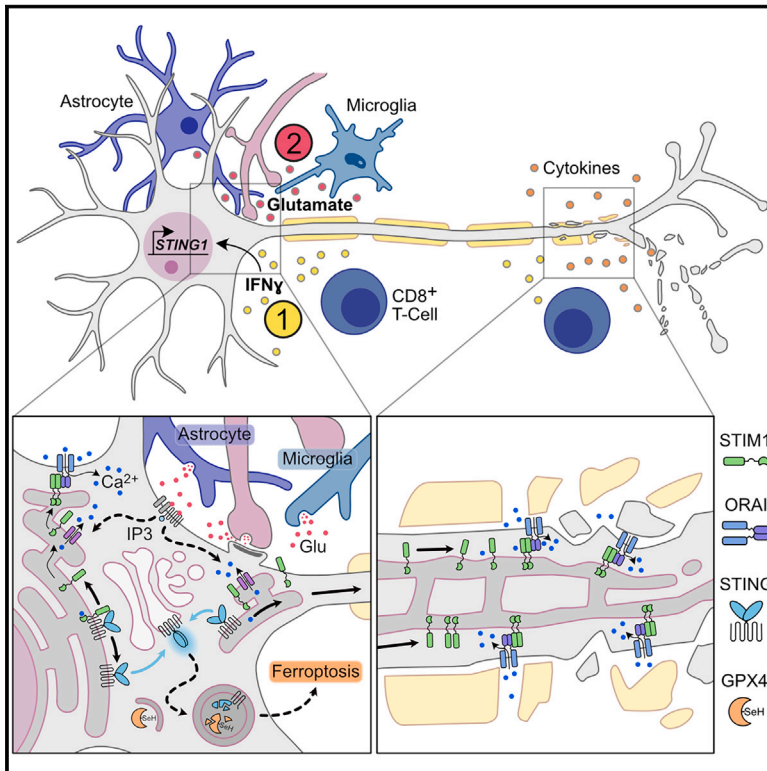


STING orchestrates the neuronal inflammatory stress response in multiple sclerosis

Graphical abstract



Authors

Marcel S. Woo, Christina Mayer, Lars Binkle-Ladisch, ..., Doron Merkler, Marc Freichel, Manuel A. Friese

Correspondence

manuel.friese@zmnh.uni-hamburg.de

In brief

Inflammation and glutamate excitotoxicity are the major drivers of neuronal cell death in multiple sclerosis (MS). This study identifies neuronal STING as a central regulator of inflammation-induced neurodegeneration by integrating (1) interferon and (2) glutamate-evoked intracellular calcium signaling to induce ferroptotic cell death, offering a target for treating MS-related neurodegeneration.

Highlights

- STING is expressed in human and mouse neurons solely under inflammatory conditions
- Excitotoxicity activates a non-canonical STIM1-STING signaling pathway in neurons
- Neuronal STING activation leads to autophagic GPX4 degradation and ferroptosis
- Targeting neuronal STING protects from inflammation-induced neurodegeneration

Article

STING orchestrates the neuronal inflammatory stress response in multiple sclerosis

Marcel S. Woo,^{1,7} Christina Mayer,^{1,7} Lars Binkle-Ladisch,^{1,8} Jana K. Sonner,^{1,8} Sina C. Rosenkranz,¹ Artem Shaposhnykov,¹ Nicola Rothhammer,¹ Volodymyr Tsvilovsky,^{2,3} Svenja M. Lorenz,⁴ Lukas Raich,¹ Lukas C. Bal,¹ Vanessa Vieira,¹ Ingrid Wagner,⁵ Simone Bauer,¹ Markus Glatzel,⁶ Marcus Conrad,⁴ Doron Merkler,⁵ Marc Freichel,^{2,3} and Manuel A. Friese^{1,9,*}

¹Institute of Neuroimmunology and Multiple Sclerosis, University Medical Center Hamburg-Eppendorf, Hamburg, Germany

²Institute of Pharmacology, Heidelberg University, Heidelberg, Germany

³DZHK (German Centre for Cardiovascular Research), partner site Heidelberg/Mannheim, Heidelberg, Germany

⁴Institute of Metabolism and Cell Death, Helmholtz Zentrum München, Neuherberg, Germany

⁵Department of Pathology and Immunology, Division of Clinical Pathology, Faculty of Medicine, University and University Hospital of Geneva, Geneva, Switzerland

⁶Institute of Neuropathology, University Medical Center Hamburg-Eppendorf, Hamburg, Germany

⁷These authors contributed equally

⁸These authors contributed equally

⁹Lead contact

*Correspondence: manuel.friese@zmnh.uni-hamburg.de

<https://doi.org/10.1016/j.cell.2024.05.031>

SUMMARY

Inflammation-induced neurodegeneration is a defining feature of multiple sclerosis (MS), yet the underlying mechanisms remain unclear. By dissecting the neuronal inflammatory stress response, we discovered that neurons in MS and its mouse model induce the stimulator of interferon genes (STING). However, activation of neuronal STING requires its detachment from the stromal interaction molecule 1 (STIM1), a process triggered by glutamate excitotoxicity. This detachment initiates non-canonical STING signaling, which leads to autophagic degradation of glutathione peroxidase 4 (GPX4), essential for neuronal redox homeostasis and thereby inducing ferroptosis. Both genetic and pharmacological interventions that target STING in neurons protect against inflammation-induced neurodegeneration. Our findings position STING as a central regulator of the detrimental neuronal inflammatory stress response, integrating inflammation with glutamate signaling to cause neuronal cell death, and present it as a tractable target for treating neurodegeneration in MS.

INTRODUCTION

The intricate interplay between inflammation and neurodegeneration is exemplified in multiple sclerosis (MS), the most common autoimmune disease of the central nervous system (CNS).¹ Over the course of MS, persistent inflammation continuously challenges neurons, leading to neurodegeneration and worsening of neurological disability. While immunosuppressive drugs are effective in modulating CNS-infiltrating immune cells in MS, they cannot intervene in progressive neurodegeneration.^{2,3} Therefore, there is an unmet clinical need to halt inflammation-induced neurodegeneration in MS and other neurodegenerative diseases by neuroprotective therapeutics with direct action on neurons.⁴

Extensive research in MS has elucidated the important role of infiltrating immune cells⁵ and CNS-resident glial cells,⁶ particularly microglia and astrocytes, in eliciting chronic neuroinflammation. By contrast, neurons are often regarded as passive targets of these neuroinflammatory challenges, primarily due to their low expression of immune-related genes and limited ability

for morphological changes and proliferation in response to inflammatory stimuli. However, the concept of active neuronal involvement by launching a neuronal inflammatory stress response (NISR) after sensing a diverse array of cytokines or stressors during neuroinflammation is increasingly being acknowledged.^{7–9} While the composition of the NISR during CNS inflammation is not well defined, it likely determines the fate of neurons.^{10–12}

Indeed, neurons do not only passively react to cytokines to maintain homeostasis and guide development,^{13,14} but they also possess the capability to actively modulate immune responses in inflammatory environments.^{7,8} The active participation of neurons in CNS inflammation is illustrated by the neuronal response to interferon- γ (IFN γ), a highly abundant cytokine in the CNS during MS and other neurodegenerative diseases.^{15–17} IFN γ binds to the type II IFN receptor on neurons and induces the expression and phosphorylation of signal transducer and activator of transcription 1 (STAT1), followed by the induction of interferon response genes (IRGs).¹⁸ In a mouse model of neurotropic virus infection, the neuronal type II IFN response

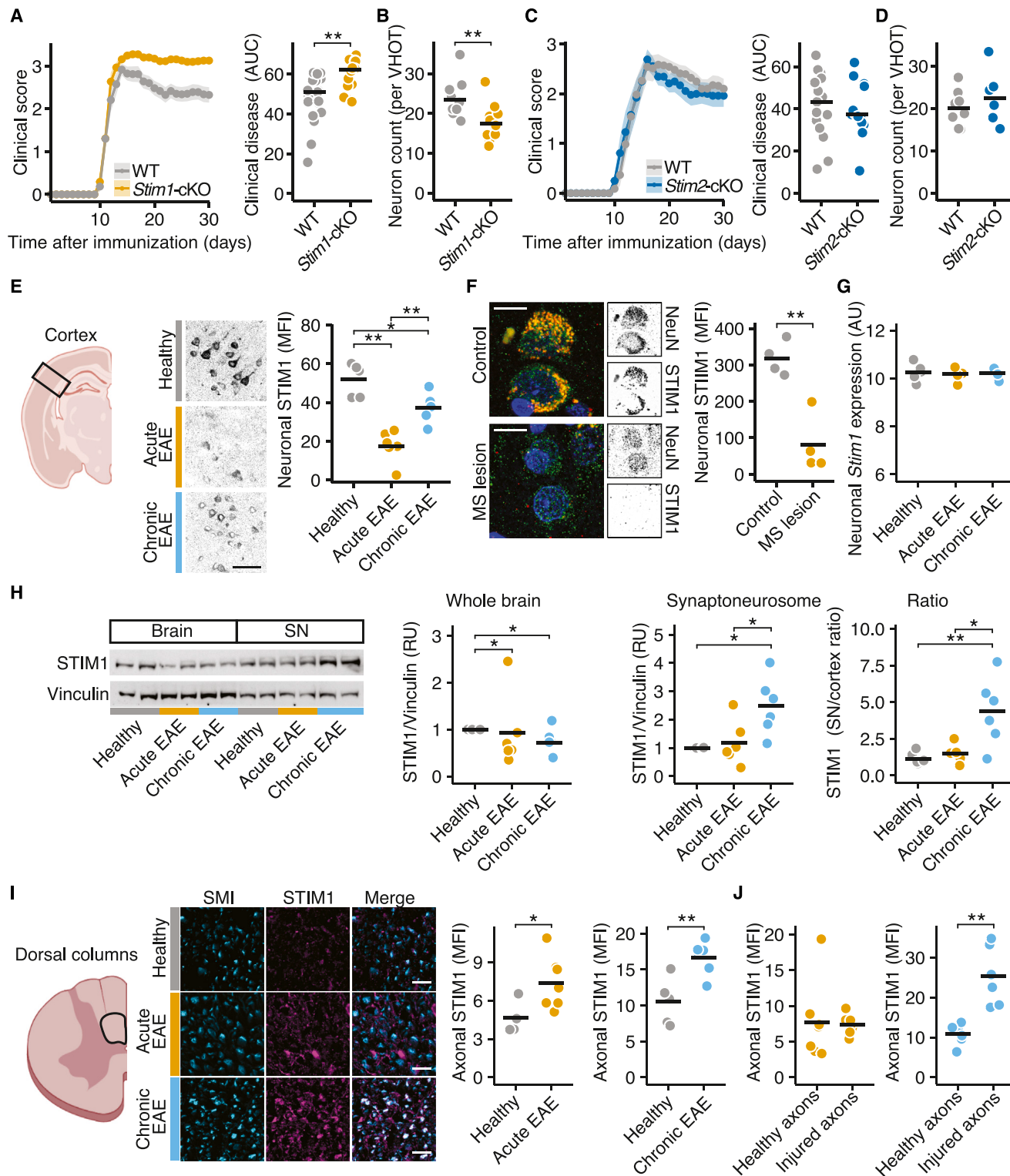


Figure 1. STIM1 deficiency increases neuronal vulnerability in CNS inflammation

(A) Clinical disease course and cumulative disease score (area under the curve [AUC]) of WT ($n = 20$) and *Stim1*-cKO ($n = 18$) mice that were subjected to EAE. EAE disease curves show the mean and standard error mean.

(B) Number of motor neurons in the spinal cord ventral horn outflow tract (VHOT) of WT ($n = 10$) and *Stim1*-cKO ($n = 10$) mice 30 days after EAE immunization.

(C) Clinical disease course and cumulative disease score (area under the curve [AUC]) of WT ($n = 18$) and *Stim2*-cKO ($n = 13$) mice that were subjected to EAE. EAE disease curves show the mean and standard error mean.

(legend continued on next page)

decisively modulates synaptic cleavage by CC-chemokine ligand 2 secretion and subsequent phagocyte recruitment.⁷ Additionally, IFN γ modulates glutamate-dependent calcium currents in the peripheral nervous system (PNS), showing that cytokine signaling alters neuronal ion homeostasis.¹⁹ Although it is likely that IFN γ is key in setting up the NISR, it is unclear how IFN γ signaling integrates with other stressors. Furthermore, non-canonical IFN γ signaling pathways are activated with varying exposure time.²⁰ However, their contribution to the NISR and their potential role in inflammation-induced neurodegeneration remain unexplored.

Besides cytokines, neuronal homeostasis during neuroinflammation is challenged by neuronal ion imbalance.^{12,21} Its main contributor, excessive levels of extracellular glutamate, stems from various sources, including glutamate release from dying cells, active glutamate secretion by immune cells, and impaired glutamate metabolism by glial cells, especially astrocytes.^{12,21–23} The excessive extracellular glutamate leads to excitotoxicity that is mediated by intracellular calcium accumulation following activation of ionotropic glutamate receptors, but also calcium release from internal stores. This disturbs the neuronal calcium equilibrium, a critical determinant of neuronal integrity, synaptic function, and survival.²⁴

In contrast to neurons, non-excitable cells like immune cells primarily rely on store-operated calcium entry (SOCE).^{25,26} This process is initiated through calcium release from the endoplasmic reticulum (ER), prompting the ER transmembrane calcium sensor proteins, stromal interaction molecule 1 and 2 (STIM1, STIM2), to translocate to contact sites between the ER and the plasma membrane. There, they cluster with calcium release-activated calcium (CRAC) channels, such as ORAI calcium release-activated calcium modulator 1 (ORAI1). This allows calcium influx from the extracellular space and subsequent replenishment of ER stores.^{25,26} Intriguingly, recent findings have identified that calcium release from the ER is also a pivotal contributor to glutamate excitotoxic cell death during neuroinflammation.^{10,27} However, although ER calcium depletion (ERCa²⁺D) exacerbates glutamate-induced calcium accumulation in neurons,²⁵ the interplay with inflammatory signaling cascades and the impact of STIM translocation on neuronal fate during CNS inflammation remain unclear.

Given the unknown composition of the NISR, which is elicited by exposure to various inflammatory cues like cytokines and glutamate, we set out to define its functional switches that integrate these cues and dictate neuronal fate. We discovered the stimulator of interferon genes (STING) as a targetable master regulator in neurons that operates at the intersection of inflam-

mation and ion imbalance and is key in driving inflammation-induced neurodegeneration.

RESULTS

STIM1 mitigates inflammation-induced neurodegeneration

To investigate whether the neuronal STIM proteins are involved in neurodegeneration during CNS inflammation, we established mice with neuron-specific deletion of *Stim1* or *Stim2*. To this end, we bred *Snap25-Cre* mice that express the Cre recombinase under the control of the neuron-specific *Snap25* promoter with *Stim1*^{flox/flox},²⁵ (*Stim1*-conditional knockout [cKO]) or *Stim2*^{flox/flox},²⁵ mice (*Stim2*-cKO). These mice were then subjected to experimental autoimmune encephalomyelitis (EAE) by active immunization with the MOG_{35–55} peptide. *Stim1*-cKO (Figures 1A, 1B, S1A, and S1B) but not *Stim2*-cKO (Figures 1C, 1D, S1C, and S1D) showed an exacerbated disease course with increased neuronal loss, highlighting that STIM1 is required for neuronal resilience against neuroinflammation. To understand the specific contribution of STIM1 during neuroinflammation, we first characterized STIM1 expression and subcellular localization in EAE. A strong reduction of the STIM1 protein was detected in neuronal somata in the cortex of EAE mice (Figure 1E) and in neuronal somata of people with MS (pwMS) who underwent brain biopsies (Figure 1F). This reduction was not due to a transcriptional regulation, as neuronal *Stim1* mRNA was not differentially expressed in EAE (Figure 1G). Since neuronal ERCa²⁺D is evident in EAE animals²⁷ and in excitotoxic cell death,¹⁰ we postulated that neuronal SOCE might be activated in EAE through a mechanism involving compensatory increase of STIM1 levels in the synaptic and axonal compartments. To probe that, we first compared STIM1 protein levels in synaptoneurosome fractions (Figure S1E) of cortices of acute and chronic EAE mice. Intriguingly, STIM1 protein levels were increased in the synaptoneurosome fraction in chronic EAE animals, whereas STIM1 levels in the entire cortex were reduced (Figure 1H). Next, we analyzed the axonal projections of these cortical motor neurons in the dorsal column of the spinal cord.²⁸ Axonal STIM1 staining was elevated during acute and chronic disease stages (Figures 1I and S1F), supporting our hypothesis that STIM1 increases in synapses and axons upon SOCE activation. Given that the increase of STIM1 in axons may reflect excitotoxic damage, we next tested whether STIM1 is preferentially located at injured axonal sites. To this end, we compared STIM1 levels in healthy axons with phosphorylated (SMI31⁺) and injured axons with non-phosphorylated (SMI32⁺) neurofilament H. Indeed, STIM1

- (D) Number of motor neurons in the spinal cord ventral horn out flow tract (VHOT) of WT ($n = 8$) and *Stim2*-cKO ($n = 6$) mice 30 days after EAE immunization.
(E) STIM1 mean fluorescence intensity (MFI) in cortical neurons of healthy and acute and chronic EAE mice ($n = 5$ per group).
(F) Neuronal STIM1 MFI in brain biopsies of MS lesions and non-inflammatory controls ($n = 4$ per group). Scale bar shows 5 μm .
(G) Neuronal *Stim1* mRNA expression (arbitrary units [a.u.]) in cortical neurons of healthy ($n = 5$) and EAE mice (acute, $n = 5$; chronic, $n = 4$).
(H) STIM1 and vinculin protein levels in whole brain lysates (brain) and synaptoneurosome (SNs) of healthy mice and acute and chronic EAE mice ($n = 6$ per group) assessed by immunoblot. Ratio to vinculin as normalization control is shown as relative units (RU).
(I) Axonal STIM1 immunohistochemistry (MFI) in spinal cord dorsal columns of healthy and EAE mice ($n = 6$ per group).
(J) STIM1 MFI in spinal cord dorsal columns in SMI31⁺ (healthy) and SMI32⁺ (injured) axons in acute and chronic EAE ($n = 6$). Scale bar shows 20 μm . For comparing EAE phenotypes non-parametric Mann-Whitney U test was used. If not stated otherwise, unpaired t test with false discovery rate (FDR) correction for multiple comparisons was used, and individual mice or independent experiments and the median are shown. * $p < 0.05$, ** $p < 0.01$. See also Figure S1 and Table S2.

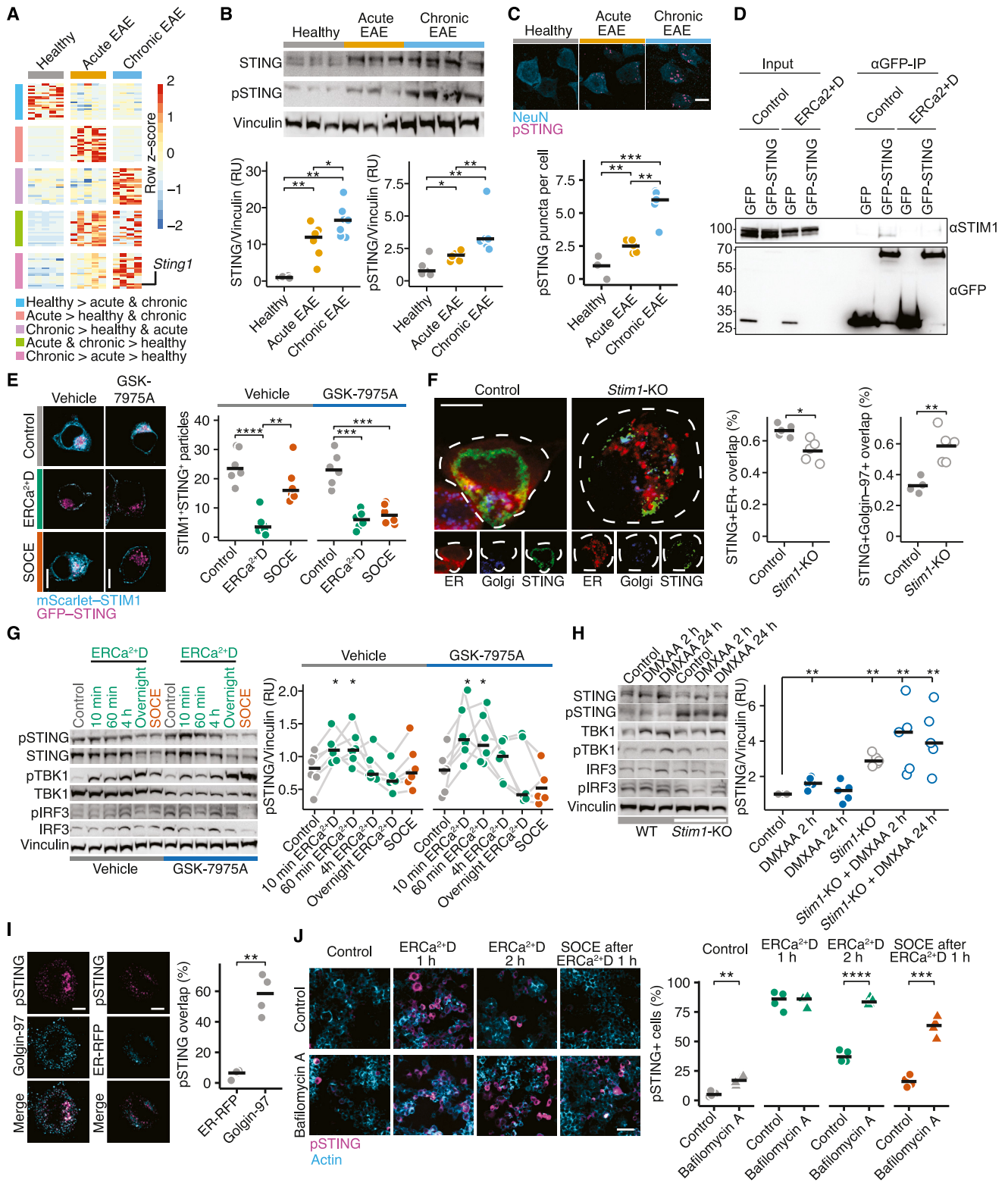


Figure 2. ER calcium depletion induces STING trafficking to the Golgi apparatus and its activation

(A) Gene expression heatmap of the top 10 differentially expressed genes in cortical motor neurons of healthy ($n = 5$), acute EAE ($n = 5$), and chronic EAE ($n = 4$) after translating ribosome affinity purification and sequencing of Glt25d2-BacTRAP mice. Genes are grouped by the depicted modules that reflect different patterns of neuronal transcription during the disease course.

(legend continued on next page)

levels were found to be substantially higher in injured SMI32⁺ axons in comparison with uninjured or recovered SMI31⁺ axons during chronic EAE (Figures 1J and S1G). Of note, no differences in *Stim1* mRNA and STIM1 protein levels were observed in motor neurons of the ventral horn of the spinal cord (Figures S1H and S1I). Together, *Stim1* deficiency increases neuronal vulnerability to inflammation-induced neurodegeneration. Furthermore, CNS inflammation is associated with a significant reduction of STIM1 in neuronal somata, likely attributable to the translocation of STIM1 to injured axons or compensatory increase of STIM1 in those axons.

Glutamate-induced excitotoxicity activates SOCE

After having shown that somatic STIM1 reduction or deficiency contributes to inflammation-induced cell death in EAE, we assessed the role of ERCa²⁺D in excitotoxic neuronal cell death *in vitro*. We used different genetically encoded calcium sensors to monitor glutamate-induced calcium changes in different neuronal compartments. Glutamate excitotoxicity simultaneously increased cytosolic calcium levels and calcium influx through ORAI while depleting ER calcium levels (Figures S2A and S2B). At the same time, the number of STIM1⁺ and ER⁺ dendritic spines, as well as STIM1⁺ membrane-associated clusters increased when neurons were exposed to glutamate excitotoxicity, which could be recapitulated by directly inducing ERCa²⁺D (Figures S2C–S2F). Notably, comparable to ERCa²⁺D, glutamate excitotoxicity led to a strong increase in co-localization of the membrane-associated STIM1⁺ clusters with ORAI1. The STIM1⁺ORAI1⁺ clusters were reversed by inducing SOCE through replenishing calcium, which could be blocked by using the CRAC channel inhibitor GSK-7975A (Figures S2G–S2I). Thus, ERCa²⁺D is part of the neuronal stress response to glutamate excitotoxicity and leads to relocation of STIM1 to the cell membrane, where it interacts with ORAI1.

Neuronal STING is activated by SOCE

To mechanistically decipher how *Stim1* deficiency increases neuronal susceptibility during CNS inflammation, we challenged *Stim1*-deficient cortical neurons with glutamate and measured

cell viability and cytosolic calcium accumulation. Unexpectedly, we did not detect any differences in neuronal susceptibility between neurons lacking *Stim1* and wild-type (WT) neurons, letting us conclude that an inflammatory milieu might be required (Figure S3A). To test this hypothesis, we chronically exposed neurons to IFN γ . Indeed, this inflammatory exposure rendered *Stim1*-deficient neurons more susceptible to excitotoxic cell death in comparison with WT neurons (Figure S3A). The differential susceptibility was not explained by differences in glutamate-induced cytosolic calcium rise (Figure S3B) and suggested the necessity of an inflammation-induced factor for the increased vulnerability observed in *Stim1*-cKO EAE mice.

To explore the neuronal response to inflammation that contributes to the STIM1-dependent neuronal vulnerability, we sequenced translating ribosome affinity purification (TRAP) profiles of cortical motor neurons from Glt25d2-EGFP/L10a mice²⁹ during acute and chronic EAE (Figure 2A; Table S1). Notably, one of the neuronal genes that was most strongly induced in both acute and chronic EAE was *Sting1* (Figure S3C), which caught our attention as it has been described as a direct interactor of STIM1 in T cells³⁰ and fibroblasts.³¹ STING is an ER transmembrane protein that has first been reported as an essential mediator of type I IFN response against microbial infections that is activated by the cyclic guanosine monophosphate (GMP)-AMP synthase (cGAS)³² after recognition of foreign double-strand DNA (dsDNA).^{33–39} In addition, its activation by mitochondrial dsDNA has recently been recognized as an important driver of inflammatory microglia activation in aging⁴⁰ and amyotrophic lateral sclerosis.⁴¹ However, its expression and function in neurons are unknown. Furthermore, it is unclear whether there are alternative routes of STING activation in neurons.

Intriguingly, we could not detect STING expression in primary neurons under normal cell culture conditions. By contrast, its expression was strongly induced upon prolonged exposure to IFN γ (Figure S3D), emphasizing that STING is selectively expressed in inflamed neurons. We confirmed its induction *in vivo* by immunoblotting of whole cortex lysates. Similar to the transcriptional changes, STING and its activated phosphorylated form (pSTING) increased continuously in acute and chronic

(B) STING, pSTING, and vinculin protein levels in whole brain lysates of healthy ($n = 6$), acute EAE ($n = 6$), and chronic EAE mice ($n = 7$). Ratio to vinculin as normalization control is shown as relative units (RUs).

(C) Neuronal pSTING puncta per cell in immunohistochemistry of cortical neurons in healthy, acute, and chronic EAE mice ($n = 5$ per group).

(D) Immunoprecipitation of GFP or GFP-STING in N2a cells that were unstimulated (control) or were exposed to targeted ER calcium depletion (ERCa²⁺D) for 24 h. Immunoblotting against STIM1 or GFP. A representative immunoblot is shown.

(E) mScarlet-STIM1 and GFP-STING transfected N2a cells that were exposed to ERCa²⁺D and subsequent store-operated calcium entry (SOCE) by replenishing of calcium with or without 20 μ M of the CRAC-inhibitor GSK-7975A ($n = 6$ per group). The number of STIM1+STING+ puncta was quantified. Scale bar shows 20 μ m.

(F) Quantification of percentage of STING⁺ER⁺ and STING⁺Golgin-97⁺ overlapping areas in WT control and *Stim1*-KO N2a cells. Scale bar shows 20 μ m.

(G) Immunoblot quantification of pSTING, STING, pTBK1, TBK1, pIRF3, IRF3, and vinculin in N2a cells that were exposed to targeted ERCa²⁺D for indicated times and subsequent SOCE after 1-h ERCa²⁺D by calcium replenishing with or without 20 μ M GSK-7975A ($n = 6$ per group). Paired t test against the controls was performed. Ratio to vinculin as normalization control is shown as relative units (RUs).

(H) Immunoblot quantification of STING, pSTING, TBK1, pTBK1, IRF3, pIRF3, and vinculin in WT and *Stim1*-KO N2a cells that were additionally exposed to 50 μ g mL⁻¹ of the STING agonist DMXAA for 2 or 24 h ($n = 5$ per group). Ratio to vinculin as normalization control is shown as relative units (RUs).

(I) Quantification of percentage of pSTING⁺Golgin-97⁺ and pSTING⁺ER⁺ overlapping area in N2a cells that were exposed to ERCa²⁺D for 1 h ($n = 4$). Scale bar shows 10 μ m.

(J) Quantification of pSTING⁺ N2a cells after exposure to ERCa²⁺D for 1 or 2 h, or SOCE activation after 1-h ERCa²⁺D. If indicated 50 nM bafilomycin A1 was applied 1 h before the different stimulations ($n = 4$). Scale bar shows 50 μ m. If not stated otherwise, unpaired t test with FDR correction for multiple comparisons was used, and individual mice or independent experiments and the median are shown. * $p < 0.05$, ** $p < 0.01$, *** $p < 0.001$, **** $p < 0.0001$.

See also Figure S2 and Table S1.

EAE (Figure 2B). This was primarily driven by an increase in neuronal STING and pSTING levels, which peaked during the chronic disease stage (Figures 2C and S3E). On the contrary, the highest STING and pSTING levels in non-neuronal cells and specifically in microglia were observed during acute EAE (Figures S3F and S3G).

Next, we probed the expression of the downstream effectors of canonical STING signaling in EAE. Of those, only the interferon regulatory factor 3 (IRF3) was upregulated in the cortex of EAE mice, which was explained by IRF3 expression in microglia. Even though we detected neuronal baseline expression of IRF3, phosphorylated IRF3 (pIRF3),⁴² phosphorylated tank-binding kinase 1 (pTBK1),⁴³ and phosphorylated nuclear factor kappa-light-chain enhancer of activated B cells (pNF- κ B)⁴⁴ as assessed by immunoblotting (Figure S3H) and immunohistochemistry (Figure S3I), we observed no increase during chronic EAE.³⁹ Furthermore, pIRF3, pNF- κ B, or pTBK were not expressed in non-neuronal cells at baseline or during EAE. Of note, bone marrow-derived dendritic cells (BMDCs) served as a positive control for our assays, and as expected, treatment with the STING ligand 5,6-dimethylxanthenone-4-acetic acid (DMXAA) strongly induced the canonical STING signaling pathway (Figure S3J). Thus, the canonical STING pathway is not induced in cortical neurons during CNS inflammation.

Therefore, we hypothesized that STIM1 depletion from neuronal cell bodies, possibly by translocation to damaged axons, during CNS inflammation might lead to STING activation in neurons. To interrogate whether STING and STIM1 physically interact, we performed an immunoprecipitation of STING-overexpressing Neuro-2a (N2a) cells. Indeed, endogenous STIM1 was co-immunoprecipitated with EGFP-tagged STING, showing the direct interaction between STING and STIM1, which was markedly decreased after ERCa²⁺D (Figure 2D). Consistently, in steady state, EGFP-STING co-localized with mScarlet-STIM1 at the ER (Figure 2E) and translocated to the Golgi apparatus after chemical activation of STING by DMXAA (Figure S3K), trafficking of STIM1 to the cell membrane through ERCa²⁺D (Figure 2E) or by genetic deletion of *Stim1* (Figure 2F). The STIM-STING co-localization was regulated by SOCE since calcium replenishing restored their co-localization, which could be inhibited by applying the CRAC-inhibitor GSK-7975A (Figure 2E). The dissociation of STING from STIM1 led to the phosphorylation of STING (Figure 2G). Additionally, ERCa²⁺D and treatment with the STING ligand DMXAA in WT N2a cells as well as genetic *Stim1* deletion increased pSTING levels in N2a cells. Notably, DMXAA did not further enhanced pSTING in *Stim1*-deficient N2a cells (Figures 2H, S3L, and S3M), and pSTING was mainly localized at the Golgi apparatus (Figure 2I). Furthermore, ERCa²⁺D-induced STING phosphorylation was only partially dependent on TBK1 signaling, as the TBK1 inhibitor GSK-8612⁴⁵ did not completely block the induction of pSTING (Figures S3N and S3O). Therefore, neuronal ERCa²⁺D results in STING trafficking to the Golgi apparatus that leads to its phosphorylation.

Since we observed that ERCa²⁺D leads only to a transient increase of pSTING, and its subsequent degradation was neither further enhanced by SOCE activation nor blocked by the CRAC-inhibitor GSK-7975A (Figure 2G), we hypothesized that

ERCa²⁺D specifically increases the initiation of STING signaling without affecting its degradation. Due to recent evidence that STING is continuously degraded in lysosomes,^{46,47} we treated N2a cells with the inhibitor of lysosomal function bafilomycin A and measured pSTING levels after ERCa²⁺D and subsequent SOCE activation. Lysosomal inhibition did not increase the level of phosphorylation of STING that is induced by ERCa²⁺D, but it prevented the decline of pSTING levels, both in the absence and presence of SOCE (Figure 2J). Thus, ERCa²⁺D enhances STING activation in neurons, which is then terminated by lysosomal degradation, independent of calcium replenishment.

STING does not induce the canonical pathway in neurons

Next, we explored how STING influences the viability of neurons *in vitro*. Since STING is not expressed at steady state, we either used lentiviral expression of STING with 80%–90% transduction efficacy, or induced it by prolonged IFN γ exposure, or by lentiviral *Irfng* expression (Figure S3D). Neurons that were transduced with an mScarlet-carrying lentivirus served as a control ruling out that transduction alone caused the observed effects. STING co-localized with STIM1 at the ER and detached after targeted ERCa²⁺D, glutamate excitotoxicity, or chemical STING activation with DMXAA (Figures 3A, S4A, and S4B). Neurons expressing STING and those subjected to prolonged IFN γ exposure were more vulnerable to glutamate excitotoxicity (Figures 3B and S4D), which could be rescued by treating them with the STING inhibitors C176 or H151⁴⁸ (Figures 3C, 3D, and S4D) or by using *Sting1*-deficient neurons (Figure 3E), and was not further enhanced by treating neurons with the STING agonist 10-carboxymethyl-9-acridanone (CMA; Figure 3C). To confirm that the translocation of STING to the Golgi apparatus is required for STING-mediated vulnerability, the same assays were performed with neurons expressing an ER-retained STING variant (STING^{ER}; Figure S3K). Notably, this prevented the increase in neuronal vulnerability (Figure 3F), and we did not observe protection by C176 or any impact of CMA, underscoring that STING trafficking to the Golgi apparatus is required for increasing neuronal vulnerability. On the same note, neither H151 nor C176 protected from excitotoxicity in neurons without STING expression, highlighting their specificity (Figures S4D and S4E). Again, *Stim1*-deficient neurons demonstrated greater susceptibility to STING-induced cell death than WT neurons, corroborating the important role of STIM1 in retaining STING at the ER in inflamed neurons (Figure 3G).

To understand the molecular mechanism of STING-mediated neuronal vulnerability, we first analyzed the canonical STING signaling pathway. Although ERCa²⁺D robustly induced phosphorylation of both STING and TBK1, the levels of pTBK1 were comparable between WT and *Sting1*-deficient N2a cells (Figure S4F). Furthermore, *Stim1*-deficient N2a cells displayed higher levels of pSTING compared with DMXAA-treated WT N2a cells but did not activate the canonical downstream effectors of STING (Figures 2H and S3L). Notably, in contrast to immune cells like BMDCs (Figure S3J), neuronal cultures showed already at steady state a detectable expression of pTBK1, pIRF3, and pNF- κ B. This expression was not further increased by STING expression and subsequent exposure to DMXAA,

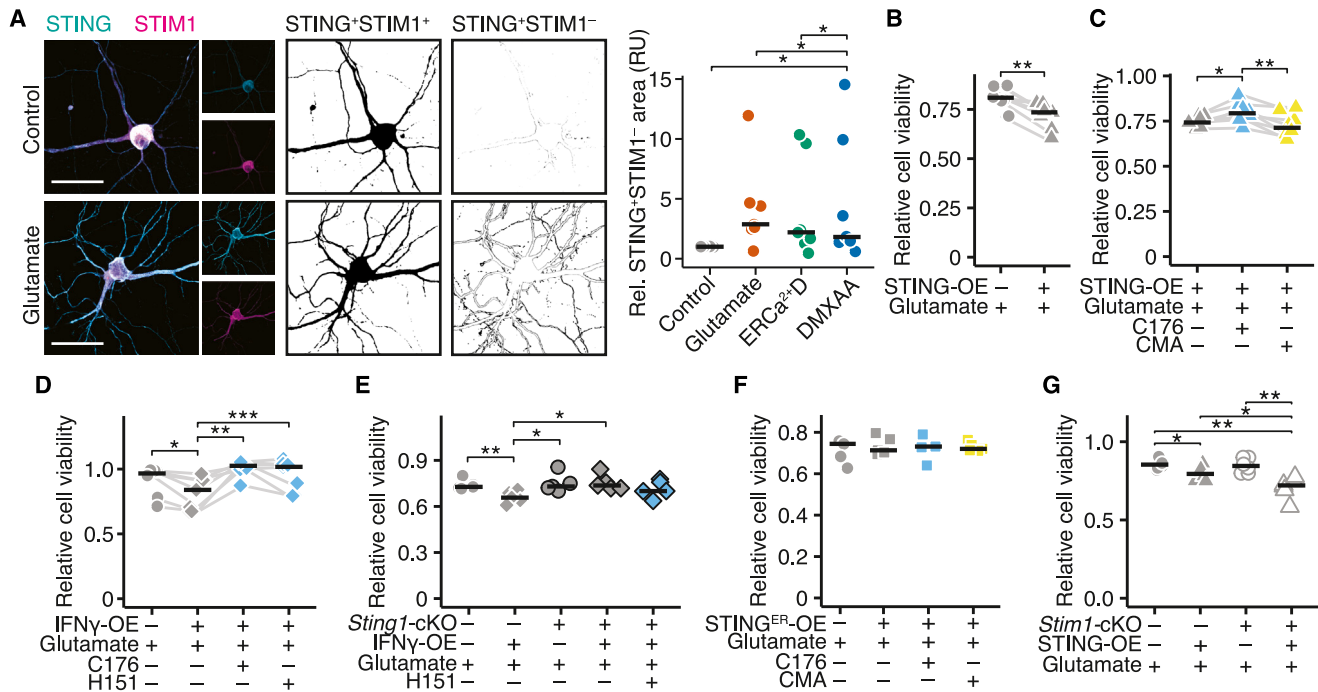


Figure 3. STING increases neuronal vulnerability to excitotoxicity

(A) EGFP-STING and mScarlet-STIM1 transfected neurons that were exposed for 6 h to 50 μ M glutamate, 50 μ g mL⁻¹ DMXAA, and targeted ER calcium depletion (ERCa²⁺D). The increase in relative units (RUs) of STING⁺STIM1⁺ area in comparison with controls was quantified ($n = 7$ per group). Scale bar shows 30 μ m. (B) Relative cell viability after 50 μ M glutamate challenge of STING-overexpressing (STING-OE) neurons and controls ($n = 7$ per group). Paired t test was used. (C) STING-OE neurons that were exposed to 50 μ M glutamate and were pre-treated with 1 μ M of the STING antagonist C176 or 20 μ M of the STING agonist CMA ($n = 7$ per group). Paired t test was used. (D) Relative cell viability of IFN γ -overexpressing (IFN γ -OE) neuronal cultures that were exposed to 50 μ M glutamate and were pre-treated with 1 μ M C176 or 1 μ M H151 ($n = 5$ per group). Paired t test was used. (E) Relative cell viability of WT and *Sting1*-cKO neurons that overexpress IFN γ and were exposed to 50 μ M glutamate with or without pre-treatment with 1 μ M H151 ($n = 5$ per group). (F) Relative cell viability of STING^{ER}-overexpressing (STING^{ER}-OE) neurons that were exposed to 50 μ M glutamate and were pre-treated with 1 μ M H151 or 20 μ M CMA ($n = 4$ per group). (G) Relative cell viability of WT and *Stim1*-cKO neurons that overexpress STING and were exposed to 50 μ M glutamate ($n = 6$ per group). If not stated otherwise, unpaired t test with FDR correction for multiple comparisons was used, and independent experiments and the median are shown. * $p < 0.05$, ** $p < 0.01$, *** $p < 0.001$.

See also [Figures S3](#) and [S4](#).

poly(I:C), glutamate excitotoxicity, or ERCa²⁺D, as measured by immunoblot ([Figures S4G](#) and [S4H](#)). Similarly, exposure to the RNA mimic poly(I:C) induced *Cxcl10* and *Irf44* expression in neuronal cultures regardless of STING expression ([Figure S4I](#)), underscoring that neurons are capable to induce an IFN response independent of STING. To test whether STING might activate its canonical signaling pathway *in vivo*, we first analyzed protein expression of the downstream targets of canonical STING signaling in the cortex of WT and *Sting1*-cKO mice that do not express *Sting1* specifically in neurons. These were generated by breeding *Snap25-Cre* mice with *Sting1*^{flox/flox},⁴⁹ mice. Again, we observed a high baseline expression of pTBK1 and pIRF3, which were independent of STING ([Figure S4J](#)). This pattern was also observed when analyzing neurons of WT and *Sting1*-cKO mice during EAE by using immunohistochemistry ([Figure S4K](#)). Furthermore, we isolated neuronal nuclei from healthy or EAE mice from a WT or *Sting1*-cKO background and compared the expression of *Cxcl10*, *Irf44*, and *Irfn*. Similar to

our findings in neuronal cultures, these transcripts were upregulated in neurons during EAE, independently of genetic *Sting1* deletion ([Figure S4L](#)). Thus, we demonstrate that, both *in vitro* and in adult mice, the canonical type I IFN-stimulating pathway is expressed at steady state and is further upregulated in neurons during CNS inflammation, independent of STING.

STING induces autophagy-dependent cell death in neurons

Since the canonical STING signaling pathway is not operational in inflamed neurons, we hypothesized a role for non-canonical STING signaling^{50,51} pathways, such as the induction of autophagy. Autophagy is a cellular process necessary for degradation of unfolded proteins, damaged organelles, and pathogens.⁵² It leads to the formation of double-membraned vesicles, the autophagosomes, that guide its content to the lysosome for degradation.⁵¹ Although autophagy is necessary for homeostasis and health, altered autophagy is increasingly

recognized as contributor to aging and diverse diseases.⁵² STING-mediated autophagy serves to limit pathogen infection by facilitating the removal of viruses and bacteria. This process can occur independently of TBK1 activation and IFN induction.⁵¹ We stained for autophagic vacuoles after inhibiting their lysosomal degradation by using bafilomycin A1 to assess the autophagic flux in STING-expressing (Figure 4A) or IFN γ -exposed neurons (Figures 4B and S5A). This was done in combination with STING activation by glutamate excitotoxicity, ERCa²⁺D induction, or DMXAA. Indeed, each stimulus that led to STING activation in neurons induced autophagy, which could be suppressed by the application of H151 or genetic deletion of *Sting1* (Figures 4C and S5B). Increased autophagy in neurons expressing STING or exposed to IFN γ that were treated with glutamate was further confirmed by measuring LC3 degradation with the GFP-LC3-RFP-LC3 Δ G reporter⁵³ (Figure S5C), endogenous LC3 puncta (Figure S5D), or accumulation of transfected GFP-LC3 (Figure S5E) after bafilomycin A1 treatment. Additionally, an increased LC3-II/LC3-I ratio was observed in STING-expressing neurons (Figure S5F). Importantly, this was independent of the canonical STING signaling pathway, as treating neurons with a TBK1 inhibitor (Figure S5G) or expression of the C-terminal truncated STING Δ CT variant, which cannot interact with TBK1 and IRF3,⁵⁴ increased glutamate-induced autophagy flux to a similar extent as the STING WT variant (Figure 4D). By contrast, we detected less autophagy flux in the variants deficient in the LC3 interaction 7 motif (STING^{LIR7})⁵⁵ or in the binding to WD repeat domain phosphoinositide-interacting protein 2 (WIPI2; STING^{W2BD}),⁵⁶ both of which are required for the STING-LC3 interaction (Figure 4D). Notably, glutamate-induced autophagy flux was significantly higher in neurons expressing the STING^{W2BD} variant than in those expressing the STING^{LIR7} variant, indicating that factors additional to WIPI2 are required for STING-induced autophagy in neurons.

Additionally, *Stim1*-deficient neurons showed further increase in STING-dependent autophagy (Figures 4C, 4E, and S5H–S5L). Of note, baseline levels of autophagic flux and maximal autophagic capacity, measured after rapamycin treatment, were similar across all conditions (Figures S5M and S5N). To evaluate the necessity of the release of STING from the ER for STING-dependent autophagy, we compared neurons expressing STING with those expressing the ER-restricted STING^{ER}. After adding bafilomycin A1 and subsequent exposure to glutamate excitotoxicity or DMXAA, we recorded an increase in p62+ puncta, indicative of autophagosomes, in neurons expressing STING but not in those expressing STING^{ER} (Figure S5O). Together, our data show that a non-canonical autophagic STING pathway is activated in neurons.

To test whether the increased autophagic flux accounts for the STING-mediated increase in neuronal vulnerability to glutamate, we treated neurons expressing STING with various autophagy inhibitors. Indeed, the inhibitors 3-methyladenine, bafilomycin A1, SAR405 (SAR), and SBI0206965 (SBI)⁵⁷ reversed STING-induced neuronal vulnerability in both WT (Figures 4F, 4G, and S5P–S5R) and *Stim1*-deficient neurons (Figures 4H and 4I). These inhibitors did not affect neuronal viability in the absence of STING expression and provided no additional protection for *Sting1*-deficient neurons (Figure S5S). Furthermore, the expres-

sion of the STING Δ CT variant increased neuronal vulnerability to glutamate. This vulnerability was significantly reduced when expressing the STING^{W2BD} variant, was absent in neurons expressing the STING^{LIR7} variant, and aggravated when pharmacologically inhibiting TBK1 (Figures S5T and S5U). This collectively indicates that STING activated by ERCa²⁺D amplifies neuronal injury by inducing autophagy under inflammatory conditions.

STING-induced autophagy activates ferroptosis by degrading GPX4

Two distinct mechanisms of autophagy-dependent cell death have been described in cancer cells, which are unexplored in neurons. First, autophagy can activate Na⁺/K⁺-ATPase-dependent apoptosis, so-called autosis.⁵⁸ However, blocking the Na⁺/K⁺-ATPase using ouabain (Figure S6A) or applying the pan-caspase inhibitor carbobenzoxy-valyl-alanyl-aspartyl-[O-methyl]-fluoromethylketone (Z-VAD-FMK) (Figure S6B) did not reverse the increased vulnerability of STING-expressing neurons to glutamate. This advocates that autosis is not responsible for STING-induced autophagy-dependent cell death in neurons.

Thus, we focused on the second mechanism, ferroptosis, an iron-dependent cell death pathway. This pathway is robustly induced in cancer cells by autophagic degradation of the glutathione peroxidase 4 (GPX4),⁵⁹ which protects against (phospho) lipid peroxidation and is associated with ferroptosis. After glutamate exposure, GPX4 levels in soma and dendrites of neurons diminished rapidly, and this reduction was significantly higher in neurons expressing STING but not in those expressing STING^{ER} (Figures 5A and S6C). This was partially rescued by treatment with the STING inhibitor H151 and the autophagy inhibitors SAR and SBI (Figures 5B and 5C). The autophagy-driven degradation of GPX4 was evident by an increased number of GPX4-positive autophagosomes in neurons expressing STING following glutamate excitotoxicity, as indicated by GPX4⁺LC3⁺ puncta. This effect was reversed by pharmacologically inhibiting STING or autophagy (Figure 5D). Notably, neither baseline GPX4 levels were different in STING-expressing neurons, nor did H151, SAR, or SBI counteract the glutamate-induced GPX4 reduction in control or STING^{ER}-expressing neurons (Figures S6D and S6E). Additionally, the other known key regulators of ferroptosis, acyl-coenzyme A (CoA) synthetase long-chain family member 4 (ACSL4),⁶⁰ solute carrier family 7 member 11 (SLC7A11),⁶¹ and ferroptosis suppressor protein 1 (FSP1)⁶² were not differently expressed in STING-expressing neurons under steady state or after glutamate challenge (Figures S6F–S6H). These results indicate that STING induces autophagic degradation of GPX4 in neurons subjected to inflammation and excitotoxicity.

Next, we explored the functional relevance of autophagic GPX4 degradation in neurons. First, we measured the ratio between oxidized glutathione disulfide (GSSG) and total glutathione (GSH). The GSSG/GSH ratio is decisively modulated by GPX4 activity, as GPX4 reduces phospholipid hydroperoxides to their corresponding lipid alcohols at the expense of two molecules of reduced GSH, yielding di-glutathione (GSSG). As anticipated, glutamate exposure increased the GSSG/GSH ratio (Figure 5E) and decreased total GSH levels (Figure S7A), proving enzymatic activity of GPX4 in neurons under excitotoxic glutamate stress. Intriguingly, the increase of the GSSG/GSH ratio

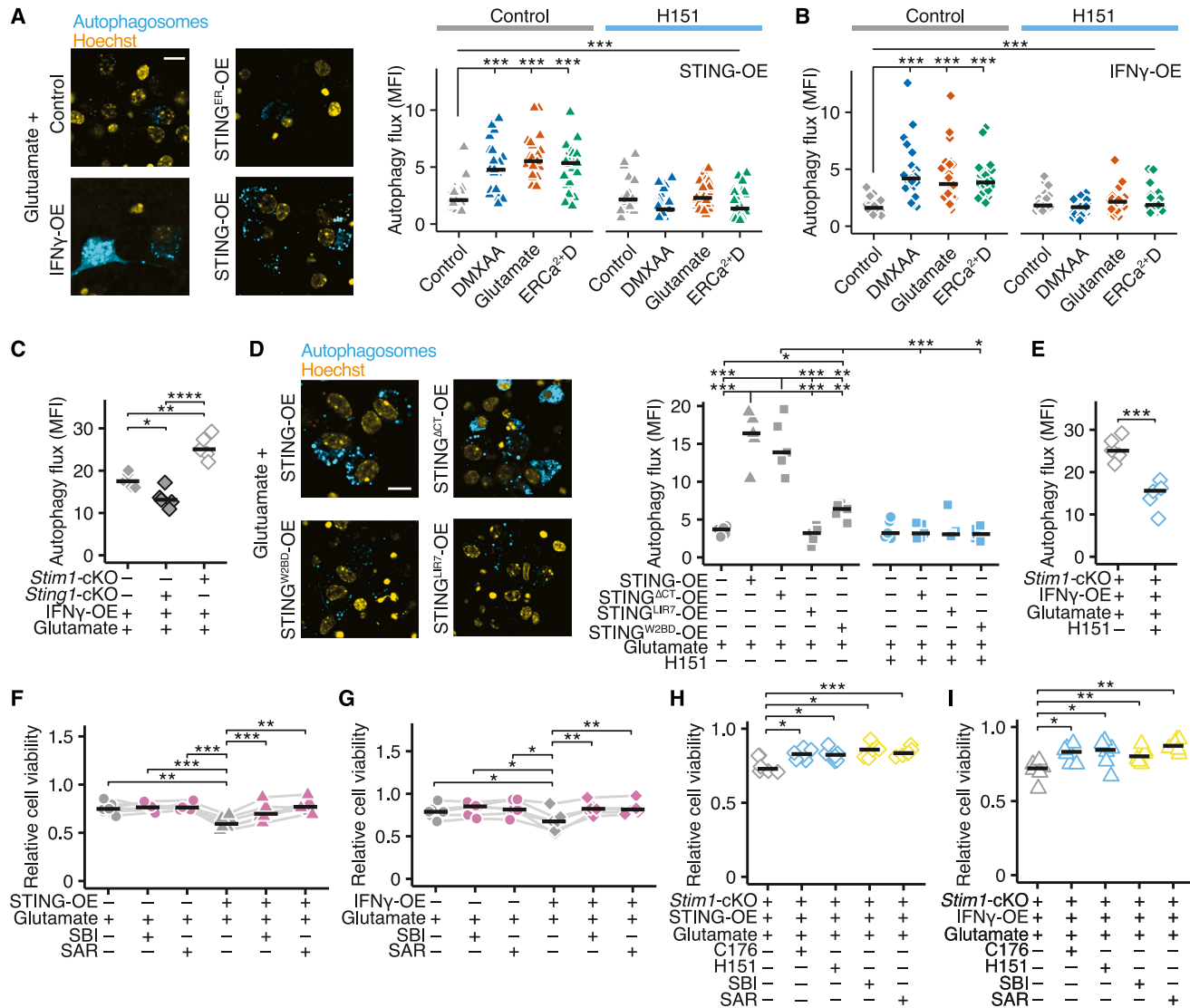


Figure 4. STING activates autophagy-dependent cell death in neurons

(A and B) Mean fluorescence intensity (MFI) of Cytold to measure autophagic flux in STING-OE (A) or IFN γ -OE (B) neurons that were treated with 50 nM bafilomycin A1 and were exposed to 50 μ g mL⁻¹ DMXAA, 50 μ M glutamate, or targeted ERCa²⁺D for 4 h and were additionally pre-treated with control or 1 μ M H151 (n = 20 per group from 5 different biological replicates). Scale bar shows 10 μ m.

(C) Autophagic flux in control, *Stim1*-cKO, and *Sting1*-cKO neurons that overexpress IFNG and were treated with 50 nM bafilomycin A1 and subsequently exposed to 50 μ M glutamate (n = 5 per group).

(D) Autophagic flux in neurons that overexpress STING, or the STING variants STING^{ACT}, STING^{W2BD}, or STING^{LIR7}, were treated with 50 nM bafilomycin A1 and subsequently treated with 1 μ M H151 or vehicle and exposed to 50 μ M glutamate for 4 h (n = 5 per group). Scale bar shows 10 μ m.

(E) Autophagic flux in *Stim1*-cKO neurons that overexpress IFNG was treated with 50 nM bafilomycin A1, subsequently exposed to 50 μ M glutamate, and pre-treated with control or 1 μ M H151 (n = 5 per group).

(F and G) Relative cell viability of STING-OE (M) and IFN γ -OE (N) neurons that were treated with glutamate and were pre-treated with the autophagy inhibitors 1 μ M SAR405 (SAR) and 1 μ M SBI-0206965 (SBI) (n = 6 per group). Paired t test was used.

(H and I) Relative cell viability of *Stim1*-cKO neurons that overexpress STING (H) or IFNG (I) and were treated with 1 μ M C176, 1 μ M H151, 1 μ M SBI, or 1 μ M SAR and were subsequently stimulated with 50 μ M glutamate (n = 6 per group). If not stated otherwise, unpaired t test with FDR correction for multiple comparisons was used, and independent experiments and the median are shown. * p < 0.05, ** p < 0.01, *** p < 0.001, **** p < 0.0001.

See also Figure S5.

after glutamate stimulation was absent in neurons expressing STING (Figure 5F), indicating a reduced activity of GPX4. GSSG/GSH ratio was restored by treating neurons with H151,

SBI, or SAR, as well as the antioxidant deferoxamine (Figure 5G). Notably, baseline GSSG/GSH ratio was comparable in neurons expressing STING, and the glutamate-induced decrease of total

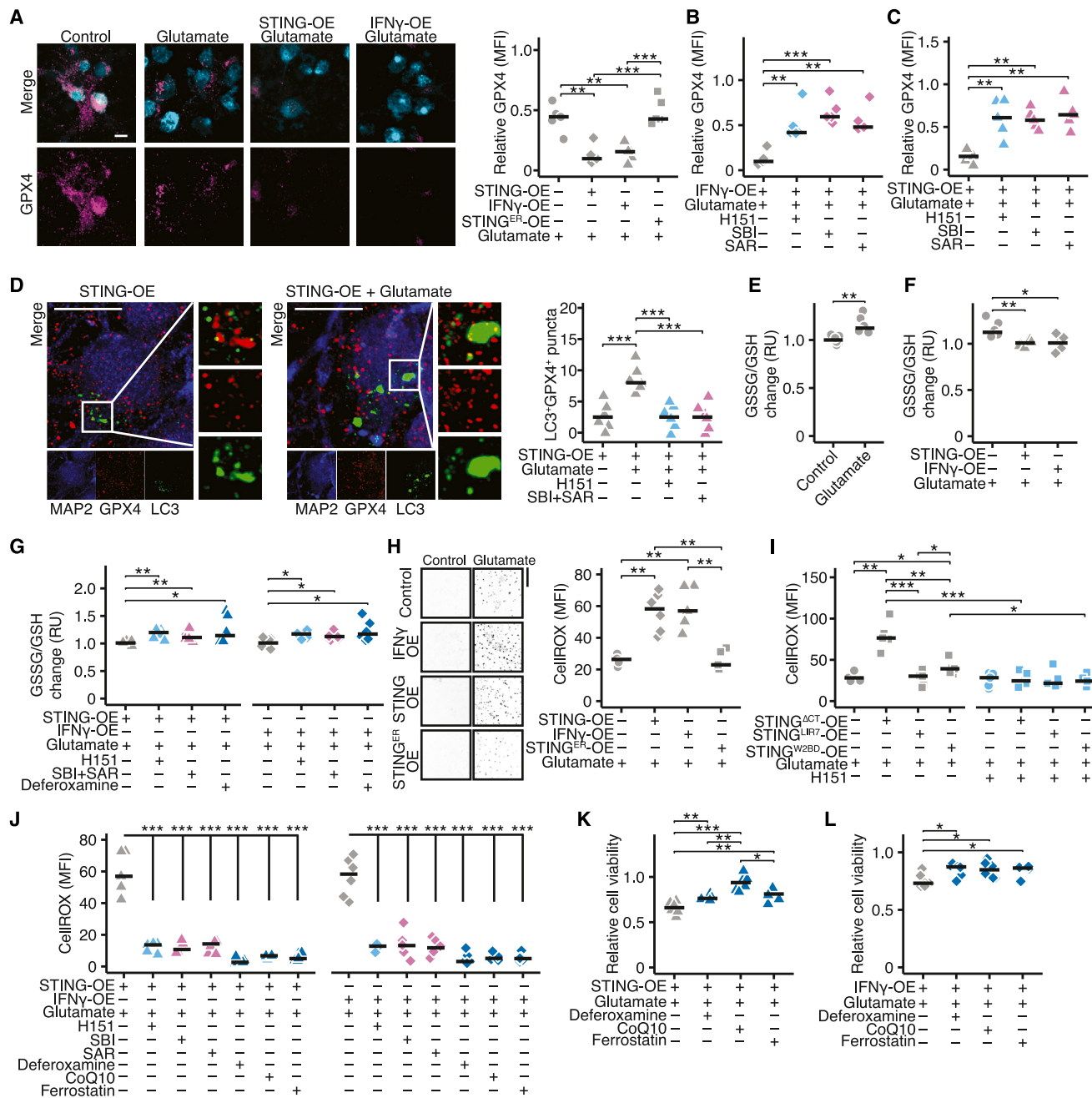


Figure 5. STING regulates ferroptosis in inflamed neurons

(A) Quantification of relative fold change of neuronal GPX4 mean fluorescence intensity (MFI) in neurons that overexpress STING (STING-OE), IFNG (IFN γ -OE), or STING^{ER} (STING^{ER}-OE) and were exposed to 50 μ M glutamate for 6 h ($n = 5$ per group). Data were normalized to controls (dashed line). NeuN is shown in cyan and GPX4 in magenta. Scale bar shows 10 μ m.

(B and C) Relative fold change of GPX4 MFI in neurons that overexpress IFNG (B) or STING (C) and were treated with 1 μ M H151, 1 μ M SBI-0206965 (SBI), or 1 μ M SAR405 (SAR) and were subsequently exposed to 50 μ M glutamate for 6 h ($n = 5$ per group).

(D) Number of LC3+GPX4+ puncta in STING-OE neurons that were transfected with EGFP-LC3 and were treated with 1 μ M H151 or 1 μ M SBI and 1 μ M SAR (SBI + SAR) and were subsequently exposed to 50 μ M glutamate for 6 h ($n = 6$). Scale bar shows 10 μ m.

(E) Relative fold change of the GSSG/GSH ratio in relative units (RUs) in neurons that were exposed to 50 μ M glutamate for 4 h ($n = 5$ per group).

(F) GSSG/GSH ratio in relative units (RUs) in neurons that overexpress STING or IFNG and were exposed to 50 μ M glutamate for 4 h ($n = 5$ per group). Data were normalized to respective unstimulated controls.

(G) GSSG/GSH fold change in relative units (RUs) in STING-OE or IFN γ -OE neurons that were treated with 1 μ M H151, 1 μ M SBI, and 1 μ M SAR or 20 μ M deferoxamine and were subsequently exposed to 50 μ M glutamate for 4 h ($n = 5$ per group).

(legend continued on next page)

GSH was not affected by neuronal STING expression (Figures S7B–S7E). Accordingly, STING-expressing neurons showed higher reactive oxygen species (ROS) levels after glutamate exposure in comparison with control or STING^{ER}-expressing neurons (Figures 5H and S7F). Furthermore, the STING^{ACT} variant significantly increased the glutamate-induced ROS production in neurons, a phenomenon that was much less pronounced in neurons expressing the STING^{W2BD} variant. Latter was at a similar level to that observed in glutamate-exposed control neurons and in neurons expressing the STING^{LIR7} variant (Figure 5I). This corroborates that the observed effects are independent of the canonical STING pathway. The ROS production could be rescued by treatments with H151, SBI, and SAR, as well as by the iron chelator deferoxamine and the radical trapping agents co-enzyme Q10 (CoQ10)⁶³ and ferrostatin⁶⁴ but not by the TBK1 inhibitor GSK-8612 (Figures 5J and S7G–S7J). Hence, STING disturbs the adaptive anti-oxidative response in inflamed neurons by autophagic degradation of GPX4. Since *Gpx4* deficiency results in activation of ferroptosis,⁶⁵ we hypothesized that STING acts as crucial regulator of inflammation-induced ferroptosis in neurons. Notably, treating neuronal cultures with the antioxidants deferoxamine, CoQ10, and ferrostatin protected STING-expressing neurons from glutamate excitotoxicity in WT (Figures 5K, 5L, S7K, and S7L) and in *Stim1*-deficient neurons (Figures S7M–S7O). Thus, STING emerges as a decisive gatekeeper of neuronal autophagy-dependent ferroptosis in neuroinflammation.

Since it has been controversially debated whether homeostatic cGAS activity is required to produce low levels of cGAMP that continuously drive STING trafficking and signaling,⁶⁶ we explored whether cGAS is also involved in the here described glutamate-induced STING-mediated ferroptosis in neurons. We generated *Cgas*-deficient neurons (Figure S8A) and induced STING expression by lentiviral transduction or chronic exposure of IFN γ . The increase in autophagy flux (Figure S8B), degradation of GPX4 (Figures S8C and S8D), and ROS production (Figure S8E) induced by glutamate excitotoxicity in STING-expressing neurons were similar between WT and *Cgas*-deficient neurons. Of note, *Cgas*-deficient neurons without STING expression were less susceptible to glutamate excitotoxicity, indicating a distinct physiological role of cGAS in neurons in the absence of STING (Figure S8F). We concluded that STING-induced ferroptosis induced by glutamate excitotoxicity is likely independent of cGAS in neurons.

STING inhibition as a strategy to ameliorate inflammation-induced neurodegeneration

Since GPX4 is downregulated in neurons of pwMS⁶⁷ and EAE (Figure S9A), we explored the potential of STING inhibition as

therapeutic strategy in treating MS neurodegeneration. First, we analyzed neuronal STING expression in post-mortem brains of pwMS. Similar to EAE, STING was induced in cortical neurons in normal-appearing gray matter (NAGM) of people with progressive MS and in cortices of people with relapsing-remitting MS and active inflammation (Figure 6A). Given the extensive neuronal upregulation of STING, positioning it as a promising target for therapeutic intervention, we next treated EAE animals with the STING antagonists C176 or H151. Daily treatments starting from disease onset reduced the clinical disease score (Figures 6B, S9B, and S9C) and neuronal loss (Figure 6C). Of note, mice treated with the STING antagonists showed lower levels of the autophagy marker LC3 (Figure S9D) and of the ferroptosis marker 4-hydroxy-2-nonenal (4-HNE; Figure 6D) accompanied by an increased GPX4 expression in neurons (Figure 6E). By contrast, *Stim1*-cKO EAE mice displayed lower GPX4 levels and higher LC3 and 4-HNE levels, supporting that autophagy-dependent ferroptosis is exacerbated in the absence of STIM1 (Figures S9E–S9G). Thus, pharmacological STING antagonists reduce inflammation-induced ferroptosis in neurons.

However, as expected from the strong activating role of STING in microglia, we found a reduced number of activated microglia⁴⁰ in treated EAE mice (Figure S9H). To bypass the dampening effect of STING antagonists on microglia activation,⁴⁶ we subjected our neuron-specific *Sting1*-cKO mice to EAE. Strikingly, *Sting1*-cKO mice showed an ameliorated disease course (Figures 6F, S9I, and S9J), as evidenced by an increased number of surviving neurons (Figure 6G), decreased immunostaining against neuronal LC3 (Figure S9K) and 4-HNE (Figure 6H), as well as increased levels of GPX4 (Figure 6I). Notably, we did not observe differences in the number of microglia and CNS-infiltrating immune cells between WT and *Sting1*-cKO EAE mice (Figures S9L, S10A, and S10B). However, we recorded higher levels of triggering receptor expressed on myeloid cells 2 (TREM2) on microglia in *Sting1*-cKO EAE mice, indicating a more homeostatic phenotype likely resulting from less neurodegeneration (Figure S10C). Collectively, our data strongly advocate that inhibiting STING is an exceptional example for a treatment paradigm that directly intervenes in the NISR during neuroinflammatory conditions and is thereby neuroprotective.

DISCUSSION

In this study, we discovered neuronal STING as a central component in the cascade leading to inflammation-induced neurodegeneration. Specifically, we identified a mechanism for STING activation that occurs through calcium signaling alone. We demonstrate that during inflammation, in response to IFN γ exposure, STING is expressed in CNS neurons. It is retained at the ER

(H) Quantification of CellROX MFI in STING-OE, IFN γ -OE, or STING^{ER}-OE neuronal cultures that were exposed to glutamate for 2 h ($n = 6$ per group).

(I) CellROX MFI in neurons that overexpress the STING variants STING^{ACT}, STING^{W2BD}, or STING^{LIR7} and were treated with 1 μ M H151 or vehicle and were subsequently exposed to 50 μ M glutamate for 2 h ($n = 5$ per group).

(J) CellROX MFI in STING-OE or IFN γ -OE neuronal cultures that were treated with 1 μ M H151, 1 μ M SAR, 1 μ M SBI, 20 μ M deferoxamine, 6 μ M co-enzyme Q10 (CoQ10), or 1 μ M ferrostatin and were subsequently exposed to 50 μ M glutamate for 2 h ($n = 6$ per group). Data were compared with untreated controls.

(K and L) Relative cell viability of STING-OE (K) or IFN γ -OE (L) neurons that were treated with 20 μ M deferoxamine, 6 μ M CoQ10, 1 μ M ferrostatin and were subsequently exposed to 50 μ M glutamate ($n = 6$ per group). If not stated otherwise, unpaired t test with FDR correction for multiple comparisons was used, and independent experiments and the median are shown. * $p < 0.05$, ** $p < 0.01$, *** $p < 0.001$.

See also Figures S6–S8.

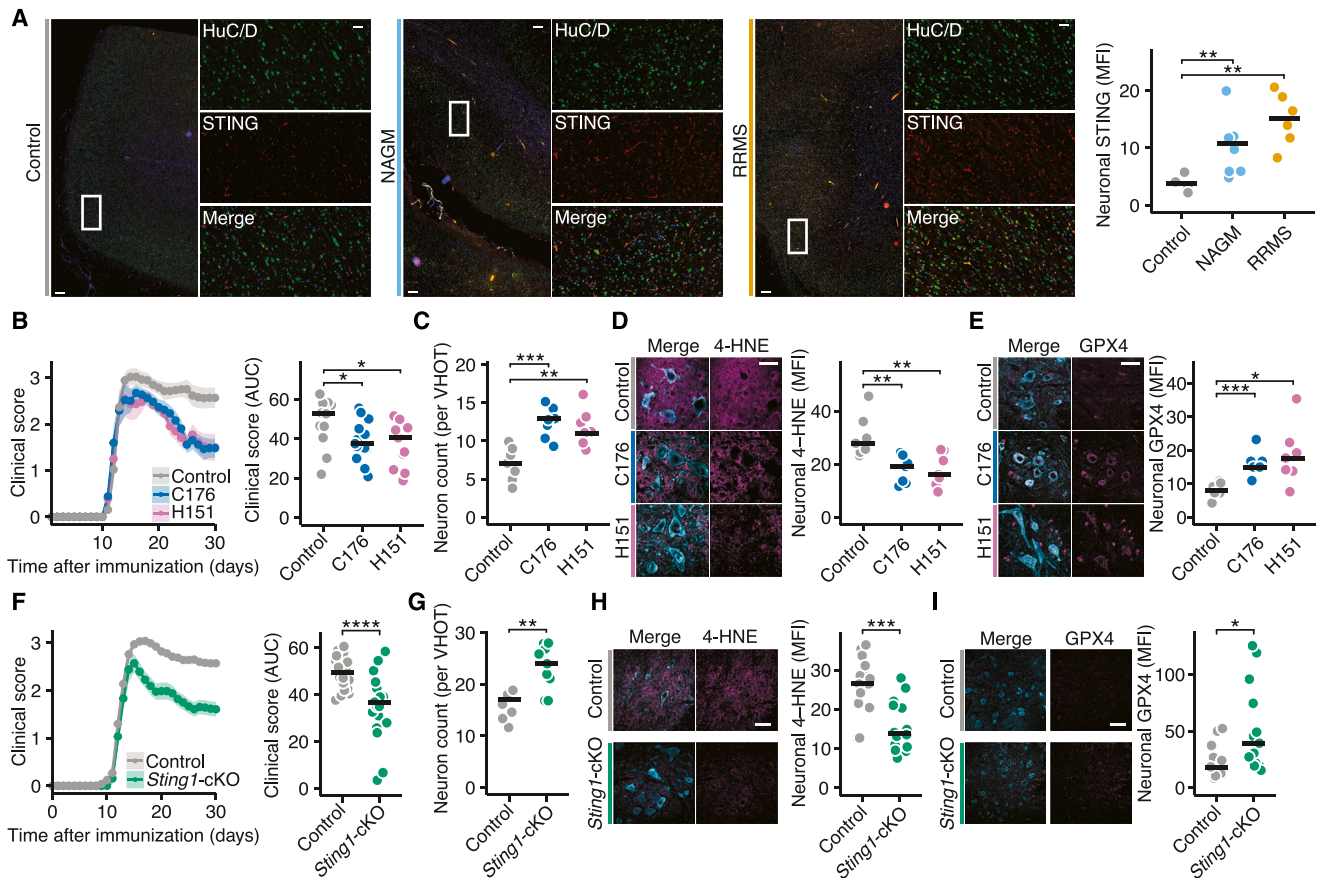


Figure 6. STING inhibition protects from inflammation-induced neurodegeneration

(A) Mean fluorescence intensity (MFI) in immunohistochemistry of STING measured in HuC/D-positive neurons of post-mortem cortices of non-neurological disease controls ($n = 4$), normal-appearing gray matter (NAGM) of people with progressive MS ($n = 7$), and actively inflamed cortex of people with relapsing MS ($n = 6$). The white box in the overview outlines the magnified area. Scale bar shows $500 \mu\text{m}$ in overview and $50 \mu\text{m}$ in magnified area.

(B) Clinical score and cumulative disease score (area under the curve [AUC]) of EAE mice that were treated with vehicle ($n = 13$), C176 ($n = 13$), or H151 ($n = 10$) intraperitoneally (i.p.) daily since day of disease onset. EAE disease curves show the mean and standard error mean.

(C) Neuronal count in the spinal cord ventral horn outflow tract (VHOT) of EAE mice that were treated with vehicle ($n = 7$), C176 ($n = 7$), or H151 ($n = 7$) 30 days after immunization.

(D and E) Neuronal MFI of 4-hydroxy-2-nonenal (4-HNE; D) and GPX4 (E) co-labeled with NeuN (cyan) to identify neurons in ventral horn spinal cords of EAE mice that were treated with vehicle ($n = 7$), C176 ($n = 7$), or H151 ($n = 7$) 30 days after immunization. Scale bar shows $20 \mu\text{m}$.

(F) Clinical score and cumulative disease score (area under the curve [AUC]) of WT ($n = 25$) and *Sting1*-cKO EAE mice ($n = 21$). EAE disease curves show the mean and standard error mean.

(G) Neuronal count in the spinal cord ventral horn outflow tract (VHOT) of WT ($n = 8$) and *Sting1*-cKO ($n = 9$) EAE 30 days after immunization.

(H and I) Neuronal MFI of 4-hydroxy-2-nonenal (4-HNE; H) and GPX4 (I) co-labeled with NeuN (cyan) to identify neurons in ventral horn spinal cords of WT ($n = 14$) and *Sting1*-cKO ($n = 13$) EAE mice 30 days after immunization. Scale bar shows $20 \mu\text{m}$. For comparing EAE phenotypes non-parametric Mann-Whitney U test was used. If not stated otherwise, unpaired t test with FDR correction for multiple comparisons was used, and individual mice and the median are shown. * $p < 0.05$, ** $p < 0.01$, *** $p < 0.001$, **** $p < 0.0001$.

See also [Figures S9](#) and [S10](#) and [Table S2](#).

through binding to STIM1, preventing its immediate activation. However, we discovered that a second stimulus, in the form of glutamate excitation, leads to STIM1 relocation, thereby allowing STING to travel to the Golgi apparatus, where it becomes activated^{39,66,68}. This highlights how two neuronal challenges, IFN γ and glutamate, jointly induce the NISR in MS and possibly in other neurodegenerative diseases.

Notably, this calcium-dependent STING activation in neurons was likely independent from the classical cGAS-mediated activation route⁶⁹ but solely required STING trafficking to the Golgi

apparatus. Thus, we provide clear evidence that trafficking-mediated STING signaling can be induced independently of classical dsDNA ligand-mediated⁶⁶ activation in neurons. Disease-relevant alterations in the trafficking-mediated STING activation route have mostly been centered around reduced lysosomal degradation, as observed in numerous lysosomal storage diseases.⁴⁷ Here we propose a framework for trafficking-mediated STING signaling in neurons, where glutamate-induced calcium depletion from the ER is a key initiator of STING phosphorylation by enabling its translocation to the

Golgi apparatus. Along these lines, we observed in [Figure 2D](#) two isoforms of STIM1, of which only the shorter one binds to STING. Indeed, two STIM1 splice variants, STIM1 and STIM1B, have been described. Intriguingly, the shorter STIM1B splice variant is exclusively expressed in neurons and decreased in neurons of Alzheimer's disease patients,⁷⁰ which might contribute to increased neuronal STING activation in other neurodegenerative diseases than MS. While pathologies in lysosomal storage diseases^{39,71} and other neurodegenerative diseases that impair lysosomal function, such as amyotrophic lateral sclerosis,⁷² are associated with less degradation of STING, we provide evidence that in inflammation-induced neurodegeneration, such as in MS, deleterious STING signaling is predominantly driven by a higher induction of STING phosphorylation rather than by less degradation of the protein.^{39,71} Intriguingly, STING phosphorylation and autophagy induction were not completely blocked by inhibiting TBK1 in neurons,⁷³ suggesting that alternative kinases might be regulating STING signaling in neurons.

Furthermore, we observed that the canonical type I IFN response was activated in EAE, independent of STING in neurons. This contrasts with dorsal root ganglion neurons of the PNS, where it directly contributes to activation of a type I IFN autocrine loop that inhibits nociception.⁷⁴ In CNS neurons, STING likely protects against neurotropic viruses but becomes detrimental during chronic neuroinflammation. This is due to continuous activation of a non-canonical signaling pathway,^{51,55,75} independent of TBK1 and IRF3 signaling, which induces autophagic degradation of GPX4, a key regulator of the oxidative balance in neurons,⁷⁶ leading to ROS build-up and ferroptosis.

This offers an explanation of how neurons sense and integrate different components of the inflammatory milieu and the mechanisms behind the suppression of GPX4 in inflamed neurons that eventually leads to the initiation of ferroptosis.⁶⁷ Notably, the signaling pathway we identified as detrimental in postmitotic cells can be therapeutically exploited in cancer. In the context of uncontrolled cell division, the hallmark of cancer, the pharmacological and genetic induction of autophagy increases GPX4 degradation and promotes ferroptosis.^{77,78} However, we show that STING-induced autophagy in neurons depends on the unc-51-like kinase 1 (ULK1) and employs WIPI2-independent mechanisms to increase autophagy in neurons, which is different in other cells.⁵⁵ As other distinct findings have been reported for several autophagy modulators like autophagy-related 9A (ATG9a)⁷⁹ or p62,⁸⁰ our study underlines the cell type specificity of STING signaling and regulation of ferroptosis.⁸¹

Our findings also illustrate how chronic CNS inflammation, particularly continuous IFN γ exposure, disrupts homeostatic regulatory mechanisms in neurons and leads to the activation of destructive signaling pathways. Meanwhile, in macrophages, GPX4 is required for STING activation, as it maintains the redox homeostasis. Without GPX4, STING trafficking is disturbed by lipid peroxides in macrophages.⁸² By contrast, neuronal STING trafficking to the Golgi apparatus and its activation are increased following glutamate-induced ROS production. This underscores the distinct mechanisms of interaction between STING and redox homeostasis in immune cells compared with neurons.

The neuronal STIM1-STING-GPX4 signaling cascade offers multiple intervention points in the NISR for developing treat-

ments to halt inflammation-induced neurodegeneration.⁸³ Indeed, using STING antagonists in EAE mice ameliorated the disease course and protected them from neuronal loss. STING signaling is known to drive CNS inflammation in mouse models of lysosomal storage disorders,⁸⁴ amyotrophic lateral sclerosis,⁴¹ and aging.⁴⁰ However, this has been largely attributed to the pro-inflammatory role of STING in microglia,^{40,85,86} as neuron-specific *Sting1* deletion has not been investigated. Given that pharmacological inhibition of STING is not cell type-specific, we provide *in vivo* evidence for the detrimental effect of neuronal, non-canonical STING signaling on inflammation-induced neurodegeneration. In particular, we demonstrate that neuron-specific deletion of *Sting1* improved the EAE disease course and reduced neuronal injury by decreasing autophagic GPX4 degradation, lipid peroxidation, and ferroptosis. This in turn also altered the response of the neuronal environment, as exemplified by more homeostatic microglia with higher TREM2 expression after neuron-specific *Sting1* deletion. Importantly, we observed an increase of STING expression not only in mouse neurons but also in neurons from pwMS, highlighting the clinical significance of our discovery. Since this neuron-specific STING pathway is activated downstream of glia-driven inflammation, STING within neurons is a critical and independent determinant of the outcome in inflammation-induced neurodegeneration. This likely applies to all inflammation-driven neurodegenerative processes, not just MS.

Our study provides insights into STING as a crucial mediator of inflammatory neuronal injury. It establishes a link between glutamate excitotoxicity, neuronal IFN signaling, and cell death. By controlling these converging pathways, STING emerges as a decisive regulator of the detrimental NISR and presents itself as a compelling pharmacological target for neuron-specific treatments aimed at combating neurodegeneration.

Limitations of the study

Our mechanistic study identifies STING as decisive initiator of ferroptosis, offering potential neuroprotective therapeutic strategies. However, some questions still warrant further investigation. First, although inhibition of the non-canonical neuronal STING signaling pathway provides substantial neuroprotection, it does not fully restore neuronal health. This suggests that several cell death pathways may be activated simultaneously, which should be considered in the conceptualization of new treatments. Second, while we have demonstrated that the relocation of STING from the ER to the Golgi apparatus is necessary for activating the autophagic degradation of GPX4, the precise molecular mechanisms in neurons are still not fully understood. Recently, STING has been identified as a proton channel that regulates autophagosome formation and inflammasome activation by controlling the proton flux of the Golgi apparatus.⁸⁷ This aspect warrants further investigation in neurons. Third, we used glutamate excitotoxicity with chronic IFN γ exposure as *in vitro* model for our mechanistic studies, which is a reduction of the complexity of inflammation-induced neurodegeneration. However, excitotoxicity seems to be an important driver of inflammation-induced neurodegeneration,^{10,88} and previous studies have successfully translated *in vitro* findings from neuronal cultures to EAE.^{10,67,89} More convincing *in vitro* models of inflammation-

induced demyelination and neurodegeneration are currently not available. Since demyelination is another important trigger of axonal injury in MS, subsequent studies should focus on STING in other mouse models of inflammation-independent demyelination. Lastly, although STING was observed exclusively in inflamed neurons, ferroptosis can be activated in neurons independently of inflammatory stimuli. Therefore, there have to be additional regulators of neuronal ferroptosis in neurodegeneration, which should be the focus of further investigations.

STAR★METHODS

Detailed methods are provided in the online version of this paper and include the following:

- **KEY RESOURCES TABLE**
- **RESOURCE AVAILABILITY**
 - Lead contact
 - Materials availability
 - Data and code availability
- **EXPERIMENTAL MODEL AND STUDY PARTICIPANT DETAILS**
 - Human subjects
 - Animals
 - Cells
- **METHOD DETAILS**
 - Vector construction
 - Lentiviral production and transduction
 - Generation of mouse neuronal cultures with conditional knockouts
 - Transfection of neuronal cultures and Neuro2a cells
 - Compounds and chemicals
 - Real-time PCR
 - Targeted ERCa²⁺D and SOCE
 - RealTime-Glo cell viability assay
 - Calcium imaging
 - GSSG/GSH-ratio estimation
 - ROS live cell imaging
 - Autophagic flux live cell imaging
 - Immunocytochemistry
 - Immunoprecipitation
 - Experimental autoimmune encephalomyelitis (EAE)
 - Cortical BacTRAP
 - RNA sequencing and analysis
 - Nucleus isolation and flow cytometric sorting
 - Mouse histopathology
 - Human histopathology
 - Immunoblot
 - Synaptoneurosomal fractionation
 - Immunophenotyping by flow cytometry
- **QUANTIFICATION AND STATISTICAL ANALYSIS**

SUPPLEMENTAL INFORMATION

Supplemental information can be found online at <https://doi.org/10.1016/j.cell.2024.05.031>.

ACKNOWLEDGMENTS

We thank the Friese laboratory for discussions. We thank the UKE vector facility for supplying viral vectors and for technical advice and the UKE Mouse Pathology Facility for immunohistochemistry. This work was funded by The Deutsche Forschungsgemeinschaft FOR 2289 (FR1720/9-1 and FR1720/9-2 to M.A.F. and FR1638/3-1 and FR1638/3-2 to M.F.), and SPP 2306 (CO291/9-1 and CO291/10-1 to M.C.), Deutsche Multiple Sklerose Gesellschaft (DMSG; grant number V 6.2 to M.A.F.), European Research Council (GA 884754 to M.C.), Joachim Herz Foundation (850035 to M.S.W.), Else Kröner Fresenius

Memorial Stipend (2023_EKMS.03 to M.S.W.), and the medMS doctoral program of the Gemeinnützige Hertie-Stiftung (P1180046 to L.C.B.).

AUTHOR CONTRIBUTIONS

M.S.W., C.M., and M.A.F. designed the study. M.S.W. and C.M. performed most experiments. M.S.W. performed bioinformatical analyses. L.B.-L., J.K.S., S.C.R., A.S., N.R., V.T., S.M.L., L.R., L.C.B., V.V., and S.B. helped with mouse experiments. M.G. provided human brain biopsies of MS patients. I.W. and D.M. performed immunostainings of post-mortem tissues. M.C. and M.F. provided expertise and reagents. M.S.W., C.M., and M.A.F. wrote the initial version of the manuscript. M.S.W. and M.A.F. supervised the study. M.A.F. funded the study. All co-authors contributed to the editing and discussion of the manuscript and approved the final version.

DECLARATION OF INTERESTS

The authors declare no competing interests.

Received: January 16, 2024

Revised: April 8, 2024

Accepted: May 16, 2024

Published: June 14, 2024

REFERENCES

1. Jakimovski, D., Bittner, S., Zivadnov, R., Morrow, S.A., Benedict, R.H., Zipp, F., and Weinstock-Guttman, B. (2024). Multiple sclerosis. *Lancet* 403, 183–202. [https://doi.org/10.1016/S0140-6736\(23\)01473-3](https://doi.org/10.1016/S0140-6736(23)01473-3).
2. Bierhansl, L., Hartung, H.-P., Aktas, O., Ruck, T., Roden, M., and Meuth, S.G. (2022). Thinking outside the box: non-canonical targets in multiple sclerosis. *Nat. Rev. Drug Discov.* 21, 578–600. <https://doi.org/10.1038/s41573-022-00477-5>.
3. Dangond, F., Donnelly, A., Hohlfeld, R., Lubetzki, C., Kohlhass, S., Leocani, L., Ciccarelli, O., Stankoff, B., Sormani, M.P., Chataway, J., et al. (2021). Facing the urgency of therapies for progressive MS — a Progressive MS Alliance proposal. *Nat. Rev. Neurol.* 17, 185–192. <https://doi.org/10.1038/s41582-020-00446-9>.
4. Faissner, S., Plemel, J.R., Gold, R., and Yong, V.W. (2019). Progressive multiple sclerosis: from pathophysiology to therapeutic strategies. *Nat. Rev. Drug Discov.* 18, 905–922. <https://doi.org/10.1038/s41573-019-0035-2>.
5. Attfeld, K.E., Jensen, L.T., Kaufmann, M., Friese, M.A., and Fugger, L. (2022). The immunology of multiple sclerosis. *Nat. Rev. Immunol.* 22, 734–750. <https://doi.org/10.1038/s41577-022-00718-z>.
6. Healy, L.M., Stratton, J.A., Kuhlmann, T., and Antel, J. (2022). The role of glial cells in multiple sclerosis disease progression. *Nat. Rev. Neurol.* 18, 237–248. <https://doi.org/10.1038/s41582-022-00624-x>.
7. Di Liberto, G., Pantelyushin, S., Kreutzfeldt, M., Page, N., Musardo, S., Coras, R., Steinbach, K., Vincenti, I., Klimek, B., Lingner, T., et al. (2018). Neurons under T Cell Attack Coordinate Phagocyte-Mediated Synaptic Stripping. *Cell* 175, 458–471.e19. <https://doi.org/10.1016/j.cell.2018.07.049>.
8. Andreadou, M., Ingelfinger, F., De Feo, D., Cramer, T.L.M., Tuzlak, S., Friebel, E., Schreiner, B., Eede, P., Schneeberger, S., Geesdorf, M., et al. (2023). IL-12 sensing in neurons induces neuroprotective CNS tissue adaptation and attenuates neuroinflammation in mice. *Nat. Neurosci.* 26, 1701–1712. <https://doi.org/10.1038/s41593-023-01435-z>.
9. Alves de Lima, K., Rustenhoven, J., Da Mesquita, S., Wall, M., Salvador, A.F., Smirnov, I., Martelossi Cebinelli, G., Mamuladze, T., Baker, W., Papadopoulos, Z., et al. (2020). Meningeal $\gamma\delta$ T cells regulate anxiety-like behavior via IL-17a signaling in neurons. *Nat. Immunol.* 21, 1421–1429. <https://doi.org/10.1038/s41590-020-0776-4>.
10. Woo, M.S., Ufer, F., Rothhammer, N., Di Liberto, G., Binkle, L., Haferkamp, U., Sonner, J.K., Engler, J.B., Hornig, S., Bauer, S., et al. (2021). Neuronal

- metabotropic glutamate receptor 8 protects against neurodegeneration in CNS inflammation. *J. Exp. Med.* 218, e20201290. <https://doi.org/10.1084/jem.20201290>.
- Schattling, B., Fazeli, W., Engeland, B., Liu, Y., Lerche, H., Isbrandt, D., and Friese, M.A. (2016). Activity of Nav1.2 promotes neurodegeneration in an animal model of multiple sclerosis. *JCI Insight* 1, e89810. <https://doi.org/10.1172/jci.insight.89810>.
 - Schattling, B., Steinbach, K., Thies, E., Kruse, M., Menigoz, A., Ufer, F., Flockerzi, V., Brück, W., Pongs, O., Vennekens, R., et al. (2012). TRPM4 cation channel mediates axonal and neuronal degeneration in experimental autoimmune encephalomyelitis and multiple sclerosis. *Nat. Med.* 18, 1805–1811. <https://doi.org/10.1038/nm.3015>.
 - Filiano, A.J., Xu, Y., Tustison, N.J., Marsh, R.L., Baker, W., Smirnov, I., Overall, C.C., Gadani, S.P., Turner, S.D., Weng, Z., et al. (2016). Unexpected role of interferon- γ in regulating neuronal connectivity and social behaviour. *Nature* 535, 425–429. <https://doi.org/10.1038/nature18626>.
 - Herz, J., Fu, Z., Kim, K., Dykstra, T., Wall, M., Li, H., Salvador, A.F., Zou, B., Yan, N., Blackburn, S.M., et al. (2021). GABAergic neuronal IL-4R mediates T cell effect on memory. *Neuron* 109, 3609–3618.e9. <https://doi.org/10.1016/j.neuron.2021.10.022>.
 - Kaya, T., Mattugini, N., Liu, L., Ji, H., Cantuti-Castelvetri, L., Wu, J., Schifferer, M., Groh, J., Martini, R., Besson-Girard, S., et al. (2022). CD8+ T cells induce interferon-responsive oligodendrocytes and microglia in white matter aging. *Nat. Neurosci.* 25, 1446–1457. <https://doi.org/10.1038/s41593-022-01183-6>.
 - Panagiotakopoulou, V., Ivanjuk, D., De Cicco, S., Haq, W., Arsić, A., Yu, C., Messelodi, D., Oldrati, M., Schöndorf, D.C., Perez, M.-J., et al. (2020). Interferon- γ signaling synergizes with LRRK2 in neurons and microglia derived from human induced pluripotent stem cells. *Nat. Commun.* 11, 5163. <https://doi.org/10.1038/s41467-020-18755-4>.
 - Lünemann, J.D., Jelčić, I., Roberts, S., Lutterotti, A., Tackenberg, B., Martin, R., and Münz, C. (2008). EBNA1-specific T cells from patients with multiple sclerosis cross react with myelin antigens and co-produce IFN- γ and IL-2. *J. Exp. Med.* 205, 1763–1773. <https://doi.org/10.1084/jem.20072397>.
 - Platanias, L.C. (2005). Mechanisms of type-I- and type-II-interferon-mediated signalling. *Nat. Rev. Immunol.* 5, 375–386. <https://doi.org/10.1038/nri1604>.
 - Sonekatsu, M., Taniguchi, W., Yamanaka, M., Nishio, N., Tsutsui, S., Yamada, H., Yoshida, M., and Nakatsuka, T. (2016). Interferon-gamma potentiates NMDA receptor signaling in spinal dorsal horn neurons via microglia–neuron interaction. *Mol. Pain* 12, 1744806916644927. <https://doi.org/10.1177/1744806916644927>.
 - Clark, D.N., O’Neil, S.M., Xu, L., Steppe, J.T., Savage, J.T., Raghunathan, K., and Filiano, A.J. (2023). Prolonged STAT1 activation in neurons drives a pathological transcriptional response. *J. Neuroimmunol.* 382, 578168. <https://doi.org/10.1016/j.jneuroim.2023.578168>.
 - Friese, M.A., Craner, M.J., Etzensperger, R., Vergo, S., Wemmie, J.A., Welsh, M.J., Vincent, A., and Fugger, L. (2007). Acid-sensing ion channel-1 contributes to axonal degeneration in autoimmune inflammation of the central nervous system. *Nat. Med.* 13, 1483–1489. <https://doi.org/10.1038/nm1668>.
 - Birkner, K., Wasser, B., Ruck, T., Thalman, C., Luchtman, D., Pape, K., Schmaul, S., Bitar, L., Krämer-Albers, E.-M., Stroh, A., et al. (2020). β 1-Integrin- and Kv1.3 channel-dependent signaling stimulates glutamate release from Th17 cells. *J. Clin. Invest.* 130, 715–732. <https://doi.org/10.1172/JCI126381>.
 - Yang, J., Vitery, M.D.C., Chen, J., Osei-Owusu, J., Chu, J., and Qiu, Z. (2019). Glutamate-Releasing SWELL1 Channel in Astrocytes Modulates Synaptic Transmission and Promotes Brain Damage in Stroke. *Neuron* 102, 813–827.e6. <https://doi.org/10.1016/j.neuron.2019.03.029>.
 - Hardingham, G.E., and Bading, H. (2010). Synaptic versus extrasynaptic NMDA receptor signalling: implications for neurodegenerative disorders. *Nat. Rev. Neurosci.* 11, 682–696. <https://doi.org/10.1038/nrn2911>.
 - Oh-hora, M., Yamashita, M., Hogan, P.G., Sharma, S., Lamperti, E., Chung, W., Prakriya, M., Feske, S., and Rao, A. (2008). Dual functions for the endoplasmic reticulum calcium sensors STIM1 and STIM2 in T cell activation and tolerance. *Nat. Immunol.* 9, 432–443. <https://doi.org/10.1038/ni1574>.
 - Zhang, S.L., Yu, Y., Roos, J., Kozak, J.A., Deerinck, T.J., Ellisman, M.H., Stauderman, K.A., and Cahalan, M.D. (2005). STIM1 is a Ca $^{2+}$ sensor that activates CRAC channels and migrates from the Ca $^{2+}$ store to the plasma membrane. *Nature* 437, 902–905. <https://doi.org/10.1038/nature04147>.
 - Witte, M.E., Schumacher, A.-M., Mahler, C.F., Bewersdorf, J.P., Lehmitz, J., Scheiter, A., Sánchez, P., Williams, P.R., Griesbeck, O., Naumann, R., et al. (2019). Calcium Influx through Plasma-Membrane Nanoruptures Drives Axon Degeneration in a Model of Multiple Sclerosis. *Neuron* 101, 615–624.e5. <https://doi.org/10.1016/j.neuron.2018.12.023>.
 - Gu, Z., Kalambogias, J., Yoshioka, S., Han, W., Li, Z., Kawasawa, Y.I., Pochareddy, S., Li, Z., Liu, F., Xu, X., et al. (2017). Control of species-dependent cortico-motoneuronal connections underlying manual dexterity. *Science* 357, 400–404. <https://doi.org/10.1126/science.aan3721>.
 - Doyle, J.P., Dougherty, J.D., Heiman, M., Schmidt, E.F., Stevens, T.R., Ma, G., Bupp, S., Shrestha, P., Shah, R.D., Doughty, M.L., et al. (2008). Application of a Translational Profiling Approach for the Comparative Analysis of CNS Cell Types. *Cell* 135, 749–762. <https://doi.org/10.1016/j.cell.2008.10.029>.
 - Srikanth, S., Woo, J.S., Wu, B., El-Sherbiny, Y.M., Leung, J., Chupradit, K., Rice, L., Seo, G.J., Calmettes, G., Ramakrishna, C., et al. (2019). The Ca $^{2+}$ sensor STIM1 regulates the type I interferon response by retaining the signaling adaptor STING at the endoplasmic reticulum. *Nat. Immunol.* 20, 152–162. <https://doi.org/10.1038/s41590-018-0287-8>.
 - Prabakaran, T., Troidborg, A., Kumpunya, S., Alee, I., Marinković, E., Windross, S.J., Nandakumar, R., Narita, R., Zhang, B.C., Carstensen, M., et al. (2021). A STING antagonist modulating the interaction with STIM1 blocks ER-to-Golgi trafficking and inhibits lupus pathology. *EBio-medicine* 66, 103314. <https://doi.org/10.1016/j.ebiom.2021.103314>.
 - Chen, C., and Xu, P. (2023). Cellular functions of cGAS-STING signaling. *Trends Cell Biol.* 33, 630–648. <https://doi.org/10.1016/j.tcb.2022.11.001>.
 - Ishikawa, H., Ma, Z., and Barber, G.N. (2009). STING regulates intracellular DNA-mediated, type I interferon-dependent innate immunity. *Nature* 461, 788–792. <https://doi.org/10.1038/nature08476>.
 - Li, X., Shu, C., Yi, G., Chaton, C.T., Shelton, C.L., Diao, J., Zuo, X., Kao, C.C., Herr, A.B., and Li, P. (2013). Cyclic GMP-AMP Synthase Is Activated by Double-Stranded DNA-Induced Oligomerization. *Immunity* 39, 1019–1031. <https://doi.org/10.1016/j.immuni.2013.10.019>.
 - Wu, J., Sun, L., Chen, X., Du, F., Shi, H., Chen, C., and Chen, Z.J. (2013). Cyclic GMP-AMP Is an Endogenous Second Messenger in Innate Immune Signaling by Cytosolic DNA. *Science* 339, 826–830. <https://doi.org/10.1126/science.1229963>.
 - Civril, F., Deimling, T., de Oliveira Mann, C.C., Ablasser, A., Moldt, M., Witte, G., Hornung, V., and Hopfner, K.-P. (2013). Structural mechanism of cytosolic DNA sensing by cGAS. *Nature* 498, 332–337. <https://doi.org/10.1038/nature12305>.
 - Sun, L., Wu, J., Du, F., Chen, X., and Chen, Z.J. (2013). Cyclic GMP-AMP Synthase Is a Cytosolic DNA Sensor That Activates the Type I Interferon Pathway. *Science* 339, 786–791. <https://doi.org/10.1126/science.1232458>.
 - Di Domizio, J.D., Gulen, M.F., Saidoune, F., Thacker, V.V., Yatim, A., Sharma, K., Nass, T., Guenova, E., Schaller, M., Conrad, C., et al. (2022). The cGAS-STING pathway drives type I IFN immunopathology in COVID-19. *Nature* 603, 145–151. <https://doi.org/10.1038/s41586-022-04421-w>.
 - Decout, A., Katz, J.D., Venkatraman, S., and Ablasser, A. (2021). The cGAS-STING pathway as a therapeutic target in inflammatory diseases. *Nat. Rev. Immunol.* 21, 548–569. <https://doi.org/10.1038/s41577-021-00524-z>.

40. Gulen, M.F., Samson, N., Keller, A., Schwabenland, M., Liu, C., Glück, S., Thacker, V.V., Favre, L., Mangeat, B., Kroese, L.J., et al. (2023). cGAS–STING drives ageing-related inflammation and neurodegeneration. *Nature* 620, 374–380. <https://doi.org/10.1038/s41586-023-06373-1>.
41. Yu, C.-H., Davidson, S., Harapas, C.R., Hilton, J.B., Mlodzianowski, M.J., Laohamonthonkul, P., Louis, C., Low, R.R.J., Moecking, J., De Nardo, D., et al. (2020). TDP-43 Triggers Mitochondrial DNA Release via mPTP to Activate cGAS/STING in ALS. *Cell* 183, 636–649.e18. <https://doi.org/10.1016/j.cell.2020.09.020>.
42. Liu, S., Cai, X., Wu, J., Cong, Q., Chen, X., Li, T., Du, F., Ren, J., Wu, Y.-T., Grishin, N.V., et al. (2015). Phosphorylation of innate immune adaptor proteins MAVS, STING, and TRIF induces IRF3 activation. *Science* 347, aaa2630. <https://doi.org/10.1126/science.aaa2630>.
43. Zhang, C., Shang, G., Gui, X., Zhang, X., Bai, X.C., and Chen, Z.J. (2019). Structural basis of STING binding with and phosphorylation by TBK1. *Nature* 567, 394–398. <https://doi.org/10.1038/s41586-019-1000-2>.
44. Dunphy, G., Flannery, S.M., Almine, J.F., Connolly, D.J., Paulus, C., Jönsson, K.L., Jakobsen, M.R., Nevels, M.M., Bowie, A.G., and Unterholzner, L. (2018). Non-canonical Activation of the DNA Sensing Adaptor STING by ATM and IFI16 Mediates NF- κ B Signaling after Nuclear DNA Damage. *Mol. Cell* 71, 745–760.e5. <https://doi.org/10.1016/j.molcel.2018.07.034>.
45. Thomson, D.W., PoECKel, D., Zinn, N., Rau, C., Strohmmer, K., Wagner, A.J., Graves, A.P., Perrin, J., Bantscheff, M., Duempelfeld, B., et al. (2019). Discovery of GSK8612, a Highly Selective and Potent TBK1 Inhibitor. *ACS Med. Chem. Lett.* 10, 780–785. <https://doi.org/10.1021/acs-medchemlett.9b00027>.
46. Kuchitsu, Y., Mukai, K., Uematsu, R., Takaada, Y., Shinjima, A., Shindo, R., Shoji, T., Hamano, S., Ogawa, E., Sato, R., et al. (2023). STING signaling is terminated through ESCRT-dependent microautophagy of vesicles originating from recycling endosomes. *Nat. Cell Biol.* 25, 453–466. <https://doi.org/10.1038/s41556-023-01098-9>.
47. Wang, A., Chen, C., Mei, C., Liu, S., Xiang, C., Fang, W., Zhang, F., Xu, Y., Chen, S., Zhang, Q., et al. (2024). Innate immune sensing of lysosomal dysfunction drives multiple lysosomal storage disorders. *Nat. Cell Biol.* 26, 219–234. <https://doi.org/10.1038/s41556-023-01339-x>.
48. Haag, S.M., Gulen, M.F., Reymond, L., Gibelin, A., Abrami, L., Decout, A., Heymann, M., van der Goot, F.G., Turcatti, G., Behrendt, R., et al. (2018). Targeting STING with covalent small-molecule inhibitors. *Nature* 559, 269–273. <https://doi.org/10.1038/s41586-018-0287-8>.
49. Jin, L., Hill, K.K., Filak, H., Mogan, J., Knowles, H., Zhang, B., Perraud, A.-L., Cambier, J.C., and Lenz, L.L. (2011). MPYS Is Required for IFN Response Factor 3 Activation and Type I IFN Production in the Response of Cultured Phagocytes to Bacterial Second Messengers Cyclic-di-AMP and Cyclic-di-GMP. *J. Immunol.* 187, 2595–2601. <https://doi.org/10.4049/jimmunol.1100088>.
50. Zhang, D., Liu, Y., Zhu, Y., Zhang, Q., Guan, H., Liu, S., Chen, S., Mei, C., Chen, C., Liao, Z., et al. (2022). A non-canonical cGAS–STING–PERK pathway facilitates the translational program critical for senescence and organ fibrosis. *Nat. Cell Biol.* 24, 766–782. <https://doi.org/10.1038/s41556-022-00894-z>.
51. Gui, X., Yang, H., Li, T., Tan, X., Shi, P., Li, M., Du, F., and Chen, Z.J. (2019). Autophagy induction via STING trafficking is a primordial function of the cGAS pathway. *Nature* 567, 262–266. <https://doi.org/10.1038/s41586-019-1006-9>.
52. Aman, Y., Schmauck-Medina, T., Hansen, M., Morimoto, R.I., Simon, A.K., Bjedov, I., Palikaras, K., Simonsen, A., Johansen, T., Tavernarakis, N., et al. (2021). Autophagy in healthy aging and disease. *Nat Aging* 1, 634–650. <https://doi.org/10.1038/s43587-021-00098-4>.
53. Kaizuka, T., Morishita, H., Hama, Y., Tsukamoto, S., Matsui, T., Toyota, Y., Kodama, A., Ishihara, T., Mizushima, T., and Mizushima, N. (2016). An Autophagic Flux Probe that Releases an Internal Control. *Mol. Cell* 64, 835–849. <https://doi.org/10.1016/j.molcel.2016.09.037>.
54. Tanaka, Y., and Chen, Z.J. (2012). STING Specifies IRF3 Phosphorylation by TBK1 in the Cytosolic DNA Signaling Pathway. *Sci. Signal.* 5, ra20. <https://doi.org/10.1126/scisignal.2002521>.
55. Liu, D., Wu, H., Wang, C., Li, Y., Tian, H., Siraj, S., Sehgal, S.A., Wang, X., Wang, J., Shang, Y., et al. (2019). STING directly activates autophagy to tune the innate immune response. *Cell Death Differ.* 26, 1735–1749. <https://doi.org/10.1038/s41418-018-0251-z>.
56. Wan, W., Qian, C., Wang, Q., Li, J., Zhang, H., Wang, L., Pu, M., Huang, Y., He, Z., Zhou, T., et al. (2023). STING directly recruits WIPI2 for autophagosome formation during STING-induced autophagy. *EMBO J.* 42, e112387. <https://doi.org/10.15252/emboj.2022112387>.
57. Kocak, M., Ezazi Erdi, S., Jorba, G., Maestro, I., Farrés, J., Kirkin, V., Martínez, A., and Pless, O. (2022). Targeting autophagy in disease: established and new strategies. *Autophagy* 18, 473–495. <https://doi.org/10.1080/15548627.2021.1936359>.
58. Liu, Y., Shoji-Kawata, S., Sumpster, R.M., Wei, Y., Ginet, V., Zhang, L., Posner, B., Tran, K.A., Green, D.R., Xavier, R.J., et al. (2013). Autosis is a Na⁺/K⁺-ATPase-regulated form of cell death triggered by autophagy-inducing peptides, starvation, and hypoxia-ischemia. *Proc. Natl. Acad. Sci. USA* 110, 20364–20371. <https://doi.org/10.1073/pnas.1319661110>.
59. Lee, S., Hwang, N., Seok, B.G., Lee, S., Lee, S.-J., and Chung, S.W. (2023). Autophagy mediates an amplification loop during ferroptosis. *Cell Death Dis.* 14, 464. <https://doi.org/10.1038/s41419-023-05978-8>.
60. Doll, S., Proneth, B., Tyurina, Y.Y., Panzilius, E., Kobayashi, S., Ingold, I., Irmiler, M., Beckers, J., Aichler, M., Walch, A., et al. (2017). ACSL4 dictates ferroptosis sensitivity by shaping cellular lipid composition. *Nat. Chem. Biol.* 13, 91–98. <https://doi.org/10.1038/nchembio.2239>.
61. Yan, Y., Teng, H., Hang, Q., Kondiparthi, L., Lei, G., Horbath, A., Liu, X., Mao, C., Wu, S., Zhuang, L., et al. (2023). SLC7A11 expression level dictates differential responses to oxidative stress in cancer cells. *Nat. Commun.* 14, 1–15. <https://doi.org/10.1038/s41467-023-39401-9>.
62. Nakamura, T., Hipp, C., Santos Dias Mourão, A., Borggräfe, J., Aldrovandi, M., Henkelmann, B., Wanninger, J., Mishima, E., Lytton, E., Emler, D., et al. (2023). Phase separation of FSP1 promotes ferroptosis. *Nature* 619, 371–377. <https://doi.org/10.1038/s41586-023-06255-6>.
63. Doll, S., Freitas, F.P., Shah, R., Aldrovandi, M., da Silva, M.C., Ingold, I., Goya Grocin, A., Xavier da Silva, T.N., Panzilius, E., Scheel, C.H., et al. (2019). FSP1 is a glutathione-independent ferroptosis suppressor. *Nature* 575, 693–698. <https://doi.org/10.1038/s41586-019-1707-0>.
64. Dixon, S.J., Lemberg, K.M., Lamprecht, M.R., Skouta, R., Zaitsev, E.M., Gleason, C.E., Patel, D.N., Bauer, A.J., Cantley, A.M., Yang, W.S., et al. (2012). Ferroptosis: An Iron-Dependent Form of Nonapoptotic Cell Death. *Cell* 149, 1060–1072. <https://doi.org/10.1016/j.cell.2012.03.042>.
65. Mishima, E., Ito, J., Wu, Z., Nakamura, T., Wahida, A., Doll, S., Tonnus, W., Nepachalovich, P., Eggenhofer, E., Aldrovandi, M., et al. (2022). A non-canonical vitamin K cycle is a potent ferroptosis suppressor. *Nature* 608, 778–783. <https://doi.org/10.1038/s41586-022-05022-3>.
66. Jeltama, D., Abbott, K., and Yan, N. (2023). STING trafficking as a new dimension of immune signaling. *J. Exp. Med.* 220, 1–14. <https://doi.org/10.1084/jem.20220990>.
67. Rothhammer, N., Woo, M.S., Bauer, S., Binkle-Ladisich, L., Di Liberto, G., Egervari, K., Wagner, I., Haferkamp, U., Pless, O., Merkler, D., et al. (2022). G9a dictates neuronal vulnerability to inflammatory stress via transcriptional control of ferroptosis. *Sci. Adv.* 8, eabm5500. <https://doi.org/10.1126/sciadv.abm5500>.
68. Paul, B.D., Snyder, S.H., and Bohr, V.A. (2021). Signaling by cGAS–STING in Neurodegeneration, Neuroinflammation, and Aging. *Trends Neurosci.* 44, 83–96. <https://doi.org/10.1016/j.tins.2020.10.008>.
69. Galluzzi, L., Vanpouille-Box, C., Bakhoum, S.F., and Demaria, S. (2018). SnapShot: CGAS-STING Signaling. *Cell* 173, 276–276.e1. <https://doi.org/10.1016/j.cell.2018.03.015>.

70. Ramesh, G., Jarzembowski, L., Schwarz, Y., Poth, V., Konrad, M., Knapp, M.L., Schwär, G., Lauer, A.A., Grimm, M.O.W., Alansary, D., et al. (2021). A short isoform of STIM1 confers frequency-dependent synaptic enhancement. *Cell Rep.* 34, 108844. <https://doi.org/10.1016/j.celrep.2021.108844>.
71. Yang, K., Tang, Z., Xing, C., and Yan, N. (2024). STING signaling in the brain: Molecular threats, signaling activities, and therapeutic challenges. *Neuron* 112, 539–557. <https://doi.org/10.1016/j.neuron.2023.10.014>.
72. McCauley, M.E., O'Rourke, J.G., Yáñez, A., Markman, J.L., Ho, R., Wang, X., Chen, S., Lall, D., Jin, M., Muhammad, A.K.M.G., et al. (2020). C9orf72 in myeloid cells suppresses STING-induced inflammation. *Nature* 585, 96–101. <https://doi.org/10.1038/s41586-020-2625-x>.
73. Ma, M., Dang, Y., Chang, B., Wang, F., Xu, J., Chen, L., Su, H., Li, J., Ge, B., Chen, C., et al. (2023). TAK1 is an essential kinase for STING trafficking. *Mol. Cell* 83, 3885–3903.e5. <https://doi.org/10.1016/j.molcel.2023.09.009>.
74. Donnelly, C.R., Jiang, C., Andriessen, A.S., Wang, K., Wang, Z., Ding, H., Zhao, J., Luo, X., Lee, M.S., Lei, Y.L., et al. (2021). STING controls nociception via type I interferon signalling in sensory neurons. *Nature* 591, 275–280. <https://doi.org/10.1038/s41586-020-03151-1>.
75. Zhang, R., Kang, R., and Tang, D. (2021). The STING1 network regulates autophagy and cell death. *Signal Transduct. Target. Ther.* 6, 208. <https://doi.org/10.1038/s41392-021-00613-4>.
76. Ingold, I., Berndt, C., Schmitt, S., Doll, S., Poschmann, G., Buday, K., Roveri, A., Peng, X., Porto Freitas, F., Seibt, T., et al. (2018). Selenium Utilization by GPX4 Is Required to Prevent Hydroperoxide-Induced Ferroptosis. *Cell* 172, 409–422.e21. <https://doi.org/10.1016/j.cell.2017.11.048>.
77. Liu, Y., Wang, Y., Liu, J., Kang, R., and Tang, D. (2021). Interplay between mTOR and GPX4 signaling modulates autophagy-dependent ferroptotic cancer cell death. *Cancer Gene Ther.* 28, 55–63. <https://doi.org/10.1038/s41417-020-0182-y>.
78. Sun, Y., Berleth, N., Wu, W., Schlütermann, D., Deitersen, J., Stuhldreier, F., Berning, L., Friedrich, A., Akgün, S., Mendiburo, M.J., et al. (2021). Fin56-induced ferroptosis is supported by autophagy-mediated GPX4 degradation and functions synergistically with mTOR inhibition to kill bladder cancer cells. *Cell Death Dis.* 12, 1028. <https://doi.org/10.1038/s41419-021-04306-2>.
79. Saitoh, T., Fujita, N., Hayashi, T., Takahara, K., Satoh, T., Lee, H., Matsu-naga, K., Kageyama, S., Omori, H., Noda, T., et al. (2009). Atg9a controls dsDNA-driven dynamic translocation of STING and the innate immune response. *Proc. Natl. Acad. Sci. USA* 106, 20842–20846. <https://doi.org/10.1073/pnas.0911267106>.
80. Prabakaran, T., Bodda, C., Krapp, C., Zhang, B.C., Christensen, M.H., Sun, C., Reinert, L., Cai, Y., Jensen, S.B., Skouboe, M.K., et al. (2018). Attenuation of cGAS-STING signaling is mediated by a p62/SQSTM1-dependent autophagy pathway activated by TBK1. *EMBO J.* 37, e97858. <https://doi.org/10.15252/embj.201797858>.
81. Dixon, S.J., and Olzmann, J.A. (2024). The cell biology of ferroptosis. *Nat. Rev. Mol. Cell Biol.* 25, 424–442. <https://doi.org/10.1038/s41580-024-00703-5>.
82. Jia, M., Qin, D., Zhao, C., Chai, L., Yu, Z., Wang, W., Tong, L., Lv, L., Wang, Y., Rehwinkel, J., et al. (2020). Redox homeostasis maintained by GPX4 facilitates STING activation. *Nat. Immunol.* 21, 727–735. <https://doi.org/10.1038/s41590-020-0699-0>.
83. Chitnis, T., and Weiner, H.L. (2017). CNS inflammation and neurodegeneration. *J. Clin. Invest.* 127, 3577–3587. <https://doi.org/10.1172/JCI90609>.
84. Chu, T.-T., Tu, X., Yang, K., Wu, J., Repa, J.J., and Yan, N. (2021). Tonic prime-boost of STING signalling mediates Niemann–Pick disease type C. *Nature* 596, 570–575. <https://doi.org/10.1038/s41586-021-03762-2>.
85. Reinert, L.S., Lopusná, K., Winther, H., Sun, C., Thomsen, M.K., Nandakumar, R., Mogensen, T.H., Meyer, M., Vægter, C., Nyengaard, J.R., et al. (2016). Sensing of HSV-1 by the cGAS–STING pathway in microglia orchestrates antiviral defence in the CNS. *Nat. Commun.* 7, 13348. <https://doi.org/10.1038/ncomms13348>.
86. Jin, M., Shiwaku, H., Tanaka, H., Obita, T., Ohuchi, S., Yoshioka, Y., Jin, X., Kondo, K., Fujita, K., Homma, H., et al. (2021). Tau activates microglia via the PQBP1–cGAS–STING pathway to promote brain inflammation. *Nat. Commun.* 12, 6565. <https://doi.org/10.1038/s41467-021-26851-2>.
87. Liu, B., Carlson, R.J., Pires, I.S., Gentili, M., Feng, E., Hellier, Q., Schwartz, M.A., Blainey, P.C., Irvine, D.J., and Hacohen, N. (2023). Human STING is a proton channel. *Science* 381, 508–514. <https://doi.org/10.1126/science.adf8974>.
88. Zhai, D., Yan, S., Samsom, J., Wang, L., Su, P., Jiang, A., Zhang, H., Jia, Z., Wallach, I., Heifets, A., et al. (2023). Small-molecule targeting AMPA-mediated excitotoxicity has therapeutic effects in mouse models for multiple sclerosis. *Sci. Adv.* 9, eadj6187. <https://doi.org/10.1126/sciadv.adj6187>.
89. Winkler, I., Engler, J.B., Vieira, V., Bauer, S., Liu, Y.-H., Di Liberto, G., Grochowska, K.M., Wagner, I., Bier, J., Bal, L.C., et al. (2023). MicroRNA-92a–CPEB3 axis protects neurons against inflammatory neurodegeneration. *Sci. Adv.* 9, eadi6855. <https://doi.org/10.1126/sciadv.adi6855>.
90. Nunes-Hasler, P., Maschalidi, S., Lippens, C., Castelbou, C., Bouvet, S., Guido, D., Bermont, F., Bassoy, E.Y., Page, N., Merkler, D., et al. (2017). STIM1 promotes migration, phagosomal maturation and antigen cross-presentation in dendritic cells. *Nat. Commun.* 8, 1852. <https://doi.org/10.1038/s41467-017-01600-6>.
91. Giuliano, C.J., Lin, A., Girish, V., and Sheltzer, J.M. (2019). Generating Single Cell-Derived Knockout Clones in Mammalian Cells with CRISPR/Cas9. *Curr. Protoc. Mol. Biol.* 128, e100. <https://doi.org/10.1002/cpmb.100>.
92. Chen, T.-W., Wardill, T.J., Sun, Y., Pulver, S.R., Renninger, S.L., Baohan, A., Schreier, E.R., Kerr, R.A., Orger, M.B., Jayaraman, V., et al. (2013). Ultrasensitive fluorescent proteins for imaging neuronal activity. *Nature* 499, 295–300. <https://doi.org/10.1038/nature12354>.
93. de Juan-Sanz, J., Holt, G.T., Schreiter, E.R., de Juan, F., Kim, D.S., and Ryan, T.A. (2017). Axonal Endoplasmic Reticulum Ca²⁺ Content Controls Release Probability in CNS Nerve Terminals. *Neuron* 93, 867–881.e6. <https://doi.org/10.1016/j.neuron.2017.01.010>.
94. Dynes, J.L., Amcheslavsky, A., and Cahalan, M.D. (2016). Genetically targeted single-channel optical recording reveals multiple Orai1 gating states and oscillations in calcium influx. *Proc. Natl. Acad. Sci. USA* 113, 440–445. <https://doi.org/10.1073/pnas.1523410113>.
95. Hirabayashi, Y., Kwon, S.-K., Paek, H., Pernice, W.M., Paul, M.A., Lee, J., Erfani, P., Raczkowski, A., Petrey, D.S., Pon, L.A., et al. (2017). ER-mitochondria tethering by PDZD8 regulates Ca²⁺ dynamics in mammalian neurons. *Science* 358, 623–630. <https://doi.org/10.1126/science.aan6009>.
96. Kabeya, Y., Mizushima, N., Ueno, T., Yamamoto, A., Kirisako, T., Noda, T., Kominami, E., Ohsumi, Y., and Yoshimori, T. (2000). LC3, a mammalian homologue of yeast Apg8p, is localized in autophagosomal membranes after processing. *EMBO J.* 19, 5720–5728. <https://doi.org/10.1093/emboj/19.21.5720>.
97. Dobin, A., Davis, C.A., Schlesinger, F., Drenkow, J., Zaleski, C., Jha, S., Batut, P., Chaisson, M., and Gingeras, T.R. (2013). STAR: ultrafast universal RNA-seq aligner. *Bioinformatics* 29, 15–21. <https://doi.org/10.1093/bioinformatics/bts635>.
98. Liao, Y., Smyth, G.K., and Shi, W. (2014). featureCounts: an efficient general purpose program for assigning sequence reads to genomic features. *Bioinformatics* 30, 923–930. <https://doi.org/10.1093/bioinformatics/btt656>.
99. Love, M.I., Huber, W., and Anders, S. (2014). Moderated estimation of fold change and dispersion for RNA-seq data with DESeq2. *Genome Biol.* 15, 550. <https://doi.org/10.1186/s13059-014-0550-8>.

100. Durinck, S., Spellman, P.T., Birney, E., and Huber, W. (2009). Mapping identifiers for the integration of genomic datasets with the R/Bioconductor package biomaRt. *Nat. Protoc.* *4*, 1184–1191. <https://doi.org/10.1038/nprot.2009.97>.
101. Platt, R.J., Chen, S., Zhou, Y., Yim, M.J., Swiech, L., Kempton, H.R., Dahlman, J.E., Parnas, O., Eisenhaure, T.M., Jovanovic, M., et al. (2014). CRISPR-Cas9 Knockin Mice for Genome Editing and Cancer Modeling. *Cell* *159*, 440–455. <https://doi.org/10.1016/j.cell.2014.09.014>.
102. Woo, M.S., Ufer, F., Sonner, J.K., Belkacemi, A., Tintelnot, J., Sáez, P.J., Krieg, P.F., Mayer, C., Binkle-Ladisch, L., Engler, J.B., et al. (2023). Calcium channel β 3 subunit regulates ATP-dependent migration of dendritic cells. *Sci. Adv.* *9*, eadh1653. <https://doi.org/10.1126/sciadv.adh1653>.
103. Sanjana, N.E., Shalem, O., and Zhang, F. (2014). Improved vectors and genome-wide libraries for CRISPR screening. *Nat. Methods* *11*, 783–784. <https://doi.org/10.1038/nmeth.3047>.
104. Poplawski, G.H.D., Kawaguchi, R., Van Niekerk, E., Lu, P., Mehta, N., Canete, P., Lie, R., Dragatsis, I., Meves, J.M., Zheng, B., et al. (2020). Injured adult neurons regress to an embryonic transcriptional growth state. *Nature* *581*, 77–82. <https://doi.org/10.1038/s41586-020-2200-5>.

STAR★METHODS

KEY RESOURCES TABLE

REAGENT or RESOURCE	SOURCE	IDENTIFIER
Antibodies		
4-hydroxy-2-nonenal	Abcam	Cat# ab46545; RRID: AB_722490
ACSL4	Santa Cruz	Cat# sc-365230; RRID: AB_10843105
Acti-Stain	Cytoskeleton	Cat# PHGD1
CD4 BV711	BioLegend	Cat# 100447; RRID: AB_2564586
CD8 α BV785	BioLegend	Cat# 100750; RRID: AB_2562610
CD11b BUV395	BD Bioscience	Cat# 563553; RRID: AB_2738276
CD11c PE/Cy7	BioLegend	Cat# 117318; RRID: AB_493568
CD19 BUV661	BD Bioscience	Cat# 612971; RRID: AB_2870243
CD45 APC/Cy7	BioLegend	Cat# 103116; RRID: AB_312981
CD68 BV785	BioLegend	Cat# 137035; RRID: AB_2860684
CD80 FITC	BioLegend	Cat# 104706; RRID: AB_313126
CD86 BUV496	BD Bioscience	Cat# 750437; RRID: AB_2874600
Clec7a PE/Cy7	eBioscience	Cat# 25-5859-80; RRID: AB_2573479
CX3CR1 PB	BioLegend	Cat# 149038; RRID: AB_2632857
F4/80 BV421	BioLegend	Cat# 123137; RRID: AB_2563102
FSP1	Santa Cruz	Cat# sc-377120; RRID: AB_2893240
GAPDH	Cell Signaling	Cat# 2118; RRID: AB_561053
GFP	Abcam	Cat# ab13970; RRID: AB_300798
Golgin-97	Cell Signaling	Cat# 13192; RRID: AB_2798144
Golgin-97	ThermoFisher	Cat# A21270; RRID: AB_221447
GPX4	Abcam	Cat# ab125066; RRID: AB_10973901
HuC/D	Invitrogen	Cat# A-21271; RRID: AB_221448
Ig chicken AF 488	Jackson Immuno	Cat# 703-545-155; RRID: AB_2340375
Ig chicken AF 647	Jackson Immuno	Cat# 703-606-155; RRID: AB_2340380
Ig chicken Cy3	Abcam	Cat# ab97145; RRID: AB_10679516
Ig mouse AF 647	Jackson Immuno	Cat# 715-605-151; RRID: AB_2340863
Ig mouse AF 405	Abcam	Cat# ab175658; RRID: AB_2687445
Ig rabbit AF 488	Abcam	Cat# ab150073; RRID: AB_2636877
Ig rabbit AF 555	Abcam	Cat# ab150074; RRID: AB_2636997
Ig rabbit AF 647	Abcam	Cat# ab150075; RRID: AB_2752244
Ig mouse HRP	LI-COR	Cat# 926-80010; RRID: AB_2721263
Ig rabbit HRP	LI-COR	Cat# 926-80011; RRID: AB_2721264
I-A/I-E BUV805	BD Bioscience	Cat# 748844; RRID: AB_2873247
IRF3	Cell Signaling	Cat# 4302; RRID: AB_1904036
Lamin B	Cell Signaling	Cat# 12586; RRID: AB_2650517
LC3	nanotools	Cat# 0231-100/LC3-5F10; RRID: AB_2722733
Ly6C PE	BioLegend	Cat# 128008; RRID: AB_1186132
Ly6G PerCP-Cy5.5	BioLegend	Cat# 127616; RRID: AB_1877271
NeuN	Abcam	Cat# EPR12763; RRID: AB_2732785
NeuN	Merck	RRID: AB_11205592
NF κ B	Invitrogen	Cat# PA1-186; RRID: AB_2539917
NK1.1 APC	BioLegend	Cat# 108710; RRID: AB_313396

(Continued on next page)

Continued

REAGENT or RESOURCE	SOURCE	IDENTIFIER
P2RY12 PE	BioLegend	Cat# 848004; RRID: AB_2721644
pIRF3	Cell Signaling	Cat# 29047; RRID: AB_2773013
pNFκB (Ser536)	Cell Signaling	Cat# 3033; RRID: AB_331284
pSTING (Ser365)	Cell Signaling	Cat# 72971; RRID: AB_2799831
pSTING (Ser365)	Cell Signaling	Cat# 62912; RRID: AB_2799635
pTBK1	Cell Signaling	Cat# 5483; RRID: AB_10693472
PSD95	Merck	Cat# MAB1596; RRID: AB_2092365
RFP	ThermoFisher	Cat# R10367; RRID: AB_2315269
SLC7A11	ThermoFisher	Cat# PA1-16893; RRID: AB_2286208
STIM1	Cell Signaling	Cat# 5668; RRID: AB_10828699
STIM1	Santa Cruz	Cat# sc-166840; RRID: AB_2198006
STING	Cell Signaling	Cat# 13647; RRID: AB_2732796
STING	Novus	Cat# NBP3-13941
Synapsin 1/2	Synaptic Systems	Cat# 106004; RRID: AB_1106784
TBK1	Santa Cruz	Cat# sc-398366
TCRβ BUV737	BD Bioscience	Cat# 612821; RRID: AB_2870145
TREM2	R&D Systems	Cat# FAB17291A; RRID: AB_884527
Vinculin	Merck	Cat# V9131; RRID: AB_477629
Zombie Green	BioLegend	Cat# 423112

Biological samples

Brain biopsies from healthy individuals and pwMS.	Brain biopsies at the University Medical Center Hamburg-Eppendorf	NA
Post-mortem brain autopsies from healthy individuals and pwMS.	UK biobank	https://www.ukbiobank.ac.uk/

Chemicals, peptides, and recombinant proteins

3-methyladenine	Santa Cruz	5142-23-4
Bafilomycin A1	Cayman Chemical	NSC 381866
C176	Selleckchem	S6575
CMA	biotechne	6677
Co-enzyme Q10	Merck	07386
Deferoxamine	Merck	138-14-7
DMXAA	Invitrogen	tlrl-dmx
EGTA	Merck	67-42-5
Ferostatin-1	Sigma	SML0583
Glutamate	Merck	106445
GSK-7975A	Merck	534351
GSK-8612	Merck	SML2721
H151	Selleckchem	S6652
Interferon-γ	preprotech	315-05
Ouabain	Tocris	1076
Poly I:C	invivogen	tlrl-pic
Rapamycin	Enzo	BML-A275
SAR405	Selleckchem	S7682
SBI-0206965	Selleckchem	S7885
Thapsigargin	Merck	586005
Z-VAD-FMK	Selleckchem	S8102

Critical commercial assays

CYTO-ID Autophagy detection kit	Enzo	ENZ-51031
CellROX green reagent	ThermoFisher Scientific	C10444

(Continued on next page)

Continued

REAGENT or RESOURCE	SOURCE	IDENTIFIER
GSH/GSSG-Glo Glutathione assay	Promega	V6611
RealTime-Glo	Promega	G9711
Deposited data		
Raw and analyzed data	This paper	GSE249192
Raw and analyzed data	Gene expression omnibus	GSE104899
Experimental models: Cell lines		
Bone marrow-derived dendritic cells	This paper	N/A
Neuro2a cells	DSMZ	ACC148
Primary neuronal cortical cultures	This paper	N/A
Experimental models: Organisms/strains		
C57BL/6J WT	The Jackson Laboratory	RRID:IMSR_JAX:000664
C57BL/6J Snap25-Cre x Sting ¹ ^{flox/flox}	This paper	N/A
C57BL/6J Snap25-Cre x Stim1 ^{flox/flox}	This paper	N/A
C57BL/6J Snap25-Cre x Stim2 ^{flox/flox}	This paper	N/A
GlT25d2-EGFP/L10a	The Jackson Laboratory	RRID:IMSR_JAX:030257
Rosa26-LSL-Cas9	The Jackson Laboratory	RRID:IMSR_JAX:026175
Oligonucleotides		
Primer_f1: TAGACCGGTATGGACTACAAGGATGACGATGAC AAGATGCCATACTCCAACCTGCATCCA	This paper	N/A
Primer_r1: TAGTCTAGAGATGAGGTCAGTGCGGAGTGG	This paper	N/A
Primer_r2: TAGTCTAGAGAGCTCATCTTTGATGAGGTCAGTG CGGAGTGG	This paper	N/A
Primer_f3: TAGACCGGTATGAACGCTACACACTGCATCTTGG	This paper	N/A
Primer_r3: TAGTCTAGAGCAGCGACTCCTTTTCCGCTTC	This paper	N/A
Primer_f4: TAGACCGGTATGGTGAGCAAGGGCGAGGAG	This paper	N/A
Primer_r4: TAGGAATTCTCACTACTTCTTAAGAGGCTTCTTA AAGATTTTG	This paper	N/A
Primer_f5: TAGCGTACGATGGACTACAAGGATGACGATGAC AAGATGCCATACTCCAACCTGCATCCA	This paper	N/A
Primer_r5: TAGAAGCTTTTCAGATGAGGTCAGTGCGGAGT	This paper	N/A
Primer_f6: TAGCGTACGATGCCATACTCCAACCTGCATCCA	This paper	N/A
Primer_r6: AATGAATTCTCAGATGAGGTCAGTGCGGAGTG	This paper	N/A
Primer_f7: AGCGTCGCCGAGATTGCGGAGAACGGA	This paper	N/A
Primer_r7: CGCAATCTCGGCGACGCTGTTGGAATAAACC	This paper	N/A
Primer_f8: CACTTGCAGCAATCCTGGCAGATGTC	This paper	N/A
Primer_r8: GACATCTGCCAGGATTGCCGCAAGTG	This paper	N/A
Primer_r9: AATGAATTCTCAAACCTCCTCTTTTCTTCTGACG	This paper	N/A
Oligo_f1: CACCGTGTGCGCCCGTCTTGCCCTG	This paper	N/A
Oligo_r1: aaacCAGGGCAAGACGGGCGCACAC	This paper	N/A
Oligo_f2: CACCGAATACAGGAGCTAGCTCCG	This paper	N/A
Oligo_r2: aaacCGGAGCTAGCTCCTGTATTC	This paper	N/A
Oligo_f3: CACCGAGACTTTCAGAAGTCGCCC	This paper	N/A
Oligo_r3: aaacGGGCGACTTCTGAAGAGTCTC	This paper	N/A
Oligo_f4: CACCGCTGATGGATGACGATGCCAA	This paper	N/A
Oligo_r4: aaacTTGGCATCGTCATCCATCAGC	This paper	N/A
Oligo_f5: CACCGCCAGCCATCCCACGGCCCAG	This paper	N/A
Oligo_r5: aaacCTGGGCGCTGGGATGGCTGGC	This paper	N/A
Oligo_f6: CACCGCAGTAGTCCAAGTTCGTGCG	This paper	N/A

(Continued on next page)

Continued

REAGENT or RESOURCE	SOURCE	IDENTIFIER
Oligo_r6: aaacCGCACGAACCTGGACTACTGC	This paper	N/A
Oligo_f7: CACCGTAGAATCATAGCCATACAG	This paper	N/A
Oligo_r7: aaacCTGTATGGCTATGATTCTAC	This paper	N/A
Oligo_f8: CACCGCAGTTGGATGTTTGGCCTTC	This paper	N/A
Oligo_r8: aaacGAAGGCCAAACATCCAACCTGC	This paper	N/A
Oligo_f9: CACCGAGATCCGCGTAGAAGGACGA	This paper	N/A
Oligo_r9: aaacTCGTCCTTCTACGCGGATCTC	This paper	N/A
Oligo_f10: CACCGGAGCGTGACGGGGACACCA	This paper	N/A
Oligo_r10: aaacTGGTGTCCCGTCACGCTCC	This paper	N/A
Oligo_f11: CACCGCTTACGACTTTCCGCGCCTC	This paper	N/A
Oligo_r11: aaacGAGGCGCGAAAGTCGTAAGC	This paper	N/A
Oligo_f12: CACCGGTTCTTCTCCTGGACCCTCG	This paper	N/A
Oligo_r12: aaacCGAGGGTCCAGGAAGGAACC	This paper	N/A
Primer_f1: TAGACCGGTATGGACTACAAGGATGACGATG ACAAGATGCCATACTCCAACCTGCATCCA	This paper	N/A
Primer_r1: TAGTCTAGAGATGAGGTCAGTGCGGAGTGG	This paper	N/A
Primer_r2: TAGTCTAGAGAGCTCATCTTTGATGAGGTCAG TGCGGAGTGG	This paper	N/A
Primer_f3: TAGACCGGTATGAACGCTACACACTGCATCTTGG	This paper	N/A
Primer_r3: TAGTCTAGAGCAGCGACTCCTTTTCCGCTTC	This paper	N/A
Primer_f4: TAGACCGGTATGGTGAAGGCGGAGGAG	This paper	N/A
Primer_r4: TAGGAATTCTCACTACTTCTTAAGAGGCTTCTTA AAGATTTTG	This paper	N/A
Primer_f5: TAGCGTACGATGGACTACAAGGATGACGATGAC AAGATGCCATACTCCAACCTGCATCCA	This paper	N/A
Primer_r5: TAGAAGCTTTCAGATGAGGTCAGTGCGGAGT	This paper	N/A
Primer_f6: TAGCGTACGATGCCATACTCCAACCTGCATCCA	This paper	N/A
Primer_r6: AATGAATTCTCAGATGAGGTCAGTGCGGAGTGG	This paper	N/A
Primer_f7: AGCGTCGCCGAGATTGCGGAGAACGGA	This paper	N/A
Primer_r7: CGCAATCTCGGCGACGCTGTTGGAATAAACC	This paper	N/A
Primer_f8: CACTTGCGGCAATCCTGGCAGATGTC	This paper	N/A
Primer_r8: GACATCTGCCAGGATTGCCGCAAGTG	This paper	N/A
Primer_r9: AATGAATTCTCAAACCTCCTCTTTTCTCCTGACG	This paper	N/A
Oligo_f1: CACCGTGTGCGCCCGTCTTGCCCTG	This paper	N/A
Oligo_r1: aaacCAGGGCAAGACGGGCGCACAC	This paper	N/A
Oligo_f2: CACCGAATACAGGAGCTAGCTCCG	This paper	N/A
Oligo_r2: aaacCGGAGCTAGCTCCTGTATTC	This paper	N/A
Oligo_f3: CACCGAGACTTCTCAGAAGTCGCCC	This paper	N/A
Oligo_r3: aaacGGGCGACTTCTGAAGAGTCTC	This paper	N/A
Oligo_f4: CACCGTGTGATGGATGACGATGCCAA	This paper	N/A
Oligo_r4: aaacTTGGCATCGTCATCCATCAGC	This paper	N/A
Oligo_f5: CACCGCCAGCCATCCACGGCCAG	This paper	N/A
Oligo_r5: aaacCTGGGCGCTGGGATGGCTGGC	This paper	N/A
Oligo_f6: CACCGCAGTAGTCCAAGTTCGTGCG	This paper	N/A
Oligo_r6: aaacCGCACGAACCTGGACTACTGC	This paper	N/A
Oligo_f7: CACCGTAGAATCATAGCCATACAG	This paper	N/A
Oligo_r7: aaacCTGTATGGCTATGATTCTAC	This paper	N/A
Oligo_f8: CACCGCAGTTGGATGTTTGGCCTTC	This paper	N/A

(Continued on next page)

Continued

REAGENT or RESOURCE	SOURCE	IDENTIFIER
Oligo_r8: aaacGAAGGCCAAACATCCAAGTGC	This paper	N/A
Oligo_f9: CACCGAGATCCGCGTAGAAGGACGA	This paper	N/A
Oligo_r9: aaacTCGTCTCTACGCGGATCTC	This paper	N/A
Oligo_f10: CACCGGAGCGTGACGGGGACACCA	This paper	N/A
Oligo_r10: aaacTGGTGTCCCGTCACGCTCC	This paper	N/A

Recombinant DNA

pMDLg/pRRE	Addgene	RRID: Addgene_12251
pRSV-Re	Addgene	RRID: Addgene_12253
pMDLg/pRRE	Addgene	RRID: Addgene_12259
mu-IFN γ -pCIneo	Addgene	RRID: Addgene_163517
p2K7bsdUBI-mCherry-STIM1	Nunes-Hasler et al. ⁹⁰	RRID: Addgene_114178
pMRX-IP-GFP-LC3-RFP-LC3 Δ G	Addgene	RRID: Addgene_84572
Lenti-Cas9-gRNA-GFP	Giuliano et al. ⁹¹	RRID: Addgene_124770
pAAV-Syn-Gcamp6f-WPRE-SV4088	Chen et al. ⁹²	RRID: Addgene_100837
ER-GcaMP6-210	de Juan-Sanz et al. ⁹³	RRID: Addgene_86919
Orai1-GcaMP6f	Dynes et al. ⁹⁴	RRID: Addgene_73564
pCAG Cyto-RCaMP1h	Hirabayashi et al. ⁹⁵	RRID: Addgene_105014
pEGFP-LC3	Kabeya et al. ⁹⁶	RRID: Addgene_21073
pAAV-hSyn-EGFP-mmSting1	This paper	N/A
L21-hSyn-mmSting1-P2a-mScarlet	This paper	N/A
pAAV-hSyn-EGFP-mmSting1-KDEL	This paper	N/A
L21-hSyn-mmSting1-KDEL-P2a-mScarlet	This paper	N/A
L21-hSyn-mScarlet-mmStim1	This paper	N/A
L21-hSyn-mmlfng-P2a-mScarlet	This paper	N/A
L21-hSyn-mmSting1-P2a-mScarlet	This paper	N/A
L21-hSyn-mmSting1-KDEL-P2a-mScarlet	This paper	N/A
L21-hSyn-mScarlet-P2a-mmSting1-LIR7	This paper	N/A
L21-hSyn-mScarlet-P2a-mmSting1-W2BD	This paper	N/A
L21-hSyn-mScarlet-P2a-mmSting1- Δ C-terminus	This paper	N/A
L21-hSyn-mScarlet-mmStim1	This paper	N/A

Software and algorithms

R	https://www.r-project.org/	https://www.r-project.org/
STAR	Dobin et al. ⁹⁷	https://github.com/alexdobin/STAR
featureCounts	Liao et al. ⁹⁸	https://subread.sourceforge.net/
DESeq2	Love et al. ⁹⁹	https://doi.org/10.18129/B9.bioc.DESeq2
biomaRT	Durinck et al. ¹⁰⁰	https://doi.org/10.18129/B9.bioc.biomaRT

RESOURCE AVAILABILITY

Lead contact

Further information and requests for resources and reagents should be directed to and will be fulfilled by the lead contact, Manuel A. Friese (manuel.friese@zmnh.uni-hamburg.de).

Materials availability

Plasmids and mouse lines generated in this study are available upon reasonable request from the corresponding author.

Data and code availability

- Bulk mRNA sequencing data have been deposited at Gene Expression Omnibus GEO: GSE249192 and are publicly available as of the date of publication. Accession numbers are listed in the [key resources table](#). This paper analyzes existing, publicly available data. These accession numbers for the datasets are listed in the [key resources table](#). All other data reported in this paper will be shared by the [lead contact](#) upon request.
- This paper does not report original code.
- Any additional information required to reanalyze the data reported in this paper is available from the [lead contact](#) upon request.

EXPERIMENTAL MODEL AND STUDY PARTICIPANT DETAILS

Human subjects

The specimen used for histopathology were obtained from brain biopsies or *post-mortem* autopsies of people where MS-typical changes were described by board-certified histopathologists, and the people had a MS diagnosis as determined by board-certified neurologists. The specimen was anonymized (cohort characteristics are provided in [Table S2](#)). The use of patient specimens for research upon anonymization was in accordance with local ethical standards and regulations at the University Medical Center Hamburg-Eppendorf. As human tissue could no longer be assigned to a human being, the analyses did not constitute a “research project on humans” in the sense of § 9 para. 2 of the Hamburg Chamber of Commerce Act for the Health Professions and therefore did not require consultation in accordance with § 15 para. 1 of the Professional Code of Conduct for Physicians in Hamburg.

Animals

All mice (C57BL/6J WT (The Jackson Laboratory); C57BL/6J *Snap25-Cre* x *Sting1^{flox/flox}*,¹⁰⁰ C57BL/6J *Snap25-Cre* x *Stim1^{flox/flox}*,²⁵ C57BL/6J *Snap25-Cre* x *Stim2^{flox/flox}*,²⁵ C57BL/6J *Rosa26-LSL-Cas9*,¹⁰¹ *Glit25d2-EGFP/L10a*²⁹ (The Jackson Laboratory)) were kept under specific pathogen-free conditions in the central animal facility of the University Medical Center Hamburg-Eppendorf (UKE). We used adult mice (6–20 weeks old) from both sexes; mice were sex- and age-matched in all experiments. We did not observe sex-specific differences in any of the experiments; therefore, the sexes were reported together. All animal care and experimental procedures were performed according to institutional guidelines and conformed to the requirements of the German legal authorities. Ethical approvals were obtained from the State Authority of Hamburg, Germany (approval No. 41/22).

Cells

Mouse primary neurons

For primary cortical cultures we euthanized pregnant C57BL/6J, or LSL-Cas9 mice. We isolated the cortex, dissociated, and plated cells at a density of 6×10^4 cells per 1 cm^2 on poly-D-lysine-coated wells ($5 \mu\text{M}$ Sigma-Aldrich). If not stated otherwise, cells were maintained in PNGM (Lonza) at 37°C , 5% CO_2 and a relative humidity of 98%. Throughout, we used cultures after 14–23 days *in vitro* (d.i.v.) for experiments. If indicated, we applied 100 ng/mL $\text{IFN}\gamma$ every day from 7 d.i.v. until the day of the experiment. Subsequent stimulations were carried out at 14–16 d.i.v. as described in the respective figure legends (all compounds and respective concentrations are provided in the section “[compounds and chemicals](#)”).

Mouse bone marrow-derived dendritic cells (BMDCs)

We obtained bone marrow from 6- to 12-week-old mice as described previously.¹⁰² Cells were homogenized through $40 \mu\text{m}$ cell strainers (Greiner) and incubated in red blood cell lysis buffer (0.15 M NH_4Cl , 10 mM KHCO_3 , and 0.1 mM Na_2EDTA in double-distilled H_2O at pH 7.4) for 5 min. We cultured the remaining cells in 10 mL cell culture flasks (Sarstedt) in mouse complete medium containing granulocyte-macrophage colony-stimulating factor (GM-CSF; 20 ng mL^{-1}) (PeproTech) at 37°C , 5% CO_2 and a relative humidity of 98%. We changed the medium every second day by carefully replacing the supernatant with fresh medium containing GM-CSF (20 ng mL^{-1}). We harvested semi-adherent BMDCs on day 6 to 8, unless stated otherwise. To validate the TBK1 inhibitor GSK-8612 we seeded 2×10^6 cells on 24-well plates that were treated with $10 \mu\text{M}$ or $50 \mu\text{M}$ GSK-8612 before adding $20 \mu\text{g mL}^{-1}$ DMXAA for 1 hour. After harvesting, immunoblot for pSTING and STING was performed as described below. To validate the activation of the canonical STING pathway, we seeded 2×10^6 BMDCs in 24-well plates and exposed them to $50 \mu\text{g mL}^{-1}$ DMXAA for 1 hour, 3 hours, 5 hours and 7 hours. After harvesting the cells, we performed immunoblot for pSTING, STING, pIRF3, IRF3, pTBK1, TBK1, and pNF κ B as described below.

Neuro2a cell line

Neuro2a cells (N2a, DSMZ ACC148) were grown at 37°C , 5% CO_2 and a relative humidity of 98% in T25 or T75 flasks (Sarstedt) in DMEM high glucose, GlutaMAX (Gibco) supplemented with 10% fetal bovine serum (PAN Biotech) and penicillin/streptomycin (50 U mL^{-1} , Gibco). At the desired time points, they were dissociated with TrypLE (Gibco) with 1 mM EDTA (Invitrogen) and seeded on poly-D-lysine-coated wells ($5 \mu\text{M}$ Sigma-Aldrich) at a density of 6×10^4 cells per 1 cm^2 , achieving 80%–90% confluence the following day. Transfection was performed as described below.

METHOD DETAILS

Vector construction

Sting1 was amplified from lymph node cDNA using primer_f1 and primer_r1. Primer_f1 additionally contained a FLAG tag for visualization. To generate an ER-retained STING variant (STING^{ER}), we used primer_r2 that contained a KDEL sequence. *Irfng* was amplified from the publicly available mu-IFN γ -pCIneo (mu-IFN γ -pCIneo was a gift from Thomas Weber (Addgene plasmid #163517; <http://n2t.net/addgene:163517>; RRID:Addgene_163517)) using primer_f3 and primer_r3. A mCherry-tagged STIM1 was amplified from p2K7bsdUBI-mCherry-STIM1 (p2K7bsdUBI-mCherry-STIM1 was a gift from Nicolas Demareux (Addgene plasmid #114178; <http://n2t.net/addgene:114178>; RRID:Addgene_114178))⁹⁰ using primer_f4 and primer_r4. The PCR amplification products were digested with the restriction enzymes AgeI and XbaI for 16 hours on 37 °C and were ligated into a customized lentiviral backbone with a human synapsin (hSyn) promoter (*Sting1*, *Sting1*^{ER}, *Stim1*) for neuron-specific expression or CMV promoter (*Irfng*) for ubiquitous expression. The expression plasmid additionally contained a mScarlet after a P2a domain to assess transduction efficacy. Furthermore FLAG-mm*Sting1* was amplified from lymph node cDNA using primer_f5 and primer_r5 and inserted behind a EGFP using BsiWI and HindIII as restriction enzymes. Thereby, a C-terminal EGFP-tagged STING variant under the control of a hSyn promoter was constructed. STING mutants, including STING^{LIR7} and STING^{W2BD} variants, were created using recombinant PCR. Outer primers primer_f6 and primer_r6, along with inner primers (primer_f7, primer_r7, primer_f8, and primer_r8), were employed to introduce specific amino acid substitutions. For the STING^{LIR7} mutant, substitutions Y478A and L481A were introduced, while for the STING^{W2BD} mutant substitutions E295A, E296A, and E299A were introduced. Additionally, the STING^{ACT} mutant, lacking amino acids 341–378, was generated via PCR with primers primer_f6 and primer_r9. All PCR products were then inserted into a lentivirus vector with the human synapsin promoter and an N-terminal mScarlet tag, using restriction enzymes Pfi23II and EcoRI. For inducing CRISPR knockouts of *Stim1* (oligos pairs 1–4), *Sting1* (oligo pairs 5–8), and *Cgas* (oligo pairs 9–12) we first annealed forward and reverse oligos which were digested with BsmBI for 6 hours on 37 °C and subsequently ligated either in Lenti-Cas9-gRNA-GFP (Lenti-Cas9-gRNA-GFP was a gift from Jason Sheltzer (Addgene plasmid #124770; <http://n2t.net/addgene:124770>; RRID:Addgene_124770))⁹¹ or a customized lentiviral backbone based on the lentiGuide Puro (lentiGuide-Puro was a gift from Feng Zhang (Addgene plasmid #52963))¹⁰³ that consists of the Cre recombinase under the control of the hSyn promoter and a guideRNA cassette under the control of a human U6 promoter. The Lenti-Cas9-*Sting1*/*Stim1*/*Cgas*-GFP constructs were transfected (see below for detailed description) in N2a cells to confirm the respective knockouts on genetic and protein levels. All final products were confirmed using Sanger sequencing. For all lentiviral overexpression experiments, a lentiviral mScarlet overexpression construct was used as control. If indicated the ER-retained form of STING (*Sting1*^{ER}) that does not travel to the Golgi apparatus was used as additional control.

Lentiviral production and transduction

To produce lentiviruses, we first transfected HEK293T cells with 10 μ g expression plasmid, 10 μ g pMDLg/pRRE, 5 μ g pRSV-Rev, 2 μ g pMD2.G. pMDLg/pRRE was a gift from Didier Trono (Addgene #12251; <http://n2t.net/addgene:12251>; RRID: Addgene_12251). pRSV-Rev was a gift from Didier Trono (Addgene #12253; <http://n2t.net/addgene:12253>; RRID: Addgene_12253). pMD2.G was a gift from Didier Trono (Addgene #12259; <http://n2t.net/addgene:12259>; RRID: Addgene_12259). Briefly, HEK293T cells were seeded with an 80% confluency in DMEM with glutamine and high glucose (ThermoFisher, cat. no. 10569010), the next day the plasmids were mixed in 1 \times HEPES buffered saline (HBS) and 125 mM CaCl₂ and were applied to the HEK293T cells for 6 hours. Subsequently, medium was changed and after 48 hours the supernatant was filtered through a 0.45 μ m PES filter, was immediately snap frozen and stored at –80 °C. Neurons were transduced at 7 d.i.v. with an efficacy of 80–90% which was visually confirmed by expression of a fluorescent protein. Control neurons were always included that were transduced with a mScarlet-carrying lentivirus. Chronic IFN γ exposure was achieved by delivering a lentivirus with an *Irfng* expressing construct controlled by a CMV promoter. The functionality of *Irfng* expression was confirmed by increased expression of the type II interferon downstream mediator signal transducer and activator of transcription 1 and its activated phosphorylated form.

Generation of mouse neuronal cultures with conditional knockouts

To generate *Sting1*-cKO, *Cgas*-cKO and *Stim1*-cKO neurons, neuronal cultures from LSL-Cas9 mice were transduced at 7 d.i.v. with lentiviruses that contained a Cre recombinase controlled by a hSyn promoter and respective guide RNAs (see above for detailed description). Per gene 4 guides were used to create pooled lentiviruses. The transduction efficacy was 70–80% estimated visually since all LSL-Cas9 cells that were transduced with a Cre recombinase express EGFP. We used neurons that were transduced with the same vectors containing non-targeted control gRNAs or gRNAs against LacZ.

Transfection of neuronal cultures and Neuro2a cells

Neuronal cultures were transfected at 1–3 d.i.v. with 500 ng DNA using lipofectamine 2000 (ThermoFisher, cat. no.11668019) according to the manufacturer's instruction. Neurons were incubated for 1 hour with DNA and lipofectamine and were subsequently washed for two times with preconditioned medium. Neuronal cultures were transfected with EGFP-STING and mCherry-STIM1 or EGFP-STING and an ER-retained mScarlet (mScarlet-KDEL, kind gift of Michael Kreutz) to visualize co-localization of STING with STIM1 or the ER. Furthermore, EGFP-LC3 (pEGFP-LC3 was a gift from Tamotsu Yoshimori (Addgene plasmid #21073; <http://n2t.net/addgene:21073>; RRID: Addgene_21073)) was transfected to visualize GPX4 colocalization after glutamate

stimulation. Neuro2a (N2a, DSMZ ACC148) cells were transfected using lipofectamine 2000 when 80% confluency was reached. N2a cells were incubated for 6 hours with DNA and lipofectamine and were subsequently washed for two times with preconditioned medium. N2a cells were transfected with EGFP-STING and mCherry-STIM1 to visualize colocalization.

Compounds and chemicals

Compounds were added to primary neurons at the indicated time points in the respective figure legends. For cell viability assays, the compounds were added 5 hours before glutamate was applied. If not stated otherwise, the following concentrations were used: 20 μ M 3-methyladenine, 50 nM bafilomycin A1, 1 μ M C176, 20 μ M CMA, 6 μ M c0-enzyme Q10, 20 μ M deferoxamine, 50 μ g/mL DMXAA, 2 mM EGTA, 1 μ M Ferrostatin-1, 50 μ M glutamate, 10 μ M GSK-7975A, 50 μ M GSK-8612, 1 μ M H151, 100 ng/mL interferon- γ , 1 μ M ouabain, 5 μ g/mL poly I:C, 500 nM rapamycin, 1 μ M SAR405, 1 μ M SBI0206965, 2 μ M thapsigargin, 20 μ M Z-VAD-FMK.

Real-time PCR

We reverse-transcribed RNA to complementary DNA with the RevertAid H Minus First Strand cDNA Synthesis Kit (Thermo Fisher Scientific) according to the manufacturer's instructions. We analyzed gene expression by real-time PCR performed in an ABI Prism 7900 HT Fast Real-Time PCR System (Applied Biosystems) using TaqMan Gene Expression Assays (Thermo Fisher Scientific) for *Acs14* (Mm00490331), *Actb* (Mm00607939), *Aifm2* (Mm00464061), *Cxcl10* (Mm00445235), *Gpx4* (Mm00433840), *Ifi44* (Mm00505670), *Ifnb1* (Mm00439552), *Tbp* (Mm01277042). We calculated gene expression as $2^{-\Delta Ct}$ relative to *Tbp* (mouse) or *Actb* as the endogenous control.

Targeted ERCa²⁺D and SOCE

Targeted ERCa²⁺D was achieved by depleting calcium in N2a cells or primary neurons. First, they were incubated in their respective medium with 2 mM EGTA for 30 minutes. Subsequently, we applied 2 μ M thapsigargin (Merck, T9033) for the indicated time frames up to 4 hours. For overnight ERCa²⁺D, afterwards we changed the medium to preconditioned medium with 2 mM EDTA (referred to as "ERCa²⁺D" in the figures). For initiating SOCE, we reintroduced calcium by changing the medium to preconditioned medium after 1 hour or 2 hours of ERCa²⁺D (referred to as "SOCE" in the figures). If indicated, we added 20 μ M of the CRAC-inhibitor GSK-7975A in the last medium change.

RealTime-Glo cell viability assay

We mixed RealTime-Glo (Promega, cat. no. G9711) MT cell viability substrate and NanoLuc Enzyme together, added it to neuronal cultures and incubated them for five hours for equilibration of luminescence signal before respective treatments were applied (all compounds and respective concentrations are provided in the section "compounds and chemicals"). Toxicity was estimated after applying 50 μ M glutamate. We recorded luminescence with a Spark 10M multimode microplate reader (Tecan) at 37 °C and 5% CO₂ every 30 min over a total time of 20–24 hours. We used at least four technical replicates per condition. For analysis every well's data point was normalized to its last value before the stressor was added and then normalized to the mean of the control wells for every time point. Thereby we controlled for well-to-well seeding variability. For statistical analysis we compared either area under curve (AUC) or end point.

Calcium imaging

We seeded primary neuronal cultures on either Ibidi 60 μ -Dish Quad (cat. no. 80411) or High (cat. no. 81158) with a glass bottom. To measure cytosolic calcium changes, we transduced neuronal cultures with an AAV7 that contained pAAV-Syn-Gcamp6f-WPRE-SV4088 (pAAV.Syn.GcaMP6f.WPRE.SV40 was a gift from Douglas Kim & GENIE Project (Addgene plasmid #100837; <http://n2t.net/addgene:100837>; RRID:Addgene_100837))⁹² at 8–12 d.i.v. with a 10,000–20,000 MOI. AAV particles were produced according to the standard procedures of the UKE vector facility. To visualize ER-calcium or calcium flux through ORAI1 we transfected ER-GcaMP6-210 (ER-GcaMP6-210 was a gift from Timothy Ryan (Addgene plasmid #86919; <http://n2t.net/addgene:86919>; RRID:Addgene_86919))⁹³ or Orai1-GcaMP6f (Orai1-GcaMP6f was a gift from Michael Cahalan (Addgene plasmid # 73564; <http://n2t.net/addgene:73564>; RRID:Addgene_73564))⁹⁴ using lipofectamine at 3 d.i.v. (see above for detailed description of lipofectamine transfection). We acquired images with a confocal LSM 700 laser scanning confocal microscope (Zeiss) every 0.48 seconds with a 20 \times magnification in an imaging chamber maintaining 37 °C and 5% CO₂. Infected cultures were imaged in the respective culture medium. In general, we recorded the first 5–10 minutes of baseline activity before applying the indicated chemicals. At the end of recording, we applied 10 μ M ionomycin to induce maximum cellular calcium response that was used for normalization. Specific assay details and concentrations can be found in the respective figure legend. For data analysis, we measured mean fluorescence values of every cell using Fiji software (NIH) and normalized it to the maximal calcium response after ionomycin challenge (indicated as F/F_{Max}). For each cell, we calculated maximal, minimal, mean and AUC of the calcium response using a custom R script. If not stated otherwise, AUC was used for statistical comparisons.¹⁰²

GSSG/GSH-ratio estimation

GSH/GSSG-Glo Glutathione assay (Promega) was used as described by the manufacturer. Primary cortical neurons were cultured in a 96-well plate and stimulated with glutamate for 4 hours. If indicated in the respective figures additional treatments were applied 30 minutes before glutamate stimulation. Cells were washed with pre-conditioned neuronal medium and GSH-Glo reagent was added to the wells for 30 min at room temperature, followed by the addition of luciferin detection reagent. After 15 min, luminescence was detected using a Spark 10M multimode microplate reader (Tecan). We used 4 technical replicates per condition for measuring GSSG and total glutathione (GSH). For final analysis, we compared the GSSG/GSH ratios between different conditions and genotypes.

ROS live cell imaging

For the detection of oxidative stress in response to glutamate treatment, CellROX green reagent (Thermo Fisher Scientific) was used. Neuronal cultures were stimulated with 50 μM glutamate for a total incubation time of 1 hour. If indicated in the respective figures additional treatments were applied 30 minutes before glutamate stimulation. CellROX reagent was added to the wells in a 5 μM final concentration after 30 minutes of glutamate stress. Hoechst 33342, a cell-permeant nuclear counterstain, was added at the same time. Cells were washed two times with pre-conditioned medium before image acquisition. The cells were subsequently imaged on a Zeiss LSM 700 confocal microscope using $\times 20$ magnification. Immunofluorescence of nuclear CellROX dye was quantified using Fiji (ImageJ).

Autophagic flux live cell imaging

To measure autophagic flux we used the CYTO-ID Autophagy detection kit (Enzo), a cationic amphiphilic tracer that selectively stains autophagic vacuoles. Neurons were incubated for 2 hours with 50 nM bafilomycin A1 and were subsequently treated for 2 hours with 50 μM glutamate. If indicated in the respective figures additional treatments were applied 30 minutes before glutamate stimulation. The CYTO-ID green reagent was applied 1.5 hours after glutamate application in a total dilution of 1:500. Hoechst 33342, a cell-permeant nuclear counterstain, was added at the same time. After 30 minutes neurons were washed two times in pre-conditioned neuronal medium and fluorescence was imaged on a Zeiss LSM 700 confocal microscope using $\times 20$ magnification or on a Zeiss LSM 900 Airyscan 2 microscope using $\times 40$ magnification. Additionally, neurons treated with 500 nM rapamycin, a well described inducer of autophagy was used as positive control. Quantification was performed using Fiji (ImageJ).

Furthermore, we measured LC3 degradation by lentiviral transduction of neurons with the pMRX-IP-GFP-LC3-RFP-LC3 ΔG ,⁵³ which was a gift from Noboru Mizushima (Addgene plasmid # 84572; <http://n2t.net/addgene:84572>; RRID: Addgene_84572). This plasmid expresses a GFP that is subject to autophagic degradation as well as a RFP transfection control. Thus, a lower GFP to RFP ratio indicates higher autophagy flux. Lentiviral production and transduction are described above in detail. Neurons were either treated with H₂O vehicle or 100 ng mL⁻¹ IFN γ daily from 7 d.i.v. to 15 d.i.v. At 15 d.i.v neurons were treated with either 1 μM H151, or 1 μM SAR405 together with 1 μM SBI-0206965 for 30 minutes and were subsequently exposed to 50 μM glutamate. The cells were fixed after in total 4 hours glutamate exposure and stained with antibodies against GFP and RFP. Images were acquired using a Zeiss LSM 900 Airyscan 2 microscope using $\times 63$ magnification. Quantification was performed using Fiji (ImageJ) and the ratio between GFP and RFP was compared between the different conditions.

Furthermore, we quantified LC3 and p62 accumulation after inhibiting lysosomal degradation of autophagosomes. For quantification of endogenous LC3 and p62, we transduced neuronal cultures after 7 d.i.v. with *Sting1*- or *Irfng*-expressing lentiviruses as described above and treated these cultures after 15 d.i.v. with 50 nM bafilomycin A1. After 1.5 hours we added 1 μM H151, or 1 μM SAR405 together with 1 μM SBI-0206965 for 30 minutes, subsequently we treated neurons with 50 μM glutamate for additional 4 hours. After PFA fixation, we performed immunostaining of LC3, acquired images using a Zeiss LSM 900 Airyscan 2 microscope at $\times 63$ magnification, and quantified LC3⁺ puncta with Fiji (ImageJ). Additionally, we used the same conditions to quantify the accumulation of transfected pEGFP-LC3,⁹⁶ which was a gift from Tamotsu Yoshimori (Addgene plasmid #21073; <http://n2t.net/addgene:21073>; RRID: Addgene_21073). The neuronal cultures were transfected at 2–4 d.i.v. as described above in detail. Subsequently, the same experimental setups and conditions were used as for quantification of endogenous LC3. We acquired images using a Zeiss LSM 900 Airyscan 2 microscope using $\times 63$ magnification, and quantified EGFP accumulation with Fiji (ImageJ).

In addition, we quantified the LC3-II/LC3-I ratio. We transduced neuronal cultures with either a mScarlet-expressing control or a *Sting1*-expressing lentivirus at 7 d.i.v. as described above. At 15 d.i.v. the neuronal cultures were treated for 4 hours with 50 μM glutamate. After cell harvesting and lysis, we performed immunoblotting as described above to visualize LC3-I and LC3-II. Using Fiji (ImageJ) we quantified the LC3-II/LC3-I ratio as marker of autophagy flux.

Immunocytochemistry

For immunocytochemistry, we cultivated neuronal cultures or N2a cells on 12 mm diameter coverslips. They were stimulated with 50 μM glutamate or when indicated additionally with respective treatments 30 minutes before adding glutamate (all compounds and respective concentrations are listed in the section “[compounds and chemicals](#)”). Subsequently, they were fixed with 4% paraformaldehyde (PFA) and incubated in 10% normal donkey’s serum (NDS) containing 0.1% Triton X-100 and was followed by immunolabeling. Images were acquired using a confocal LSM 700 laser scanning confocal microscope (Zeiss) or LSM 900 Airyscan 2 confocal microscope (Zeiss). The following antibody concentrations were used: ACSL4 1:200, Acti-Stain 1:70, FSP1 1:200, GFP

1:1,000, Golgin-97 (Cell Signaling) 1:100, Golgin-97 (ThermoFisher) 1:200, GPX4 1:100, HuC/D 1:100, Ig chicken AF488 1:500, Ig chicken AF647 1:500, Ig chicken Cy3 1:500, Ig mouse AF647 (Jackson Immuno) 1:500, Ig mouse AF647 (Abcam) 1:500, Ig rabbit AF488 1:500, Ig rabbit AF555 1:500, Ig rabbit AF647 1:500, LC3 1:100, NeuN 1:300, pSTING 1:200, RFP 1:1,000, SLC7A11 1:200, STIM1 1:300, STING 1:100.

Immunoprecipitation

For transfection, cells were seeded in two 10 cm cell culture dishes at a density of 6×10^4 cells per 1 cm^2 , achieving 80–90% confluence the following day. Transfections were performed using Lipofectamine 2000 (ThermoFisher) following the manufacturer's protocol as described above, with plasmids encoding N-terminal EGFP-tagged *Sting1* or *EGFP* alone. Twenty-four hours post-transfection, ERCa²⁺D was induced as described above. Afterwards cells were washed twice with ice-cold $1 \times$ PBS and lysed in HEPES buffer containing 0.5% CHAPS (Sigma), Complete protease inhibitor cocktail (Merck), 1 mM EDTA, 1 mM PMSF, and 1 mM DTT for 1 hour at 4 °C on an overhead shaker. Lysates were cleared by centrifugation at $20,000 \times g$ for 10 min, and 5% of the cleared lysate was retained as an input control. 50 μl of equilibrated GFP-Trap magnetic agarose beads (ChromoTek) were blocked in lysis buffer supplemented with 1 mg ml^{-1} BSA for 1 hour, then washed three times with HEPES washing buffer containing 0.05% CHAPS, 1 mM EDTA, 1 mM PMSF, and 1 mM DTT. Beads were incubated with cleared lysates for 1 hour at 4 °C on an overhead shaker to precipitate EGFP or EGFP-Stim1, respectively. Precipitates were washed five times with 500 μl washing buffer and boiled at 95 °C for 5 minutes in reducing sample buffer before being subjected to SDS-PAGE and immunoblotting. Membranes were incubated for 1 hour in blocking buffer (Tris-buffered saline + 0.1% Tween-20 (TBS-T) + 5% skim milk) before overnight incubation with primary antibodies (Rabbit Anti-STIM1 mAb D88E10 Cell Signaling #5668, Chicken Anti-GFP Abcam ab13970) in blocking buffer at 4 °C. Following three 5-minute washes with TBS-T, membranes were incubated with HRP-conjugated secondary antibodies in blocking buffer for 1 hour at room temperature. After an additional three 5-minute washes with TBS-T, detection was achieved using a chemiluminescence substrate (LI-COR).

Experimental autoimmune encephalomyelitis (EAE)

We immunized mice subcutaneously with 200 μg MOG35–55 peptide (Schafer-N) in CFA (Difco, cat. no. DF0639-60-6) containing 4 mg ml^{-1} *Mycobacterium tuberculosis* (Difco, cat. no. DF3114-33-8). In addition, we injected 200 ng pertussis toxin (Calbiochem, cat. no. CAS70323-44-3) intraperitoneally (i.p.) on the day of immunization and 48 hours later. We scored animals daily for clinical signs by the following system: 0, no clinical deficits; 1, tail weakness; 2, hind limb paresis; 3, partial hind limb paralysis; 3.5, full hind limb paralysis; 4, full hind limb paralysis and fore limb paresis; 5, premorbid or dead. Animals reaching a clinical score ≥ 4 were euthanized according to the regulations of the local animal welfare legal authorities. The investigators were blind to the genotype and treatment in the EAE experiments. For treatment studies mice were injected i.p. with 750 nmol C176 in 100 μL corn oil or 750 nmol H151 in 100 μL of 10% Tween-80 in PBS daily⁴⁸ starting with day of disease onset.

Cortical BacTRAP

TRAP was performed as described previously.¹⁰⁴ Briefly, Glt25d2-L10a-EGFP mice were anesthetized with ketamine/xylazine and perfused with 10 ml ice-cold dissection buffer ($1 \times$ Hank's Balanced Salt Solution, 2.5 mM HEPES-KOH, pH 7.4, 35 mM glucose, 4 mM NaHCO₃) over 1 minute. Cortices were dissected in ice-cold dissection buffer containing 100 $\mu\text{g ml}^{-1}$ cycloheximide; the cortices of two animals were pooled for homogenization in lysis buffer (20 mM HEPES-KOH, pH 7.4, 150 mM KCl, 5 mM MgCl₂, 0.5 mM dithiothreitol (DTT), 100 $\mu\text{g} \times \text{ml}^{-1}$ cycloheximide, 40 U $\times \text{ml}^{-1}$ Rnasin (Promega), 20 U $\times \text{ml}^{-1}$ SUPERase In Rnase Inhibitor (Invitrogen)) using a glass homogenizer. Homogenates were centrifuged at $2,000 \times g$ for 10 min at 4 °C to remove large cell debris. The supernatant was transferred to a new tube; NP-40 Surfact-Amps Detergent Solution (Thermo Fisher Scientific) and 1,2-dihexanoyl-sn-glycero-3-phosphocholine (Avanti Polar Lipids) were added to final concentrations of 1% and 30 mM, respectively. After 5 minute incubation on ice, lysates were centrifuged at $20,000 \times g$ for 10 minutes at 4 °C. Ten percent of the supernatant was saved as input control; the remaining 90% was incubated with monoclonal GFP antibody-coated (Htz-GFP19C8 and Htz-GFP19F7; Memorial Sloan Kettering Cancer Center Monoclonal Antibody Core Facility) magnetic beads (Streptavidin MyOne T1 Dynabeads (Invitrogen) pre-coupled to biotinylated Protein L (Pierce)) with end-over-end rotation overnight at 4 °C. Beads were subsequently collected on a magnetic rack, washed four times with high-salt wash buffer (20 mM HEPES, 350 mM KCl, 5 mM MgCl₂, 0.5 mM, 1% NP-40, 0.5 mM DTT, 100 $\mu\text{g ml}^{-1}$ cycloheximide) and immediately subjected to TRIzol/chloroform-based RNA extraction (Invitrogen). RNA was precipitated with sodium acetate and GlycoBlue (Thermo Fisher Scientific) in isopropanol overnight at $-80 \text{ }^\circ\text{C}$, washed twice with 70% ethanol, resuspended in water, and further purified using the Rneasy Micro Kit (Qiagen) with on-column Dnase I (Qiagen) digestion. For higher RNA yields, all steps were carried out in non-stick Ambion RNase Microfuge Tubes (Invitrogen).

RNA sequencing and analysis

RNA sequencing libraries were prepared using the TruSeq stranded mRNA Library Prep Kit (Illumina) according to the manufacturer's manual (document 1000000040498 v00). Libraries were pooled and sequenced on a NovaSeq 6000 sequencer (Illumina) generating 50 bp paired end reads. The reads were aligned to the Ensembl mouse reference genome (GRCh39) using STAR v.2.4⁹⁷ with default parameters. The overlap with annotated gene loci was counted with featureCounts v.1.5.1.⁹⁸ Differential expression analysis was

performed with DESeq2 (v.3.12)⁹⁹ calling genes with a minimal 2-fold change and false discovery rate (FDR)-adjusted $P < 0.05$ differentially expressed. Gene lists were annotated using biomaRt (v.4.0).

Nucleus isolation and flow cytometric sorting

Spinal cords of healthy and chronic EAE (30 days post immunization) WT and *Sting1*-cKO mice were explanted after PBS perfusion and stored at -80°C . Nuclei were isolated using the Nucleus Isolation Kit (Sigma-Aldrich; catalog no. NUC101) according to the manufacturer's protocol. Isolated nuclei were washed and labelled with an antibody against NeuN that is conjugated to Alexa Fluor 647 (Abcam, EPR12763) and propidium iodide to stain nuclei. We used flow cytometry to sort NeuN⁺PI⁺ nuclei with a BD FACSAria™ III Cell sorter (BD Bioscience).

Mouse histopathology

Mouse spinal cord tissue and cortex tissues was obtained and processed as described previously.¹² Images were acquired using a confocal LSM 700 or LSM 900 Airyscan 2 laser scanning confocal microscope (Zeiss). The following antibody concentrations were used: 4-HNE 1:100, GPX4 1:100, HuC/D 1:100, Ig chicken AF488 1:500, Ig chicken AF647 1:500, Ig chicken Cy3 1:500, Ig mouse AF647 (Jackson Immuno) 1:500, Ig mouse AF647 (Abcam) 1:500, Ig rabbit AF488 1:500, Ig rabbit AF555 1:500, Ig rabbit AF647 1:500, LC3 1:100, NeuN 1:300, pSTING 1:200, RFP 1:1,000, SLC7A11 1:200, STIM1 1:300, STING 1:100, IRF3 1:100, pIRF3 1:100, TBK1 1:100, pTBK1 1:100, NF κ B 1:200, pNF κ B 1:200.

Human histopathology

The brain biopsies used for this study contained only tissues that could not be used for diagnostic procedures. We deparaffinized the sections using a standard ethanol/xylol dilution. After rinsing the deparaffinized sections in water, we performed antigen retrieval using a sodium citrate buffer (pH = 6.5). After permeabilization with 0.1% Triton and blocking with 10% NDS, immunolabeling was performed with antibodies against NeuN (1:200; Millipore, ABN91), STIM1 (Santa Cruz; 1:100, cat. no. sc-166840), and DAPI. Images were acquired using a confocal LSM 700 laser scanning confocal microscope (Zeiss).

Human *post-mortem* brain tissues were acquired from the UK biobank. *Post-mortem* tissue processing was performed using standard fixation and embedding methods as described previously.⁹ Briefly, human CNS tissue was fixed in 4% formalin and embedded in paraffin, and 2 μm sections were mounted on a glass slide. Subsequently, tissue sections were deparaffinized, and antigen retrieval (Marmite Pascal Citrate pH 6.0) was performed. To prevent unspecific binding of primary antibodies, sections were incubated with normal goat serum (2.5 % in PBS) before two hours of incubation with the following primary antibodies: mouse IgG2b anti-HuC/HuD (Invitrogen, A-21271, 1/100), and rabbit anti-STING (Cell Signaling, 13647, 1/100). After washing, autofluorescence was removed (Merck, ref 2160) and bound primary antibodies were visualized using corresponding goat anti-mouse IgG2b AlexaFluor488 (Life, A21141), goat anti-mouse IgG1 AlexaFluor647 (Life, A21240) and donkey anti-rabbit IgG AlexaFluor 555 (Life, A31572). Nuclei counterstaining was performed with DAPI (Life, D3571). All steps were performed at room temperature. Stained sections were scanned using the Panoramic 250 FLASH II (3DHISTECH) Whole Slide Scanner at a 0.221 $\mu\text{m}/\text{px}$ resolution.

Immunoblot

Spinal cords or cortices of healthy and EAE mice were homogenized using a tissue grinder in 2 mL, radioimmuno-precipitation buffer (50 mM Tris, 150 mM NaCl, 0.5 mM EDTA, 10% SDS, 1% NP-40, 10% sodium deoxycholate, protease and phosphate inhibitor cocktails (cComplete, Roche)), incubated at 4°C for 30 minutes on a rotating wheel, and centrifuged for 5 minutes to remove the cell debris. Pellets from mouse primary neurons, bone marrow-derived dendritic cells and N2a cells were processed similarly but in a volume of only 200 μl radioimmuno-precipitation buffer. After measuring the protein concentrations by a BCA assay (Pierce BCA Protein Assay Kit, ThermoFisher) according to the manufacturer's protocol, we used 25 μg protein for subsequent loading on SDS-pages (NuPAGE, ThermoFisher) and wet transfer on polyvinylfluoride membranes. Blocking was performed using 5% BSA for 1 hour at room temperature. First antibodies were incubated overnight at 4°C . Horseradish peroxidase-labelled secondary antibodies were applied for 1 hour at room temperature and chemiluminescence was visualized using WesternSure PREMIUM Chemiluminescent Substrate (LI-COR) according to the manufacturer's protocol. We used the following concentrations: GAPDH 1:1,000, IRF3 1:1,000, Lamin B 1:1,000, LC3 1:500, NF κ B 1:500, pIRF3 1:1,000, pSTING 1:250, pTBK1 1:1,000, PSD95 1:1,000, STIM1 1:500, STING 1:500, Synapsin 1/2 1:500, TBK1 1:200, vinculin 1:1,000, Ig mouse HRP 1:20,000, Ig rabbit HRP 1:20,000.

Synaptoneurososome fractionation

Immediately after sacrificing mice, they were perfused with ice-cold PBS and the cortices were removed and stored on ice. We added 3 mL HEPES-buffered sucrose (HBS; 320 mM sucrose, 4 mM HEPES pH 7.4, 2 mM EDTA, 2 mM EGTA, 1 mM PMSF, protease inhibitor cocktail (Roche)) per cortex that were subsequently homogenized in a motor driven glass Teflon homogenizer at 900 rpm with 10–15 strokes. Of that, 100 μL was frozen away as homogenate inputs. Subsequently, we centrifuged for 15 minutes with $950 \times g$ at 4°C to remove the nuclear pellet. The supernatant was centrifuged for 15 minutes with $10,000 \times g$ at 4°C . The pellet was resuspended in 3 mL HBS and was centrifuged again for 15 minutes with $10,000 \times g$ at 4°C . We resuspended the pellet in 2 mL of the hypoosmotic shock solution (2 mM EDTA, protease inhibitor cocktail (Roche)) by pipetting up and down. Subsequently, we rapidly adjusted the suspension to 4 mM HEPES by adding 8 μL 1 M HEPES and continuously mixed the suspension for 30 minutes at 4°C . The lysate

was then centrifuged with $20,000 \times g$ for 60 minutes at 4°C . The pellet was used as crude synaptoneurosome fraction for subsequent experiments. Validation of the fractionation is shown in [Figure S1E](#).

Immunophenotyping by flow cytometry

Brain and spinal cord tissue were collected after transcardial PBS perfusion and were dissociated into single cell suspensions in 1 mg mL^{-1} collagenase A (Roche) and 0.1 mg mL^{-1} DNase I (Merck) using the gentleMACS Octo Dissociator (Miltenyi Biotec, program: Multi_F). The dissociated tissue was applied to a $70 \mu\text{m}$ cell strainer and immune and glia cells were enriched using a discontinuous density gradient. After centrifugation at 2,500 rpm, 4°C for 30 minutes, cells were collected from the interphase between the 30% Percoll and 78% Percoll layer. Nonspecific Fc receptor-mediated antibody binding was blocked by pre-incubation with TruStain FcX anti-mouse CD16/32 antibody (BioLegend) for 10 minutes at 4°C prior to staining of surface antibodies in Brilliant Stain Buffer (BD Biosciences) for 30 minutes at 4°C . We excluded dead cells from the analysis by staining with Zombie Green and NIR Fixable Viability Stains (BioLegend). For intracellular staining of CD68, cell suspensions were fixed for 20 minutes at room temperature using Fixation Buffer (BioLegend), followed by 20 minutes incubation with anti-CD68 antibody in Intracellular Staining Permeabilization Wash Buffer (BioLegend). For the determination of absolute cell numbers, CD45^{high} leukocytes and CD45^{med} microglia were quantified using Precision Count Beads (BioLegend). We obtained data using a BD Symphony A3 flow cytometer (BD Biosciences) and analyzed them by using FlowJo (BD Biosciences). The following antibody concentrations were used: CD4 1:200, CD8 1:200, CD11b 1:400, CD11c 1:400, CD19 1:200, CD45 1:100, CD68 1:100, CD80 1:200, CD86 1:100, CLEC7A 1:100, CXCR1 1:200, F4/80 1:100, I-A/I-E 1:200, Ly6C 1:200, Ly6G 1:100, NK1.1 1:100, P2RY12 1:100, TCR beta 1:100, TREM2 1:10, Zombie Green 1:1,000.

QUANTIFICATION AND STATISTICAL ANALYSIS

The statistical analyses applied during the bioinformatics analysis are detailed in the respective sections of the article. Images were analyzed using Fiji software (NIH). Experimental data were analyzed within the R environment on a Mac OS. Unless stated otherwise, the data are presented as means and differences between two experimental groups were determined using unpaired, two-tailed Student's *t*-tests and were FDR-corrected for multiple comparisons. Statistical analysis of the clinical scores in the EAE experiments was performed by applying a Mann-Whitney U-test to the areas under the curve for each animal. Significant results are indicated by * $P < 0.05$, ** $P < 0.01$, *** $P < 0.001$, **** $P < 0.0001$.

Supplemental figures

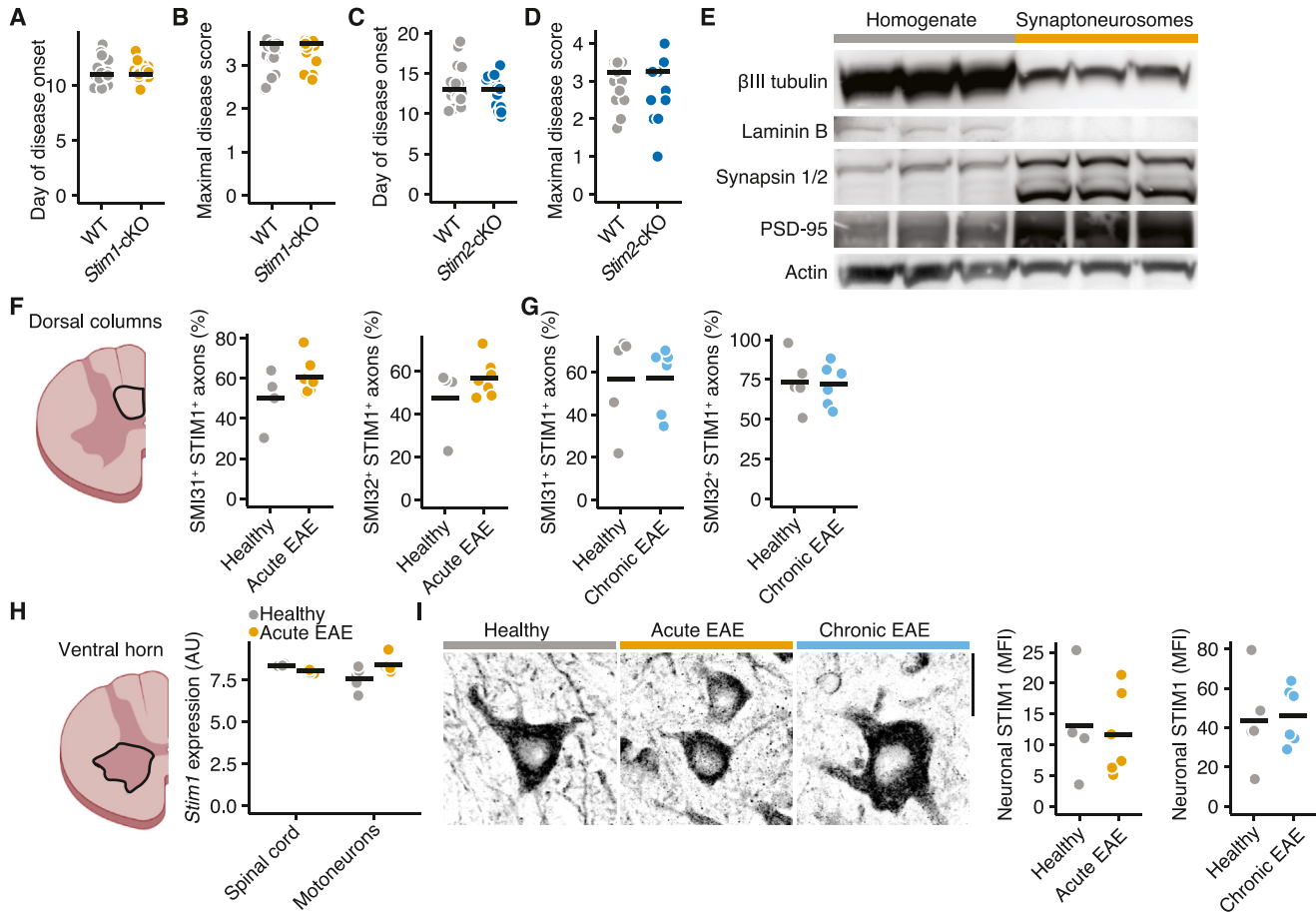


Figure S1. Neuronal STIM1 distribution but not expression is affected in CNS inflammation, related to Figure 1

(A and B) Day of disease onset (A) and maximal disease score (B) of WT ($n = 20$) and *Stim1-cKO* ($n = 18$) mice that were subjected to EAE.

(C and D) Day of disease onset (C) and maximal disease score (D) of WT ($n = 18$) and *Stim2-cKO* ($n = 13$) mice that were subjected to EAE.

(E) Immunoblots of the indicated proteins in whole cortex homogenates ($n = 3$) and purified synaptoneurosomes ($n = 3$).

(F and G) Percentage of STIM1⁺SMI31⁺ or STIM1⁺SMI32⁺ axons in spinal cord dorsal columns in healthy and acute (F) and healthy and chronic (G) EAE ($n = 6$ per group).

(H) *Stim1* mRNA expression (arbitrary units [a.u.]) in whole spinal cords and motor neurons 12 days after immunization ($n = 5$ per group). Data are retrieved from GEO: GSE104899.

(I) Neuronal STIM1 mean fluorescence intensity (MFI) in ventral horn motor neurons in healthy, acute, and chronic EAE ($n = 6$ per group). If not stated otherwise, unpaired t test with FDR correction for multiple comparisons was used, and individual mice and the median are shown.

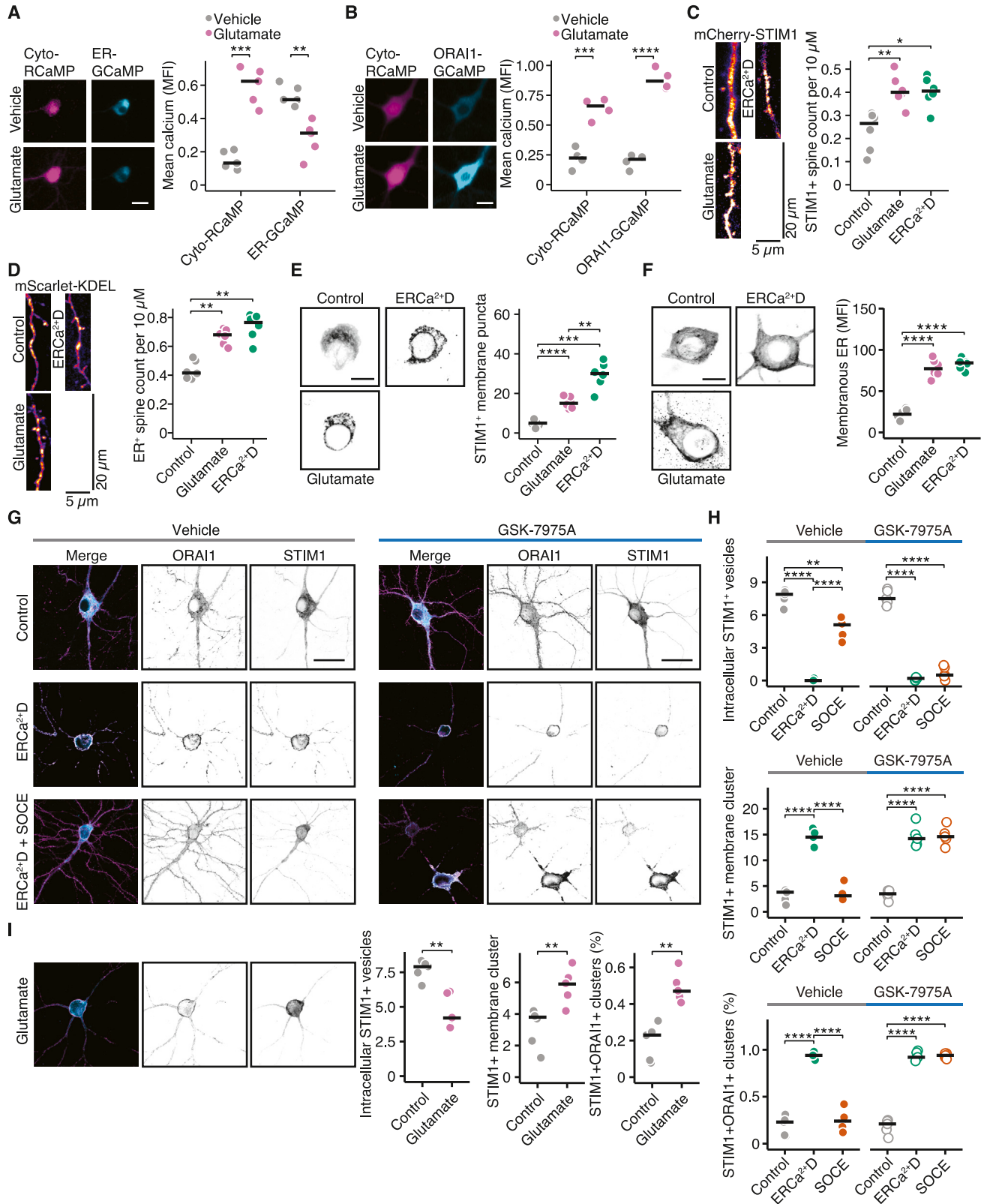


Figure S2. Glutamate excitotoxicity activates SOCE in neurons, related to Figure 2

(A and B) Mean fluorescence intensity (MFI) of RCaMP and ER-GCaMP (A) or Cyto-RCaMP and ORAI-GCaMP6f (B) transfected neurons that were exposed to vehicle or 50 μ M glutamate for 20 min ($n = 5$ per group). Scale bar shows 20 μ m.

(C and D) Number of STIM1⁺ or ER⁺ spines in neurons that were transfected with mCherry-STIM1 (C) or mScarlet-KDEL (D), respectively, and were exposed to vehicle, 50 μ M glutamate, or targeted ER calcium depletion (ERCa²⁺D) ($n = 6$ per group).

(E and F) Number of membranous STIM1+ puncta (E) and area of membranous ER MFI (F) in neurons that were transfected with mCherry-STIM1 or mScarlet-KDEL, respectively, and were exposed to vehicle, 50 μ M glutamate, or targeted ERCa²⁺D ($n = 6$ per group).

(G and H) Representative images (G) and quantification (H) of intracellular ORAI1⁺ vesicles, ORAI1+ membrane clusters, and percentage of STIM1⁺ORAI1⁺ clusters in neurons that were transfected with mCherry-STIM1 and YFP-ORAI1 and were exposed to ERCa²⁺D and subsequent store-operated calcium entry (SOCE) by calcium replenishing with or without addition of 20 μ M of the CRAC-inhibitor GSK-7975A ($n = 5$ per group).

(I) Quantification of intracellular ORAI1⁺ vesicles, ORAI1+ membrane clusters, and percentage of STIM1⁺ORAI1⁺ clusters in neurons that were transfected with mCherry-STIM1 and YFP-ORAI1 and were exposed to 50 μ M glutamate ($n = 5$). If not stated otherwise, unpaired t test with FDR correction for multiple comparisons was used, and independent experiments and the median are shown. * $p < 0.05$, ** $p < 0.01$, *** $p < 0.001$, **** $p < 0.0001$.

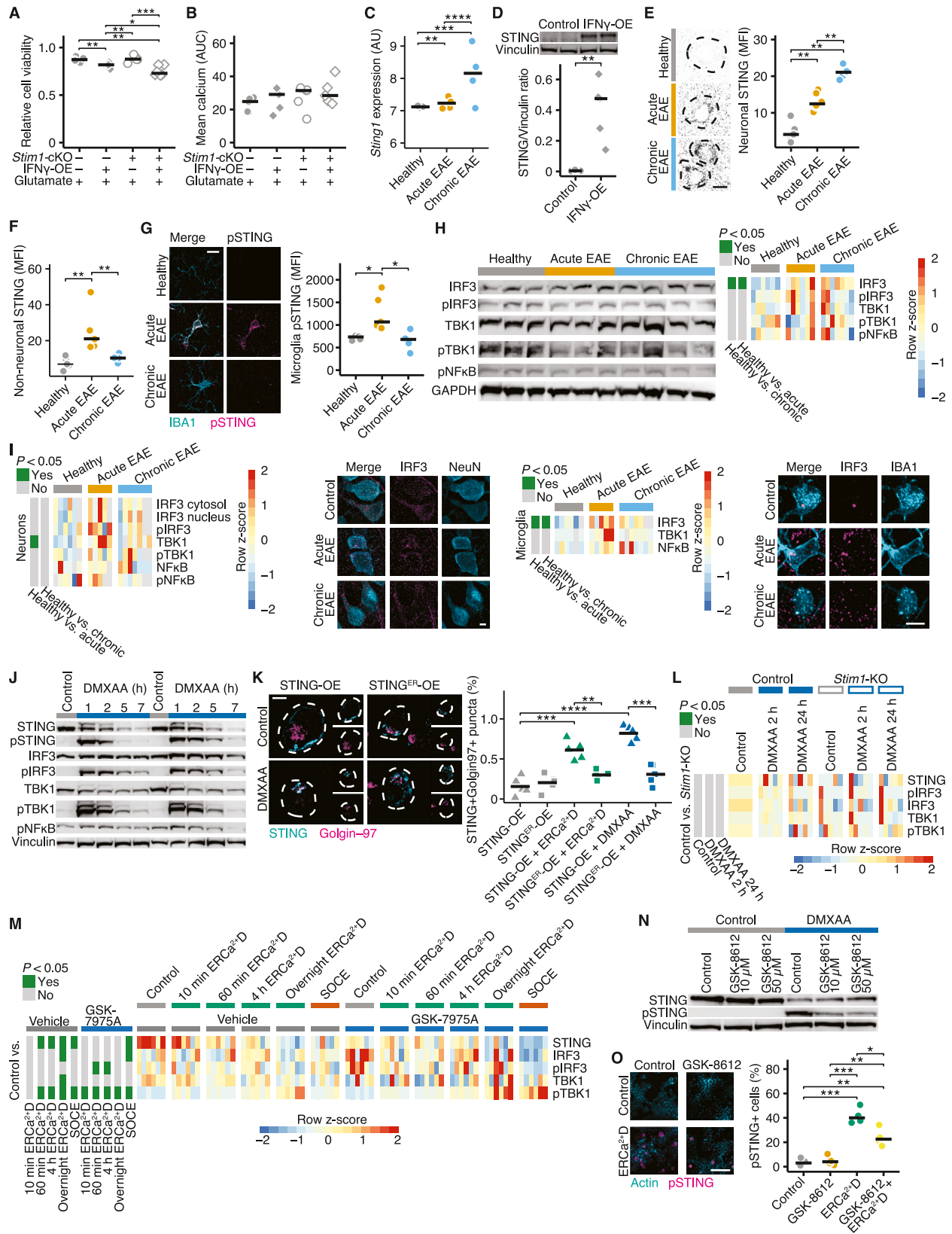


Figure S3. SOCE activates STING, related to Figure 2

(A and B) Relative cell viability (A; $n = 6$) and calcium accumulation (B; $n = 5$) quantified by area under the curve (AUC) of WT and *Stim1*-cKO neurons that overexpress IFNG and were exposed to 50 μM glutamate. Scale bar shows 20 μm .

(C) Neuronal *Sting1* mRNA expression (arbitrary units [a.u.]) in cortical neurons from healthy mice, acute and chronic EAE, by translating ribosome affinity purification and sequencing of Glt25d2-BacTRAP mice (healthy [$n = 5$], acute EAE [$n = 5$], and chronic EAE [$n = 4$]). Wald's test between group with FDR correction was used.

(D) Immunoblot of STING and vinculin in control neurons and neurons that overexpress IFNG (IFN γ -OE). Vinculin was used as normalization control ($n = 5$ per group).

(E) Immunohistochemistry of STING as mean fluorescence intensity (MFI) in neurons of the cortex from healthy and EAE mice ($n = 6$ per group). Scale bar shows 10 μm .

(F) STING MFI in NeuN $^{-}$ non-neuronal cells in the cortex of healthy and EAE mice ($n = 6$ per group).

(G) pSTING MFI in microglia of the cortex from healthy and EAE mice. The microglia marker IBA1 and pSTING are shown. Scale bar shows 10 μm .

(H) Protein levels of TBK1, pTBK1, IRF3, pIRF3, pNF- κB , and GAPDH in whole cortex lysates of healthy mice ($n = 6$), acute ($n = 6$), and chronic EAE mice ($n = 7$). Row Z scores are shown in the heatmap.

(I) Quantification of nuclear and cytosolic IRF3, pIRF3, TBK1, pTBK1, NF- κB , and pNF- κB in neurons (left panels) and microglia (right panels) of healthy and EAE mice ($n = 5$ per group) by immunohistochemistry. No signals for pTBK1, pNF- κB , and pIRF3 were detected in microglia and therefore not included in the heatmap. Row Z scores are shown in the heatmap. Scale bar shows 20 μm .

(J) Immunoblot for 2 biological replicates of STING, pSTING, IRF3, pIRF3, TBK1, pTBK1, pNF- κB , and vinculin of bone marrow-derived dendritic cells (BMDCs) that were treated with 20 $\mu\text{g mL}^{-1}$ STING agonist DMXAA for the indicated time points ($n = 2$).

(K) N2a cells that were transfected with EGFP-STING and EGFP-STING^{ER} and were subjected to targeted ER calcium depletion (ERCa²⁺D) or 50 $\mu\text{g mL}^{-1}$ DMXAA ($n = 5$ per group). The percentage of STING⁺Golgin-97⁺ puncta was quantified.

(L) Protein levels quantified by immunoblots of STING, TBK1, pTBK1, IRF3, pIRF3, and vinculin in WT and *Stim1*^{-/-} N2a cells that were treated with 50 $\mu\text{g mL}^{-1}$ DMXAA for 2 or 24 h ($n = 5$). Vinculin was used as normalization control. Row Z scores are shown in the heatmap. The immunoblot images are shown in Figure 2.

(M) Protein levels quantified by immunoblots of STING, pTBK1, TBK1, pIRF3, and vinculin in N2a cells that were treated with vehicle or 20 μM of the CRAC-inhibitor GSK-7975A and were subsequently exposed to targeted ERCa²⁺D for 10 min, 60 min, 4 h, overnight, or store-operated calcium entry (SOCE) by replenishing calcium after 1-h ERCa²⁺D ($n = 6$ per group). Row Z scores are shown in the heatmap. The immunoblot images are shown in Figure 2. Paired t tests were used to compare against control conditions.

(N) BMDCs were treated with 10 or 50 μM of the TBK1 inhibitor GSK-8612 and were subsequently treated with 20 $\mu\text{g mL}^{-1}$ DMXAA for 1 h. Immunoblot for STING, pSTING, and Vinculin.

(O) Percentage of pSTING⁺ N2a cells that were treated with 50 μM GSK-8612 and were exposed to ERCa²⁺D for 1 h ($n = 4$ per group). Scale bar shows 100 μm . If not stated otherwise, unpaired t test with FDR correction for multiple comparisons was used, and individual mice or independent experiments and the median are shown. * $p < 0.05$, ** $p < 0.01$, *** $p < 0.001$, **** $p < 0.0001$.

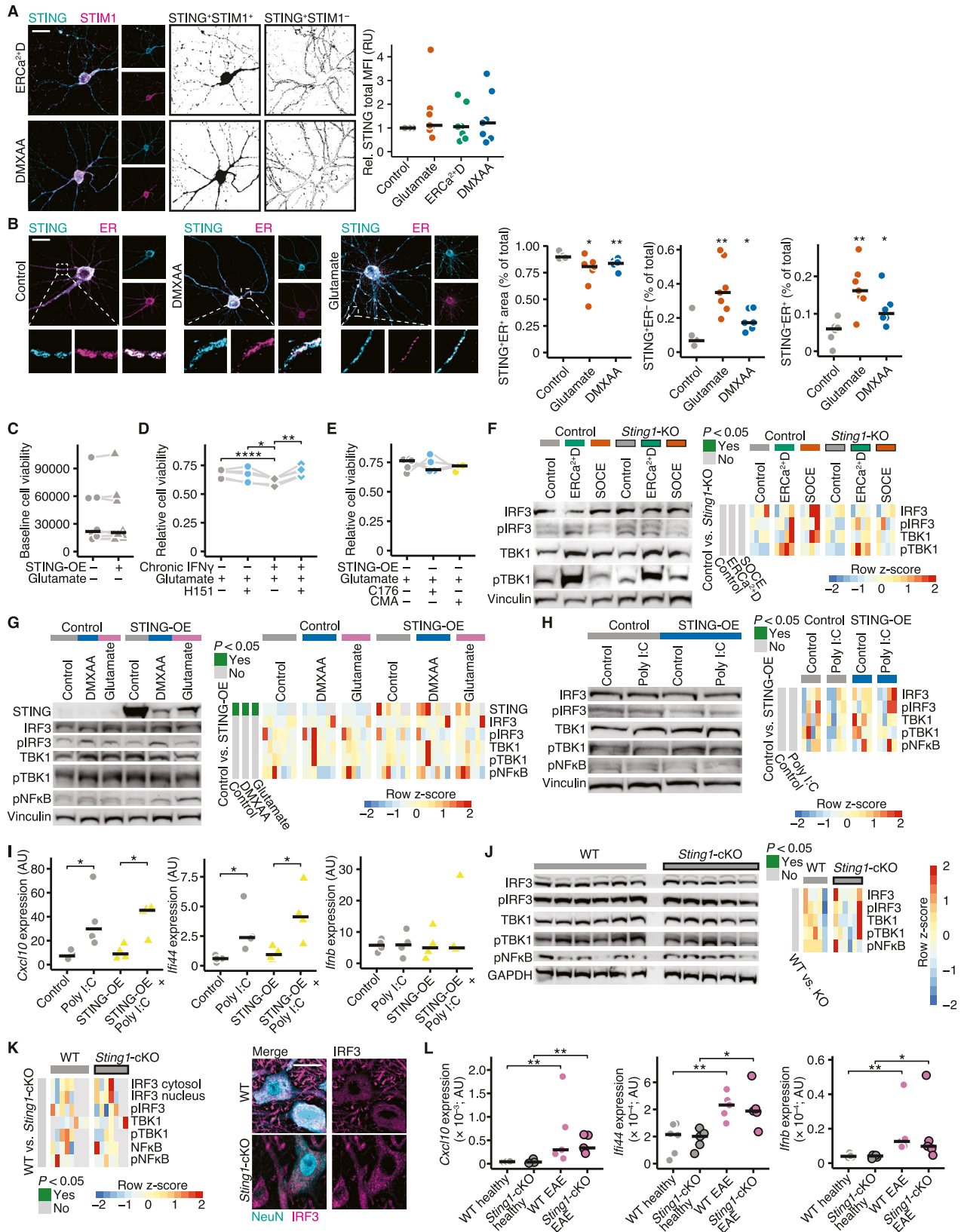


Figure S4. The canonical STING pathway is not activated in neurons, related to Figure 3

- (A) EGFP-STING and mCherry-STIM1 transfected neurons were subjected to 50 μM glutamate, 50 $\mu\text{g mL}^{-1}$ DMXAA, or targeted ER calcium depletion (ERCa²⁺D) for 6 h ($n = 7$ per group). Relative fold change as relative units (RUs) of EGFP-STING mean fluorescence intensity (MFI) across different conditions were quantified. Scale bar shows 30 μm .
- (B) EGFP-STING and mScarlet-KDEL transfected neurons were exposed to 50 μM glutamate or 50 $\mu\text{g mL}^{-1}$ DMXAA for 6 h ($n = 6$ per group). Percentages of STING⁺ER⁺ area, STING⁺ER⁻ area, and STING⁻ER⁺ area were quantified. Stimulated conditions were compared against controls. Scale bar shows 30 μm .
- (C) Baseline cell viability of STING-overexpressing (STING-OE) neurons and controls ($n = 7$ per group). Paired t test was used.
- (D) Neurons were treated from 7 to 15 d.i.v daily with 100 ng mL⁻¹ IFN γ . Subsequently, they were exposed to vehicle or 1 μM H151 and 50 μM glutamate for 24 h ($n = 5$ per group). Paired t test was used.
- (E) Relative cell viability of 50 μM glutamate-treated WT neurons that were additionally exposed to 1 μM C176 or 20 μM CMA ($n = 7$ per group). Paired t test was used.
- (F) Protein levels determined by immunoblots of IRF3, pIRF3, TBK1, pTBK1, and vinculin in WT and *Sting1*-KO N2a cells that were exposed to ERCa²⁺D and store-operated calcium entry (SOCE) by replenishing of calcium after 4 h of ERCa²⁺D ($n = 4$ per group). Vinculin was used as normalization control. Row Z scores are shown in the heatmap. Paired t tests were used to compare against control conditions.
- (G) Protein levels determined by immunoblots of STING, IRF3, pIRF3, TBK1, pTBK1, pNF- κ B, and vinculin of mScarlet-OE (control) and STING-OE neurons that were exposed to vehicle (control), 50 $\mu\text{g mL}^{-1}$ DMXAA, or 50 μM glutamate ($n = 6$ per group). Vinculin was used as normalization control.
- (H) mScarlet-overexpressing (control) or STING-OE neuronal cultures were treated with 5 $\mu\text{g mL}^{-1}$ poly(I:C) for 18 h, and protein levels of IRF3, pIRF3, TBK1, pTBK1, and pNF- κ B were quantified by immunoblots ($n = 4$ per group). Row Z scores are shown in the heatmap.
- (I) mRNA expression (arbitrary units [a.u.]) of *Cxcl10*, *Ifi44*, and *Ifnb* in neuronal mScarlet-overexpressing (control) or STING-OE neuronal cultures that were treated with 5 $\mu\text{g mL}^{-1}$ poly(I:C) for 28 h ($n = 4$ per group).
- (J) Immunoblot analysis of whole cortex lysates from WT ($n = 6$) and *Sting1*-cKO mice ($n = 5$) for IRF3 (cytosol or nucleus), pIRF3, TBK1, pTBK1, pNF- κ B, and GAPDH. Row Z scores are shown in the heatmap.
- (K) Neuronal protein levels of IRF3, pIRF3, TBK1, pTBK1, NF- κ B, and pNF- κ B in motor neurons of the cervical spinal cord in WT ($n = 5$) and *Sting1*-cKO ($n = 5$) EAE mice 30 days after immunization. Row Z scores are shown in the heatmap. Scale bar shows 20 μm .
- (L) mRNA expression (arbitrary units [a.u.]) of *Cxcl10*, *Ifi44*, and *Ifnb* in neuronal nuclei isolated from the spinal cords of WT and *Sting1*-cKO EAE mice ($n = 5$ per group) 30 days after immunization. If not stated otherwise, unpaired t test with FDR correction for multiple comparisons was used, and individual mice or independent experiments and the median are shown. * $p < 0.05$, ** $p < 0.01$, **** $p < 0.0001$.

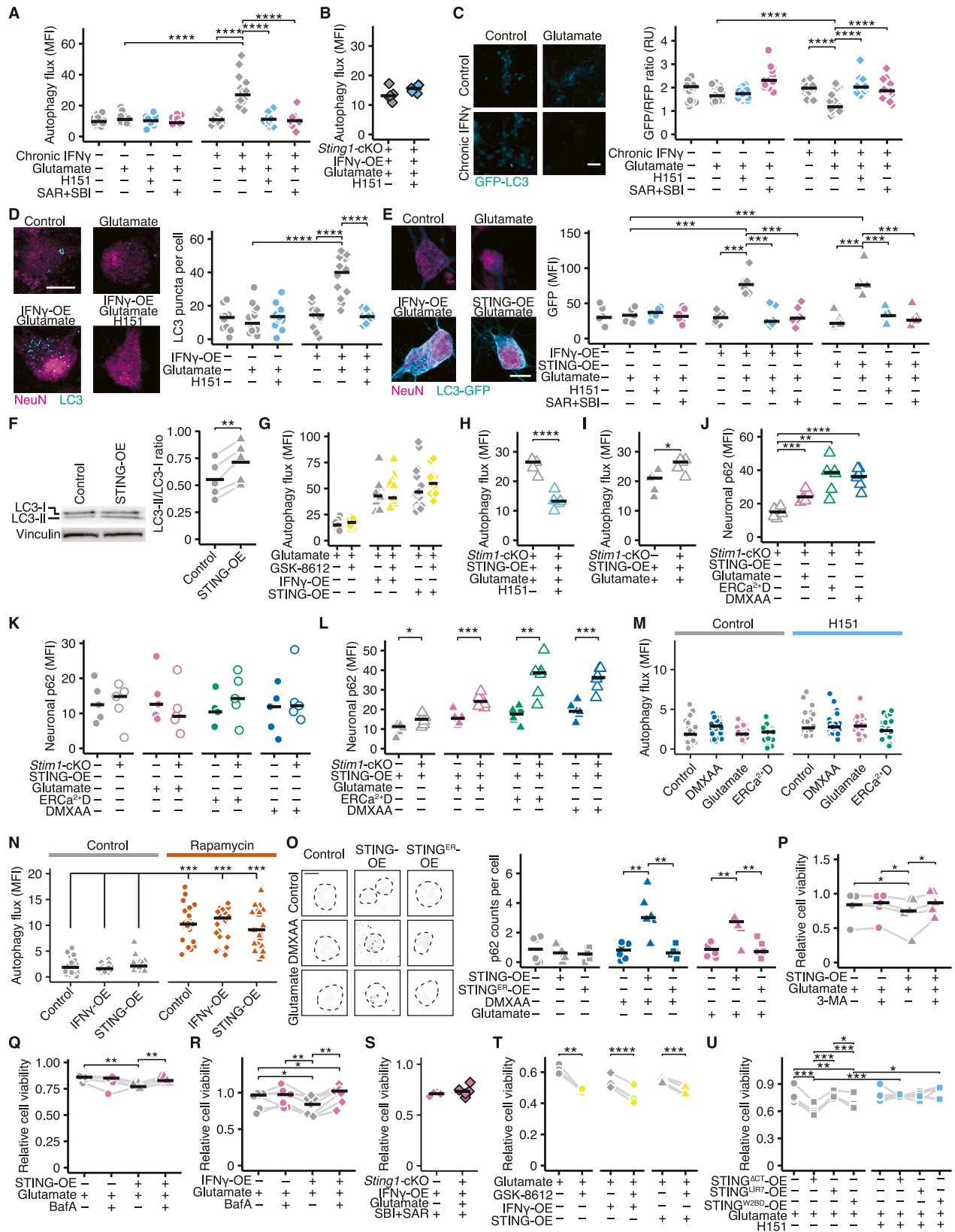


Figure S5. Inhibition of autophagy protects from STING-induced neuronal vulnerability, related to Figure 4

- (A) Mean fluorescence intensity (MFI) of CytolD to measure autophagic flux in neurons that were treated from 7 to 15 d.i.v. daily with 100 ng mL⁻¹ IFN γ and were exposed to 50 nM bafilomycin A1 and subsequently to 50 μ M glutamate for 4 h. If indicated, they were additionally pre-treated with vehicle control, 1 μ M H151 or 1 μ M SAR405 (SAR), and 1 μ M SBI-0206965 (SBI) at the same time ($n = 20$ from 5 different biological replicates per group).
- (B) Autophagy flux in *Sting1*-cKO neurons that overexpress IFNG (IFN γ -OE) and were treated with 50 nM bafilomycin A1 and subsequently exposed to 1 μ M H151 and 50 μ M glutamate for 4 h ($n = 5$ per group).
- (C) Quantification of LC3 degradation in neurons that were transfected with the GFP-LC3-RFP-LC3 Δ G reporter. Neuronal cultures were treated from 7 to 15 d.i.v. daily with 100 ng mL⁻¹ IFN γ and were exposed to 50 μ M glutamate for 4 h. If indicated, they were additionally pre-treated with vehicle control, 1 μ M H151 or 1 μ M SAR405 (SAR), and 1 μ M SBI-0206965 (SBI) at the same time ($n = 20$ from 5 different biological replicates per group). The GFP/RFP ratio is quantified as relative units (RUs). GFP of the GFP-LC3-RFP-LC3 Δ G is visualized (cyan). Scale bar shows 50 μ m.
- (D) Quantification of endogenous LC3 puncta per cell in neuronal cultures that overexpress mScarlet (control) or IFN γ and were treated with 50 nM bafilomycin A1 and were subsequently exposed to 50 μ M glutamate for 4 h. If indicated, they were additionally pre-treated with control, or 1 μ M H151 ($n = 16$ from 4 different biological replicates per group). Scale bar shows 10 μ m.
- (E) Quantification of GFP mean fluorescence intensity (MFI) in LC3-GFP transfected neurons that overexpress mScarlet (control), STING, or IFN γ and were treated with 50 nM bafilomycin A1 and were subsequently exposed to 50 μ M glutamate for 4 h. If indicated, they were additionally pre-treated with control, 1 μ M H151 or 1 μ M SAR405 (SAR), and 1 μ M SBI-0206965 (SBI) at the same time ($n = 6$ from 3 different biological replicates per group). NeuN (magenta) and GFP (cyan) are visualized. Scale bar shows 10 μ m.
- (F) LC3-II/LC3-I ratio of mScarlet- (control) and STING-overexpressing neurons that were treated with 50 μ M glutamate for 4 h ($n = 5$ per group).
- (G) Autophagy flux in WT neurons that overexpress STING (STING-OE) or IFN γ (IFN γ -OE) and were treated with 50 nM bafilomycin A1 and were subsequently exposed to 50 μ M glutamate for 4 h. If indicated neurons were treated with 50 μ M of the TBK1 inhibitor GSK-8612 ($n = 20$ from 4 different biological replicates per group).
- (H) Autophagy flux in *Stim1*-cKO neurons that overexpress STING (STING-OE) and were treated with 50 nM bafilomycin A1 and were subsequently exposed to 1 μ M H151 and 50 μ M glutamate for 4 h ($n = 5$ per group).
- (I) WT and *Stim1*-cKO neurons that overexpress STING and were treated with 50 nM bafilomycin A1 and were subsequently exposed to 50 μ M glutamate for 4 h ($n = 5$ per group).
- (J) Neuronal p62 MFI in *Stim1*-cKO neurons that were treated with 50 nM bafilomycin A1 and were subsequently exposed to 50 μ M glutamate, targeted ERCa²⁺D, or 50 μ g mL⁻¹ DMXAA for 4 h ($n = 6$ per group).
- (K) Comparison of neuronal p62 MFI between WT and *Stim1*-cKO neurons that were treated with 50 nM bafilomycin A1 and were subsequently exposed to 50 μ M glutamate, targeted ERCa²⁺D, or 50 μ g mL⁻¹ DMXAA for 4 h ($n = 6$ per group).
- (L) Comparison of neuronal p62 MFI between WT and *Stim1*-cKO neurons that overexpress STING and were treated with 50 nM bafilomycin A1 and were subsequently exposed to 50 μ M glutamate, targeted ERCa²⁺D, or 50 μ g mL⁻¹ DMXAA for 4 h ($n = 6$ per group).
- (M) Autophagic flux measured by CytolD MFI in WT neurons that were treated with 50 nM bafilomycin A1 and were subsequently exposed to 50 μ g mL⁻¹ DMXAA, 50 μ M glutamate, or targeted ER calcium depletion (ERCa²⁺D) for 4 h and were additionally pre-treated with control or 1 μ M H151 ($n = 20$ from 5 different biological replicates per group).
- (N) Autophagy flux in neurons that overexpress IFNG or STING and were treated with 50 nM bafilomycin A1 and were subsequently exposed to 500 nM rapamycin for 4 h ($n = 20$ from 5 different biological replicates per group).
- (O) STING-OE or STING^{ER}-OE neuronal cultures that were treated with 50 nM bafilomycin A1 and were subsequently exposed to 50 μ g mL⁻¹ DMXAA or 50 μ M glutamate for 4 h ($n = 6$ per group). Number of p62-positive puncta per cell was quantified. Scale bar shows 15 μ m.
- (P and Q) Relative cell viability of control and STING-overexpressing neurons that were treated with vehicle or 20 μ M 3-methyladenine (3-MA; P) or 50 nM bafilomycin A1 (Q; BafA) and were exposed to 50 μ M glutamate ($n = 5$ per group). Paired t test was used.
- (R) Relative cell viability of control and IFN γ -OE neurons that were treated with vehicle or 50 nM bafilomycin A1 (BafA) and were exposed to 50 μ M glutamate ($n = 6$ per group). Paired t test was used.
- (S) WT and *Sting1*-cKO that overexpress IFN γ and were treated with 1 μ M SAR405 (SAR) and 1 μ M SBI-0206965 (SBI) and were subsequently exposed to 50 μ M glutamate ($n = 5$ per group).
- (T) Relative cell viability of mScarlet- (control), IFN γ -, or STING-overexpressing neurons that were treated with 50 μ M of the TBK1 inhibitor GSK-8612 and were subsequently exposed to 50 μ M glutamate for 24 h ($n = 5$ per group). Paired comparisons were used.
- (U) Relative cell viability of neuronal cultures that overexpress mScarlet (control) or the STING variants STING ^{Δ CT}, STING^{W2BD}, or STING^{LIR7} and were treated with 1 μ M H151 or vehicle and were subsequently exposed to 50 μ M glutamate for 24 h ($n = 5$ per group). Paired comparisons were used. If not stated otherwise, unpaired t test with FDR correction for multiple comparisons was used, and independent experiments and the median are shown. * $p < 0.05$, ** $p < 0.01$, *** $p < 0.001$, **** $p < 0.0001$.

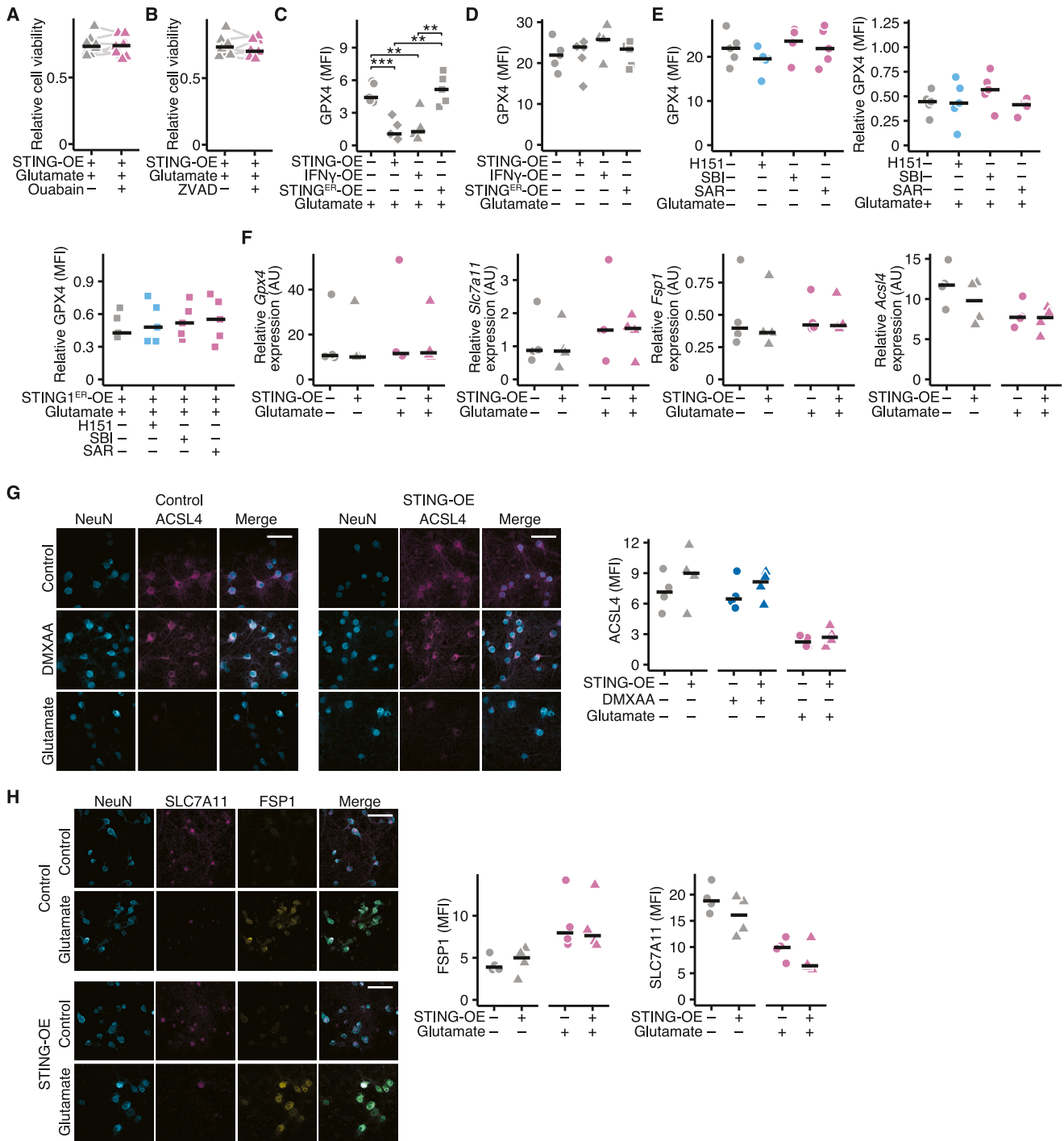


Figure S6. STING does not regulate ACSL4, FSP1, and SLC7A11 expression, related to Figure 5

(A and B) STING-overexpressing (STING-OE) neuronal cultures were treated with 1 μ M of the Na⁺/K⁺-ATPase inhibitor ouabain (A) or 20 μ M of the pan-caspase inhibitor Z-VAD-AMK (B; ZVAD) and were subsequently exposed to 50 μ M glutamate ($n = 7$). Paired t test was used.

(C) Dendritic GPX4 mean fluorescence intensity (MFI) in neuronal cultures that overexpress STING, IFN γ (IFN γ -OE), or STING^{ER} ($n = 5$; STING^{ER}-OE) and were exposed to glutamate for 6 h.

(D) GPX4 MFI in neuronal cultures overexpress STING, IFN γ (IFN γ -OE), or STING^{ER} ($n = 5$; STING^{ER}-OE).

(E) GPX4 MFI in WT or STING^{ER}-overexpressing neurons that were treated with 1 μ M H151, 1 μ M SAR405 (SAR), or 1 μ M SBI-0206965 (SBI) and were subsequently exposed to vehicle or 50 μ M glutamate ($n = 5$).

(legend continued on next page)

(F) mRNA expression (arbitrary units [a.u.]) of *Gpx4*, *Slc7a11*, *Fsp1*, and *Acsf4* in control or STING-overexpressing neuronal cultures that were exposed to vehicle or 50 μ M glutamate ($n = 4$).

(G) ACSL4 mean fluorescence intensity (MFI) in control and STING-overexpressing neuronal cultures that were exposed to 50 μ M glutamate or 50 μ g mL⁻¹ DMXAA for 6 h ($n = 4$).

(H) SLC7A11 and FSP1 MFI in control and STING-overexpressing neuronal cultures that were exposed to 50 μ M glutamate for 6 h ($n = 4$). If not stated otherwise, unpaired t test with FDR correction for multiple comparisons was used, and independent experiments and the median are shown. ** $p < 0.01$, *** $p < 0.001$.

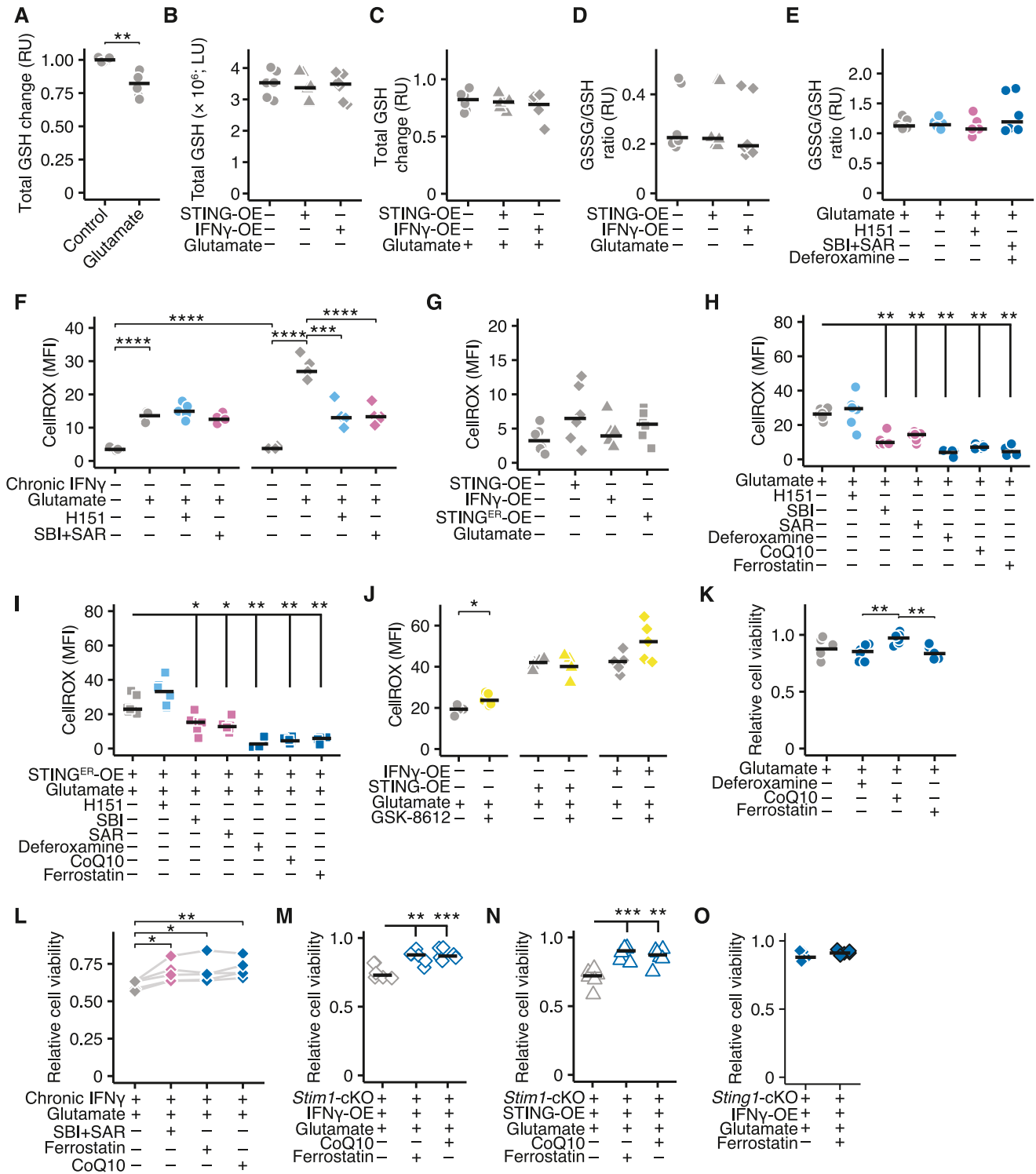


Figure S7. Neuronal STIM1 deficiency increases STING-activated ferroptosis, related to Figure 5

(A) Relative change of GSH in neuronal cultures that were treated with 50 μ M glutamate for 4 h ($n = 5$ per group). Data were normalized to control neurons and are shown as relative units (RUs).

(B) Total GSH levels as luminescence units (LUs) in STING- (STING-OE) or IFN γ -overexpressing (IFN γ -OE) neurons or control neurons ($n = 6$ per group).

(C) Relative change of total GSH in STING-OE or IFN γ -OE or control neurons that were exposed to 50 μ M glutamate for 4 h ($n = 6$ per group). Data were normalized to control neurons and are shown as relative units (RUs).

(legend continued on next page)

-
- (D) Change of the GSSG/GSH ratio as relative units (RUs) in STING- or IFNG-overexpressing neurons or control neurons ($n = 5$ per group).
- (E) Change of the GSSG/GSH ratio as relative units (RU) in neurons that were treated with 1 μM H151, 1 μM SBI-0206965 (SBI), 1 μM SAR405 (SAR), and/or 20 μM deferoxamine.
- (F) CellROX mean fluorescence intensity (MFI) in neurons that were treated with 100 ng mL^{-1} $\text{IFN}\gamma$ from 7 to 15 d.i.v. and were treated with 50 μM glutamate for 2 h ($n = 5$ per group). If indicated, they were pre-treated with 1 μM H151 or 1 μM SBI and 1 μM SAR at the same time.
- (G) CellROX mean fluorescence intensity (MFI) in STING-OE, $\text{IFN}\gamma$ -OE, or STING^{ER}-OE neurons or control neurons ($n = 6$ per group).
- (H and I) CellROX MFI in control neurons (H) and STING^{ER}-OE neurons (I) that were treated with 1 μM H151, 1 μM SBI, 1 μM SAR, 20 μM deferoxamine, 6 μM coenzyme Q10 (Co-Q10), or 1 μM ferrostatin and were subsequently exposed to 50 μM glutamate for 2 h ($n = 6$ per group). All conditions were compared against respective controls.
- (J) CellROX MFI of mScarlet- (control), $\text{IFN}\gamma$ -, or STING-overexpressing neurons that were treated with 50 μM of the TBK1 inhibitor GSK-8612 and were subsequently exposed to 50 μM glutamate for 2 h ($n = 5$ per group).
- (K–N) Relative cell viability of WT neuronal cultures (K; $n = 6$), neuronal cultures that were treated with 100 ng mL^{-1} $\text{IFN}\gamma$ from 7 to 15 d.i.v (L; $n = 5$), *Stim1*-cKO neurons that overexpress IFNG (M; $n = 6$) or STING (N; $n = 6$) and if indicated were treated with 1 μM SBI and 1 μM SAR at the same time, 20 μM deferoxamine, 6 μM CoQ, or 1 μM ferrostatin and were exposed to 50 μM glutamate. Paired comparisons were used for (L).
- (O) Control and *Sting1*-cKO neurons that were treated with 1 μM ferrostatin and were subsequently exposed to 50 μM glutamate ($n = 5$ per group). If not stated otherwise, unpaired t test with FDR correction for multiple comparisons was used, and independent experiments and the median are shown. * $p < 0.05$, ** $p < 0.01$, *** $p < 0.001$, **** $p < 0.0001$.

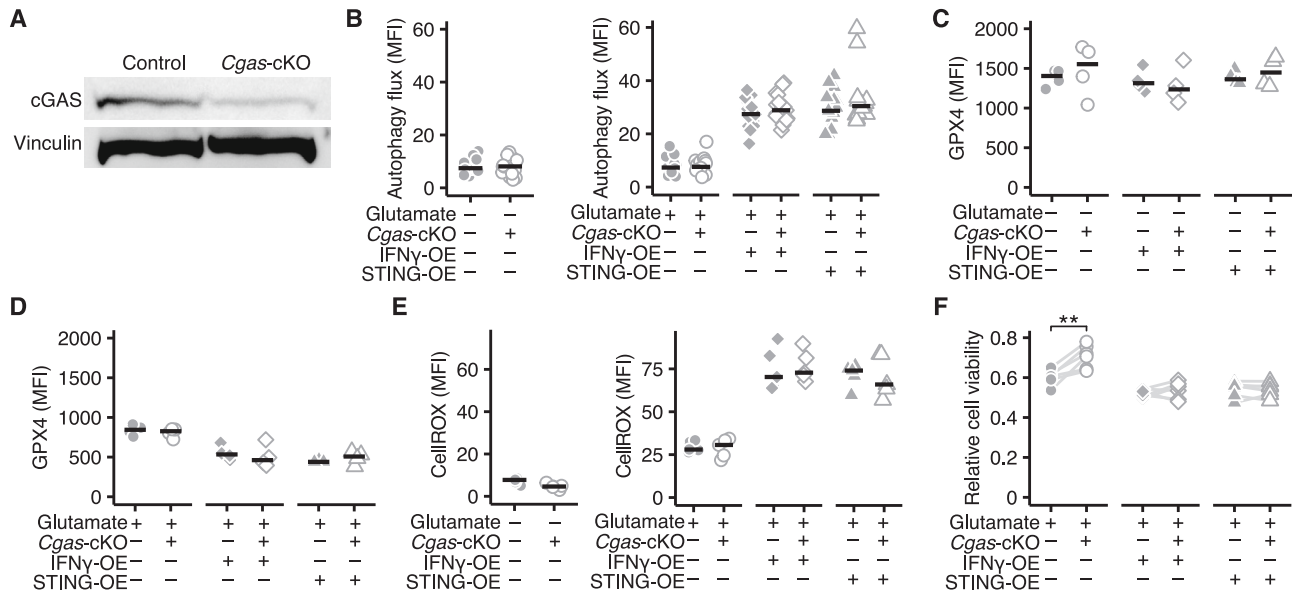


Figure S8. STING-induced ferroptosis is independent from cGAS in neurons, related to Figure 5

(A) Immunoblot of cGAS and vinculin in WT and CRISPR-Cas9-mediated *Cgas*-cKO neuronal cultures.

(B) Autophagic flux measured by Cytold mean fluorescence intensity (MFI) in WT and *Cgas*-cKO neuronal cultures that overexpress STING or IFN γ and were treated with 50 nM bafilomycin A1 at baseline or 4 h after exposure to 50 μ M glutamate ($n = 20$ cells from 5 independent replicates per group).

(C) Baseline GPX4 MFI in WT and *Cgas*-cKO neuronal cultures that overexpress STING or IFN γ ($n = 4$ per group).

(D) GPX4 mean fluorescence intensity (MFI) in WT and *Cgas*-cKO neuronal cultures that overexpress STING or IFN γ ($n = 4$ per group) and were treated with 50 μ M glutamate for 6 h.

(E) CellROX MFI in WT and *Cgas*-cKO neuronal cultures that overexpress STING or IFN γ at baseline and after exposure to 50 μ M glutamate for 2 h ($n = 5$ per group).

(F) Relative cell viability of WT and *Cgas*-KO neuronal cultures that overexpress STING or IFN γ and were treated with 50 μ M glutamate for 24 h ($n = 6$ per group). Paired comparisons were used. If not stated otherwise, unpaired t test with FDR correction for multiple comparisons was used, and independent experiments and the median are shown. ** $p < 0.01$.

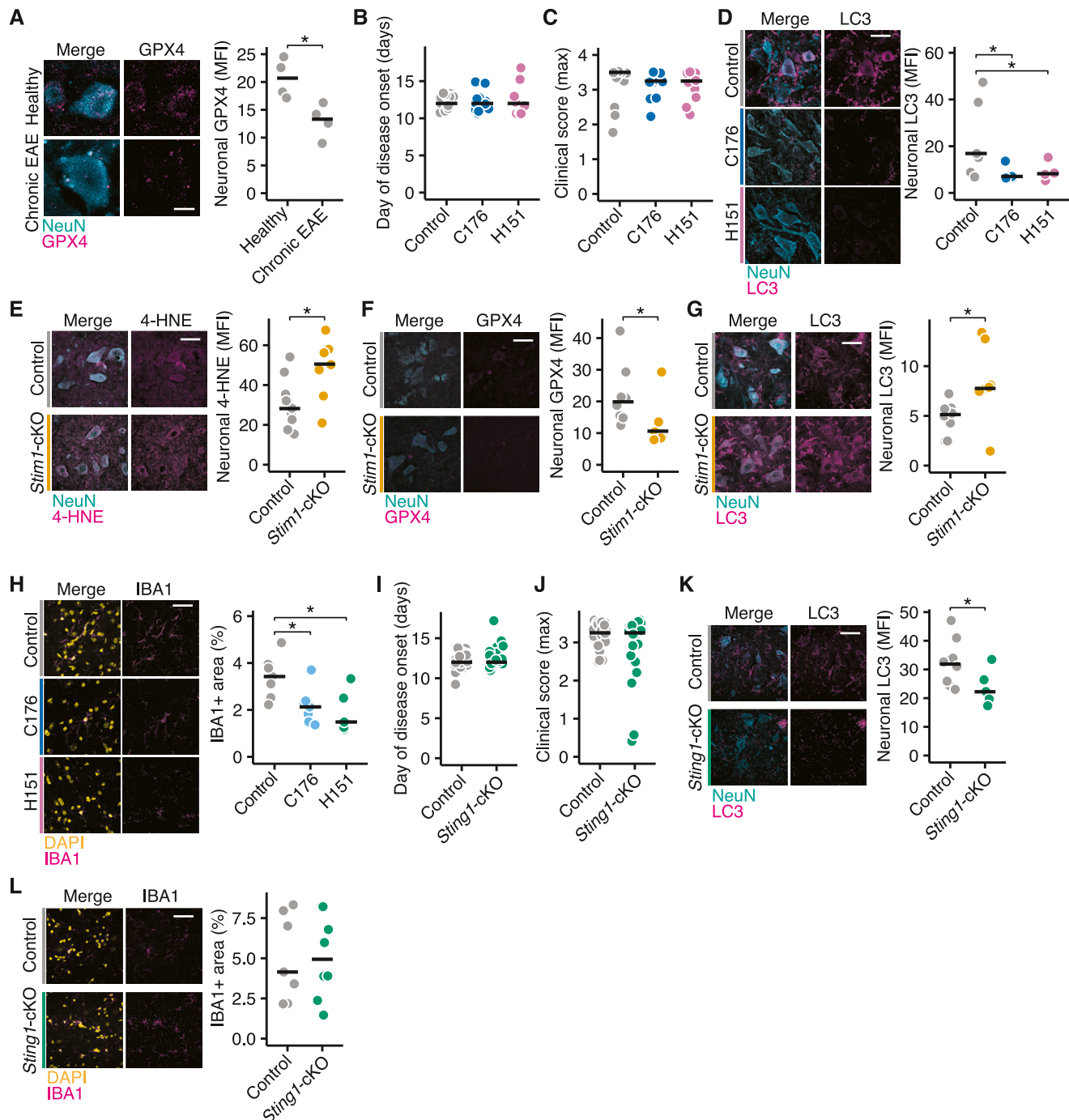


Figure S9. STING increases neuronal autophagy in EAE, related to Figure 6

(A) Neuronal GPX4 mean fluorescence intensity (MFI) in motor neurons of the cervical spinal cord of healthy and EAE mice 30 days after immunization ($n = 4$). Scale bar shows 10 μm .

(B and C) Day of disease onset (B) and maximal clinical disease score (C) of EAE mice that were treated with vehicle ($n = 13$), C176 ($n = 13$), or H151 ($n = 10$) i.p. daily since day of disease onset.

(D) Neuronal LC3 mean fluorescence intensity (MFI) in motor neurons labeled with NeuN of spinal cord ventral horns of EAE mice that were treated with vehicle ($n = 8$), C176 ($n = 8$), or H151 ($n = 8$) 30 days after immunization. Scale bar shows 20 μm .

(E–G) Neuronal MFI of 4-hydroxy-2-nonenal (E; 4-HNE), GPX4 (F), and LC3 (G) co-labeled with NeuN in ventral horn spinal cords of WT ($n = 8$) and Stim1-cKO ($n = 7$) EAE mice 30 days after immunization. Scale bar shows 20 μm .

(H) IBA1-covered area co-labeled with DAPI (yellow) in the gray matter of spinal cord ventral horns of EAE mice that were treated with vehicle ($n = 8$), C176 ($n = 8$), or H151 ($n = 8$) 30 days after immunization. Scale bar shows 20 μm .

(I and J) Day of disease onset (I) and maximal clinical disease score (J) of WT ($n = 25$) and *Sting1*-cKO EAE ($n = 21$) mice.

(legend continued on next page)

(K) Neuronal LC3 mean fluorescence intensity (MFI) in motor neurons labeled with NeuN of spinal cord ventral horns of WT ($n = 10$) and *Sting1*-cKO ($n = 6$) EAE mice 30 days after immunization.

(L) IBA1 covered area co-labeled in the gray matter of spinal cord ventral horns of WT ($n = 7$) and *Sting1*-cKO ($n = 8$) EAE mice 30 days after immunization. If not stated otherwise, unpaired t test with FDR correction for multiple comparisons was used, and individual mice and the median are shown. * $p < 0.05$, ** $p < 0.01$.

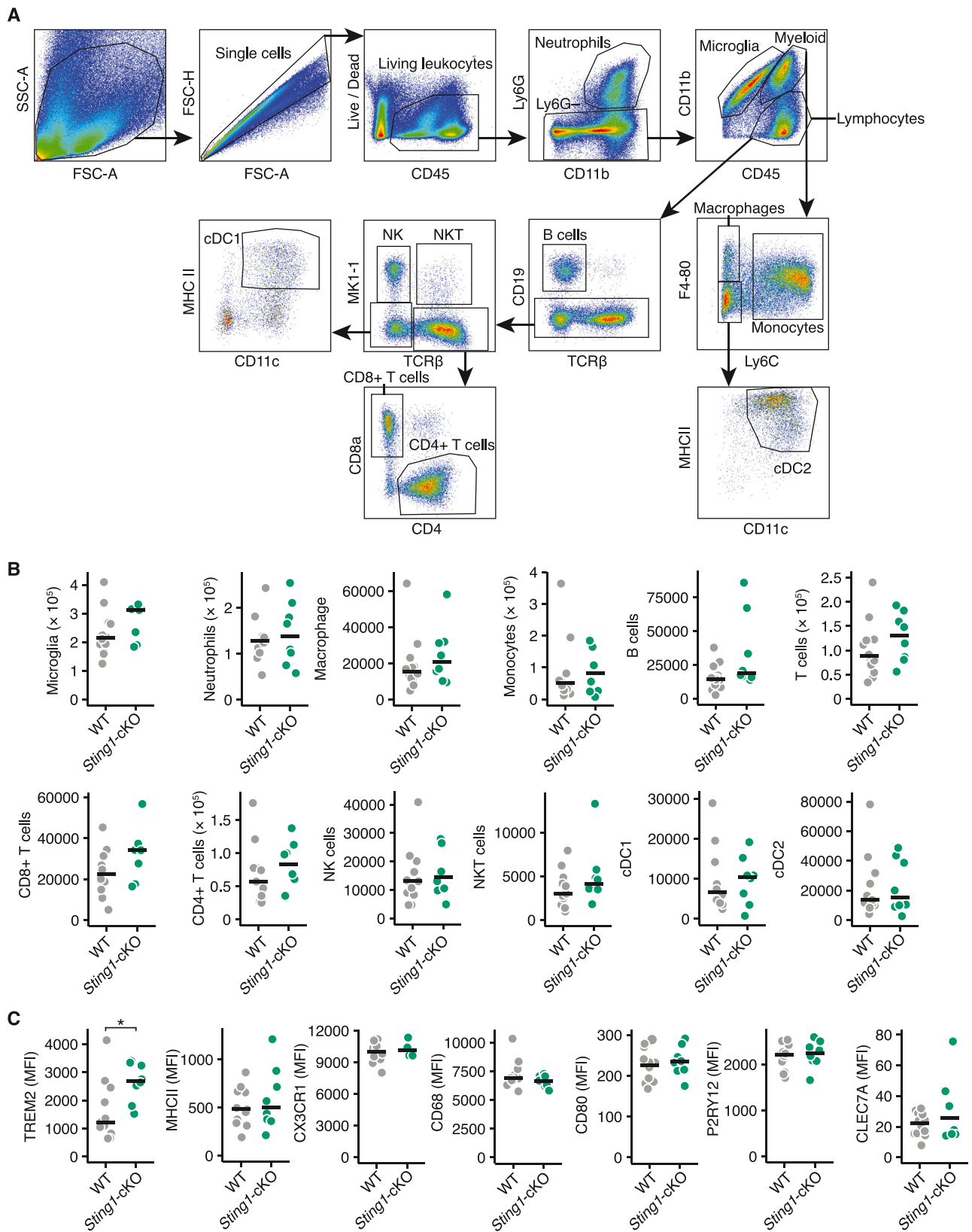


Figure S10. WT and neuronal *Sting1*-cKO mice show similar immune cell infiltration and activation during EAE, related to Figure 6

(A) Representative gating strategy for CNS immunophenotyping in EAE mice.

(B) Absolute quantification of indicated CNS-infiltrating immune cell subtypes of WT ($n = 11$) and *Sting1*-cKO ($n = 8$) EAE mice 30 days after immunization.

(C) Mean fluorescence intensity (MFI) of indicated markers of microglia isolated from the CNS of WT ($n = 11$) and *Sting1*-cKO ($n = 8$) EAE mice 30 days after immunization. If not stated otherwise, unpaired t test with FDR correction for multiple comparisons was used, and individual mice and the median are shown.